

DESIGN AND DEVELOPMENT  
OF A 1MM RESOLUTION CLINICAL  
POSITRON EMISSION TOMOGRAPHY (PET) SYSTEM

A DISSERTATION  
SUBMITTED TO THE DEPARTMENT OF  
ELECTRICAL ENGINEERING  
AND THE COMMITTEE ON GRADUATE STUDIES  
OF STANFORD UNIVERSITY  
IN PARTIAL FULFILLMENT OF THE REQUIREMENTS  
FOR THE DEGREE OF  
DOCTOR OF PHILOSOPHY

Frances Wing Yee Lau

August 2013

© 2013 by Frances Wing Yee Lau. All Rights Reserved.

Re-distributed by Stanford University under license with the author.



This work is licensed under a Creative Commons Attribution-Noncommercial 3.0 United States License.

<http://creativecommons.org/licenses/by-nc/3.0/us/>

This dissertation is online at: <http://purl.stanford.edu/hq866nc5892>

I certify that I have read this dissertation and that, in my opinion, it is fully adequate in scope and quality as a dissertation for the degree of Doctor of Philosophy.

**Craig Levin, Primary Adviser**

I certify that I have read this dissertation and that, in my opinion, it is fully adequate in scope and quality as a dissertation for the degree of Doctor of Philosophy.

**Mark Horowitz**

I certify that I have read this dissertation and that, in my opinion, it is fully adequate in scope and quality as a dissertation for the degree of Doctor of Philosophy.

**Bruce Wooley**

Approved for the Stanford University Committee on Graduate Studies.

**Patricia J. Gumport, Vice Provost for Graduate Education**

*This signature page was generated electronically upon submission of this dissertation in electronic format. An original signed hard copy of the signature page is on file in University Archives.*

# Abstract

Positron Emission Tomography (PET) is an in-vivo medical imaging modality that extracts information about molecular processes associated with disease. A PET system produces an image of radiopharmaceuticals that have preferentially accumulated in certain cells of tissues in the body, such as cancerous lesions. Clinical PET systems have about 5-10mm spatial resolution, and thus have difficulty resolving very small lesions. So, improving the resolution of PET is an active area of research.

This thesis describes the design of a 1mm<sup>3</sup> resolution PET system for breast cancer imaging and the strategies used to overcome the challenges of developing such a high resolution PET system. The detectors in this PET system consist of lutetium yttrium oxyorthosilicate (LYSO) scintillation crystal arrays coupled to position-sensitive avalanche photodiodes (PSAPDs). There will be over 2000 Dual-LYSO-PSAPD detector modules in the final system, each requiring a bias voltage of 1750 Volts. A programmable high voltage distribution method allows the bias voltage to be optimized for each detector module. Multiplexing of detector signals reduced the number of interconnects by 40% and front-end electronic channels by 33%. Charge division and charge sharing signal conditioning compensate for the mismatch between the detector signal and the front-end electronics input dynamic range, as well as for parasitic capacitance introduced by interconnect. A model of the detectors and electronics was created to help understand the system and to assist in the system design process. Two cartridges of the system, consisting of 256 Dual-LYSO-PSAPD detectors, were constructed and characterized. The system energy resolution was 11% FWHM (full-width-at-half-maximum) and the measured spatial resolution was less than 1mm. The system was able to produce reconstructed images of a phantom with 1.2mm rods filled with a solution of the positron emitter Fluorine-18.



# Acknowledgments

I would like to thank everyone who mentored, taught, helped, and supported me throughout my years at Stanford. First and foremost, I would like to express my gratitude to my advisor Professor Craig Levin for supporting, motivating, and guiding me all these years. I'd like to thank him for encouraging me to explore new ideas and to apply for fellowships. Through his passion and dedication, Professor Levin fostered a stimulating and collaborative environment in his laboratory to work and learn. I'm very grateful to him for giving me this invaluable opportunity to work on cancer research as an electrical engineer, entrusting me to play an influential role on such an exciting, large-scale project.

I feel very fortunate to have been able to learn so much from my co-advisor Professor Mark Horowitz on technical issues, and I'm grateful for his mentorship throughout all these years. I'd like to thank him for the great learning opportunity of working as part of his research group on several integrated circuit design projects, which gave me the chance to broaden my experience. I would like to thank Professor Bruce Wooley for showing interest in my work and for taking the time to read my thesis and to be on my Orals Committee. I'm grateful to Professor Guillem Pratx for his input on my research and for serving on my Orals Committee. Finally, I would like to thank Professor Olav Solggard for serving as the Chair of my Orals Committee and for giving me the chance to be a teaching assistant for his undergraduate class.

The breast-dedicated PET system described in this thesis was a large-scale project that required the collaborative effort of many individuals in Professor Levin's Molecular Imaging Instrumentation Lab. The results presented in this thesis would not have been possible without everyone's work. It is impossible to list everyone who helped,

but I would like to highlight a some contributions. Arne characterized detectors, wrote analysis software, and helped with a number of other things. Paul designed the RENA-3 ASIC board and backend electronics, wrote FPGA code, and analyzed data. Derek and Jinjian worked on mechanical design and assembly. Umit and David F. wrote data acquisition and control software. Jung-Yeol and David H. helped with designing later versions of the High Voltage Floating Power Supply board. Alex and Jing-yu did image reconstruction. Preliminary investigations by Angela, Peter, Jin, Garry, and Professor Levin got this project funded. I had the privilege of mentoring three undergraduates, Holly, Naran, and Femi, and I thank them for their help with high voltage design and microcontroller programming. I would like to thank Richard and Mickel from Radiation Monitoring Devices for their support with our photodetectors.

In addition to all these people who I worked with directly on the breast-dedicated PET system project, I'd like to thank the rest of the Molecular Imaging Instrumentation Lab members for their help and friendship, especially Alex, Donna, Ealgoo, Eric, Hao, Kader, Key Jo, Matt, Ruud, Virginia, and Yi. At the beginning of my graduate student years, I was worried that doing a PhD would be a lonely journey, but fortunately that certainly did not turn out to be the case (since we all sat in one big lab room!). Working with such a collaborative and friendly group made my PhD years so much more enjoyable, and I'll always remember the fun times spent in the lab and at conferences.

I also worked with Mark Horowitz' group on integrated circuit design projects during my PhD studies, including a sensor-interface integrated circuit for PET applications, a high speed ADC, and circuit design methodology ideas. I'm especially grateful to Hwang Ho, Byong, Sabrina, James, Suyao, Metha, Donguk, Valentin, Ofer, and Jaeha. Without their help and contributions, fabrication of the integrated circuit for PET would not have been possible.

I would like to thank my PhD Qualifying Exam study buddies and coursework project partners who made studying so much more pleasant. My time at Stanford would not have been the same without the wonderful friends I met, especially Prasanthi, Christina, June, Gordon, and Nishant.

My studies and research would not have been possible without the funding sources that supported me. I'm very grateful to Stanford BioX for awarding me a BioX Graduate Student Fellowship. I'd like to acknowledge the National Institute of Health (NIH R01CA119056, R01CA119056-S1 (ARRA), R33 EB003283) for sponsoring the breast-dedicated PET system project. I'd also like to thank the California Breast Cancer Research Program (CBCRP) for the Dissertation Award that sponsored my work on the sensor interface integrated circuit for PET. My gratitude goes to the Stanford EE department for giving me a Teaching Assistantship Funding Award, without which I may not have even come to Stanford to study. I'm grateful for the Edward S. Rogers Sr. Scholarship in Electrical and Computer Engineering which funded my undergraduate studies at the University of Toronto, and the National Research Council Canada for the enlightening summer research experiences I had as an undergraduate which set me on the path towards research.

Finally, my eternal gratitude goes to my family for supporting me in all my endeavors. I'm so grateful for Jackson, who was always able to cheer me up after a long day in the lab with his positive outlook. I'd like to thank my uncle and aunt for treating me as their own daughter. My heartfelt thanks goes to my parents, grandparents, and sister for their continuous love, support, and encouragement.

# Contents

<b>Abstract</b>	<b>iv</b>
<b>Acknowledgments</b>	<b>v</b>
<b>1 Introduction</b>	<b>1</b>
1.1 Thesis organization . . . . .	2
<b>2 PET Background</b>	<b>3</b>
2.1 PET system performance metrics . . . . .	6
2.1.1 Photon sensitivity . . . . .	6
2.1.2 Spatial resolution . . . . .	7
2.1.3 Contrast resolution . . . . .	9
2.2 PET detectors . . . . .	11
2.2.1 Scintillators . . . . .	12
2.2.2 Photodetectors . . . . .	13
2.3 Front-end electronics . . . . .	20
2.3.1 Charge-sensitive amplification . . . . .	22
2.3.2 Transimpedance amplification . . . . .	24
2.3.3 Shaping . . . . .	34
2.3.4 Time discrimination . . . . .	35
2.3.5 Waveform digitization . . . . .	36
2.4 Breast cancer and PET . . . . .	38

<b>3</b>	<b>Breast-Dedicated PET System Electronics</b>	<b>40</b>
3.1	High resolution detector . . . . .	44
3.2	Interconnect . . . . .	47
3.3	Programmable high voltage distribution . . . . .	49
3.4	RENA-3 ASIC and Board . . . . .	55
3.5	Discrete Board . . . . .	57
3.5.1	Common-side charge division . . . . .	59
3.5.2	PSAPD leakage current monitoring . . . . .	60
3.6	Summary of components studied . . . . .	62
<b>4</b>	<b>Detector interface circuit design</b>	<b>64</b>
4.1	PSAPD and electronics modeling and simulation . . . . .	64
4.1.1	LYSO scintillation crystal array modeling . . . . .	66
4.1.2	PSAPD and electronics modeling . . . . .	67
4.1.3	Simulation of flood histogram . . . . .	70
4.2	PSAPD analog signal multiplexing . . . . .	70
4.2.1	Analog signal multiplexing configuration . . . . .	71
4.2.2	Simulation and experimental setup . . . . .	72
4.2.3	Simulation results . . . . .	75
4.2.4	Experimental results . . . . .	77
4.2.5	Conclusions from multiplexing study . . . . .	83
4.3	Signal conditioning . . . . .	84
4.3.1	Shunt capacitor signal conditioning . . . . .	85
4.3.2	Shunt resistor signal conditioning . . . . .	87
4.3.3	Series capacitor signal conditioning . . . . .	95
4.3.4	Charge sharing signal conditioning . . . . .	95
<b>5</b>	<b>Experiments with two cartridges</b>	<b>99</b>
5.1	Stepped point source measurements . . . . .	104
5.1.1	Energy resolution . . . . .	105
5.1.2	Time resolution . . . . .	106

5.1.3	Filtered back projection reconstruction . . . . .	110
5.2	Sensitivity measurements . . . . .	112
5.3	Point Spread Function (PSF) measurements . . . . .	114
5.4	Acquisition and image reconstruction of phantom data . . . . .	116
5.5	Conclusions from two cartridge experiments . . . . .	120
<b>6</b>	<b>Conclusion</b>	<b>121</b>

# List of Tables

2.1	Common scintillators used in PET . . . . .	13
2.2	PET photodetectors . . . . .	13
2.3	Definition of Figure of Merit (FoM) Metrics . . . . .	20
3.1	Electronics modules in cartridge . . . . .	41
4.1	Categorization of noise sources . . . . .	65
4.2	Multiplexing study SNR from SPICE simulations . . . . .	75
4.3	Multiplexing study coincidence time resolution . . . . .	83
4.4	Count Rate . . . . .	83
5.1	Stepped point source experiment results . . . . .	105

# List of Figures

2.1	Positron decay and annihilation . . . . .	4
2.2	Principle of PET . . . . .	5
2.3	True, scattered, and random coincidences . . . . .	6
2.4	Parallax error . . . . .	8
2.5	Explanation of time-of-flight PET . . . . .	11
2.6	Silicon avalanche photodiode . . . . .	14
2.7	Position Sensitive Avalanche Photodiode (PSAPD) . . . . .	17
2.8	Example of flood histogram . . . . .	18
2.9	Two common architectures for PET front-end electronics . . . . .	21
2.10	Charge sensitive amplifier . . . . .	22
2.11	Diagram for charge sensitive amplifier noise calculation . . . . .	23
2.12	Single resistor TIA . . . . .	25
2.13	Common gate TIA . . . . .	25
2.14	Noise contributors in common gate amplifier . . . . .	26
2.15	Shunt-shunt feedback transimpedance amplifier . . . . .	28
2.16	Shunt-shunt feedback transimpedance amplifier noise sources . . . . .	29
2.17	Shunt-shunt feedback transimpedance amplifier implementation . . . . .	29
2.18	Shunt-shunt feedback transimpedance amplifier small signal diagram . . . . .	30
2.19	Regulated cascode transimpedance amplifier . . . . .	32
2.20	Small signal diagram of a regulated cascode transimpedance amplifier . . . . .	32
2.21	Time walk . . . . .	35
2.22	Constant fraction discriminator (CFD) . . . . .	36
3.1	Imaging panels in two potential breast imaging orientations . . . . .	40



3.2	Panel of breast-dedicated PET system . . . . .	42
3.3	Picture of one cartridge . . . . .	43
3.4	Dual-LYSO-PSAPD module . . . . .	44
3.5	Stacking of Dual-LYSO-PSAPD modules . . . . .	45
3.6	Face-on versus edge-on . . . . .	46
3.7	A fin of detectors . . . . .	47
3.8	Pitch Adapter . . . . .	48
3.9	Fin epoxied to Pitch Adapter . . . . .	49
3.10	Programmable HV . . . . .	53
3.11	Picture of HV Floating Power Supply Board . . . . .	54
3.12	Picture of HV Bias Board . . . . .	54
3.13	Photograph of RENA Board . . . . .	56
3.14	Photograph of Discrete Board . . . . .	58
3.15	Overview of circuits on the Discrete Board . . . . .	59
3.16	Charge division circuit for the common signal . . . . .	60
3.17	Leakage current measurement circuit . . . . .	61
4.1	Simulation flow chart for creating a simulated flood histogram . . . . .	66
4.2	One subunit of the FEM circuit model for PSAPD . . . . .	68
4.3	Multiplexing circuit configuration . . . . .	72
4.4	Ceramic-mounted PSAPDs used in multiplexing study . . . . .	73
4.5	Multiplexing sensitivity experiment . . . . .	75
4.6	Multiplexing study simulation results: floods . . . . .	76
4.7	Multiplexing study simulation results: FoM analysis . . . . .	77
4.8	Multiplexing study experimental results: energy resolution . . . . .	77
4.9	Multiplexing study experimental results: time resolution . . . . .	78
4.10	Multiplexing study experimental results . . . . .	79
4.11	Multiplexing study experimental results: FoM analysis . . . . .	80
4.12	Multiplexing study experimental results: low energy windows . . . . .	82
4.13	Flood histogram with saturation . . . . .	85
4.14	Signal conditioning circuits for each spatial channel . . . . .	86

4.15	Capacitor-based signal conditioning scheme . . . . .	87
4.16	Flood histogram with shunt capacitor signal conditioning . . . . .	88
4.17	Resistor-based signal conditioning scheme . . . . .	89
4.18	Flood histogram with resistor-based signal conditioning . . . . .	90
4.19	Shunt resistor signal conditioning flood histograms . . . . .	91
4.20	Shunt resistor signal conditioning experimental results . . . . .	92
4.21	Shunt resistor signal conditioning simulation results . . . . .	93
4.22	1-dimensional simplification of the PSAPD . . . . .	94
4.23	SPICE simulation of an interaction near the corner of the PSAPD . . . . .	94
4.24	Series capacitor signal conditioning . . . . .	95
4.25	Asymmetric flood histograms . . . . .	96
4.26	Asymmetric flood histograms caused by parasitic capacitance . . . . .	97
4.27	Flood histogram with 43pF explicit charge sharing capacitors . . . . .	98
5.1	Picture of cartridge — top view . . . . .	101
5.2	Picture of cartridge — end view . . . . .	102
5.3	Picture of stack of detectors . . . . .	103
5.4	Experimental setup with translation stage . . . . .	103
5.5	Stepped point source experiment setup . . . . .	104
5.6	Energy spectrum for Dataset 1 . . . . .	106
5.7	Per-PSAPD energy resolution for Dataset 1 . . . . .	107
5.8	Per-PSAPD energy resolution for Dataset 1, for each fin . . . . .	108
5.9	Time difference histogram for Dataset 1 . . . . .	109
5.10	Per-PSAPD time resolution for Dataset 1 . . . . .	109
5.11	Filtered back projection image for Dataset 1 . . . . .	111
5.12	Na22 source at center of the FOV for sensitivity measurements . . . . .	112
5.13	Graphing the Point Spread Function . . . . .	115
5.14	PSF for a detector module near the center of the FOV . . . . .	115
5.15	PSF for a detector module near the edge of the FOV . . . . .	116
5.16	Phantom . . . . .	117
5.17	Reconstructed phantom normalization image . . . . .	117

5.18 Reconstructed phantom hot rod image . . . . .	118
5.19 Reconstructed phantom cold rod image . . . . .	119

# Chapter 1

## Introduction

Molecular imaging is a field that enables the visualization, characterization, and quantification of cellular and molecular pathways and mechanisms of disease within intact living subjects. Conventional anatomical imaging (e.g., standard X-ray, MRI, and ultrasound) primarily image structures inside the body and only detect the end effects of the molecular alterations associated with disease. In contrast, molecular imaging has the potential to detect disease at an earlier stage and provide a more fundamental understanding of its molecular pathways. Molecular imaging is an invaluable tool for detection of disease in patients, as well as for preclinical studies, basic science research, and drug development. Positron Emission Tomography (PET) is a type of in-vivo molecular imaging that can be used to image cancer, heart disease, neurological disorders, as well as other types of diseases.

A PET system produces an image of radiopharmaceuticals that have preferentially accumulated in certain cells of tissues in the body. PET can be used to image cancerous lesions in humans, but it still has difficulty resolving very small ( $<1\text{cm}$ ) structures. Improving the resolution of PET is an active area of research. This thesis describes a project that aims to push the resolution of PET down to  $1\text{mm}^3$ .

One field where improving the resolution of PET may have great contributions is breast cancer. Many studies have reported that PET has higher sensitivity and higher specificity than mammography, especially for patients with dense breasts. This thesis describes the development of a  $1\text{mm}^3$  resolution PET system for breast cancer

imaging, and the strategies used to overcome the challenges of designing such a high resolution system.

## 1.1 Thesis organization

Chapter 2 provides background information on Positron Emission Tomography (PET) applications, detectors, and electronics. It gives the motivation for high resolution PET, especially high resolution PET for breast cancer imaging, and explains how depth-of-interaction (DOI) can improve resolution. Chapter 2 also describes common PET detectors and front-end electronics architectures and circuits, as well as characterization metrics and methods.

I worked on a project to design a  $1\text{mm}^3$  resolution breast-dedicated PET system, and an overview of this system is in Chapter 3. The system has over 2000 dual detector modules connected to over 18,000 channels of electronics. I played a major role in designing the interconnect, detector high voltage bias distribution, signal conditioning methods, and system monitoring circuits for the system. These blocks are described in detail in Chapter 3.

I studied a multiplexing method to simplify the interconnect connecting the detectors to the electronics, described in Chapter 4. Chapter 4 also describes my study of signal conditioning methods to overcome the mismatch in dynamic range between the detectors and the front-end electronics. A PET detector and front-end electronics modeling and simulation framework, also described in Chapter 4, was used to study multiplexing and signal conditioning.

Chapter 5 presents results from two cartridges from this system. Chapter 6 concludes by summarizing the contributions of this work and future directions.

# Chapter 2

## PET Background

Positron Emission Tomography (PET) is an in-vivo medical imaging modality that extracts information about molecular processes associated with diseases such as cancer, heart disease, and neurological disorders. A PET system produces an image of radiopharmaceuticals, often referred to as “probes” or “tracers”, that have preferentially accumulated in certain cells of tissues in the body. A common PET probe used in cancer imaging is 2-[<sup>18</sup>F]fluoro-2-deoxy-D-glucose (FDG). FDG is a glucose analog where the 2' hydroxyl group in the glucose molecule has been substituted with the positron-emitting isotope fluorine-18. After intravenous injection into the patient, FDG is transported into the cell, mediated by glucose transport proteins (GLUT), just like glucose normally is. Then, it is phosphorylated by hexokinase as the first step towards glycolysis. The 2' hydroxyl group is necessary for the further steps of glycolysis, and since the 2' hydroxyl group is replaced by fluorine-18 in FDG, it is trapped intracellularly as FDG-6-phosphate (Rajadhyaksha et al., 2012). So, the concentration of FDG increases with time in proportion to the cell's glucose metabolic rate. Tumor cells are characterized by an increased glucose metabolism with respect to normal cells due to an increased number of glucose transporters, higher levels of hexokinase, and an increased rate of cell proliferation, protein and DNA synthesis, and angiogenesis, so they uptake and retain higher levels of FDG compared to normal tissues (Fanti et al., 2009). Therefore, FDG allows us to detect high levels of local glucose metabolism, a possible indication of tumor cells.

After the probe preferentially accumulates in certain cells in the patient, the positron-emitting isotope in the probe decays, emitting a positron. In the case of FDG, the positron-emitting isotope is fluorine-18, which decays with a half-life of 110 minutes. The positron annihilates with an electron, on average within a hundred microns of the decay location (the positron range (Levin and Hoffman, 1999)), and produces two anti-collinear (i.e., emitted in opposite directions,  $180^\circ$  apart) 511 kilo-electron-Volt (keV) photons called annihilation photons, as shown in Figure 2.1. These annihilation photons are also known as “511keV photons” or “high energy photons”.

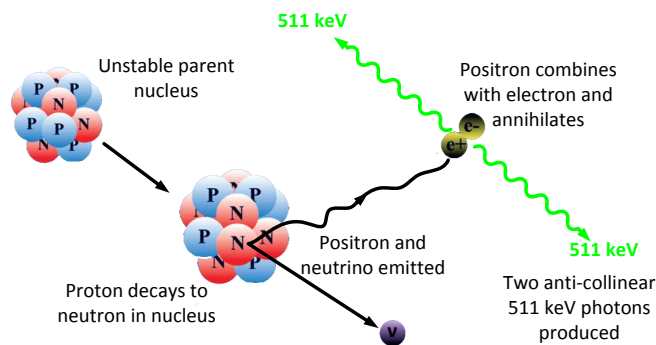


Figure 2.1: Positron decay and annihilation produces in two anti-collinear 511keV photons. Figure adapted from Wernick and Aarsvold (2004).

As illustrated in Figure 2.2, radiation detectors surrounding the patient capture these 511keV annihilation photons. Each pair of coincident 511keV photons is assigned to a line of response (LOR) joining the two detectors which detected the photons. By capturing a large number of coincident 511keV photons with detectors surrounding the object being imaged, the location of the annihilation can be estimated.

Radiation detectors convert the energy from the annihilation photons into charge pulses. As will be explained in further detail in Section 2.2, these radiation detectors are usually comprised of a scintillator plus a photodetector. A scintillator is a high density, high atomic number material which stops 511keV photons and converts them into visible light. The photodetector converts this visible light into charge pulses.

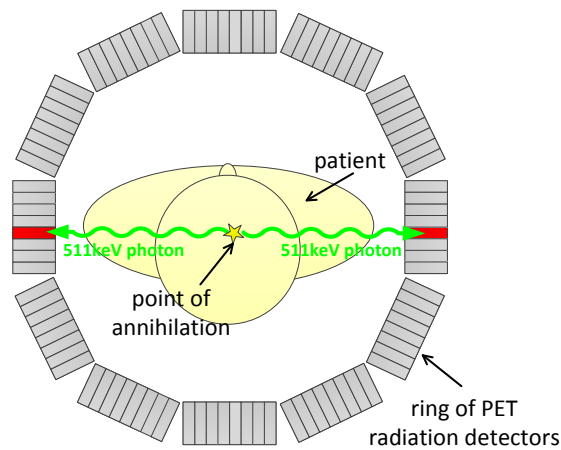


Figure 2.2: Principle of PET. In PET, the coincident 511keV annihilation photons emitted by the patient are captured by radiation detectors surrounding the patient.

These charge pulses are then processed and interpreted by electronics.

Not all pairs of annihilation photons captured are true coincident events (“true coincidences”) (see Figure 2.3). In some cases, one or both of the 511keV photons could have Compton scattered before hitting the detectors, so the line of response joining the two detectors does not pass through the location of the annihilation (“scattered coincidences”). The detected energy of these scatter events would be lower than 511keV though, so PET systems try to identify (and possibly reject) these events by measuring the energy of the photons detected. In other cases, “random coincidences” occur where two 511keV photons are captured from two independent radionuclei from two locations of annihilation, and mistakenly paired because they were both detected within the coincident time window of the system. The line of response in this case also incorrectly estimates the location of the annihilation.

In order to distinguish true coincidences from scattered or random coincidences without discarding a large fraction of events, a PET system needs to have good photon sensitivity, energy resolution and time resolution. These PET performance metrics are explained in the next section.



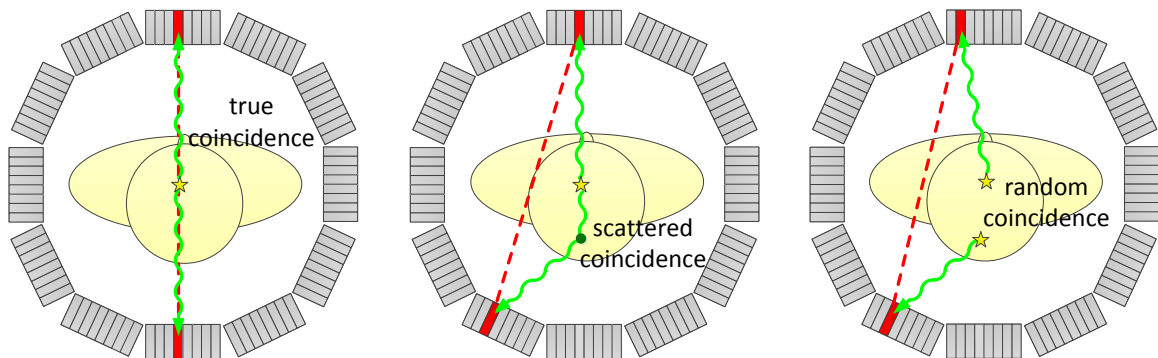


Figure 2.3: Three types of coincidences: (left) true coincidence; (middle) tissue scattered coincidence; and (right) random coincidence. The yellow star indicates the location of the annihilation. The red dashed line represents the line of response (LOR) recorded by the system. For scattered and random coincidences, the LOR does not pass through the point of annihilation.

## 2.1 PET system performance metrics

A PET system is characterized by evaluating its photon sensitivity, spatial resolution, and contrast resolution.

### 2.1.1 Photon sensitivity

The photon sensitivity of a PET system is the fraction of the coincident 511keV photons emitted from the object being imaged that is detected by the system. A higher photon sensitivity results in a shorter scan time, lower dose to the patient, and/or better statistical image quality. The photon sensitivity of a PET system can be improved by increasing geometric efficiency, i.e., the probability that the annihilation photons will traverse detector material. This is done by surrounding the imaging subject with as much detector material as possible, by bringing the detectors close to the imaging subject, and by ensuring gaps between detectors are small (Levin, 2005). The photon sensitivity can also be improved by increasing the intrinsic photon detection efficiency (i.e., the 511keV stopping power) by fabricating the detectors with denser, higher atomic number ( $Z$ ), and thicker (longer) detector elements.

### 2.1.2 Spatial resolution

A PET system must be able to distinguish between annihilation events originating from different locations within the imaging subject in order to form a quality image, i.e., it must have good spatial resolution. The two fundamental limits to the spatial resolution of PET result from the positron range and from the noncollinearity of the annihilation photons. For fluorine-18 positrons, positron range limits the spatial resolution to be above 0.1mm full-width-at-half-maximum (FWHM) (Levin and Hoffman, 1999). Annihilation photon non-collinearity results in a small angular deviation of about  $0.25^\circ$  FWHM. The translation of this angular deviation into spatial resolution depends on the distance between the detectors capturing the two opposing photons. For example if the detectors are 10 cm apart, the spatial resolution limit due to non-collinearity is 0.22 mm (Levin and Hoffman, 1999).

The resolution of current PET systems is not restricted by these fundamental limits yet. The main constraint to spatial resolution is the size of the detector elements since it determines how precisely the system can localize the annihilation photons. The size of detector elements used in PET systems has decreased over time. Currently, the dimension of detector elements in the x- and y-direction (i.e., the directions perpendicular to the incoming photons) is about 4-6 mm for clinical systems and 1-2 mm for application specific or small animal systems. The dimension in the z-direction (i.e., the direction parallel to the incoming photons, the depth of interaction direction) is generally larger, usually more than one centimeter, because that is required for sufficient probability of 511keV photon interaction in the detector (Wernick and Aarsvold, 2004, p. 240), as will be explained in Section 2.2.1 on scintillators. Measuring depth-of-interaction is one method to improve the resolution in the z-direction.

#### Depth-of-interaction techniques in PET

The large z-dimension of PET detector elements causes an effect called parallax error. As illustrated in Figure 2.4, when 511keV photons interact at oblique angles there is non-uniform spatial resolution that varies as a function of radial position.

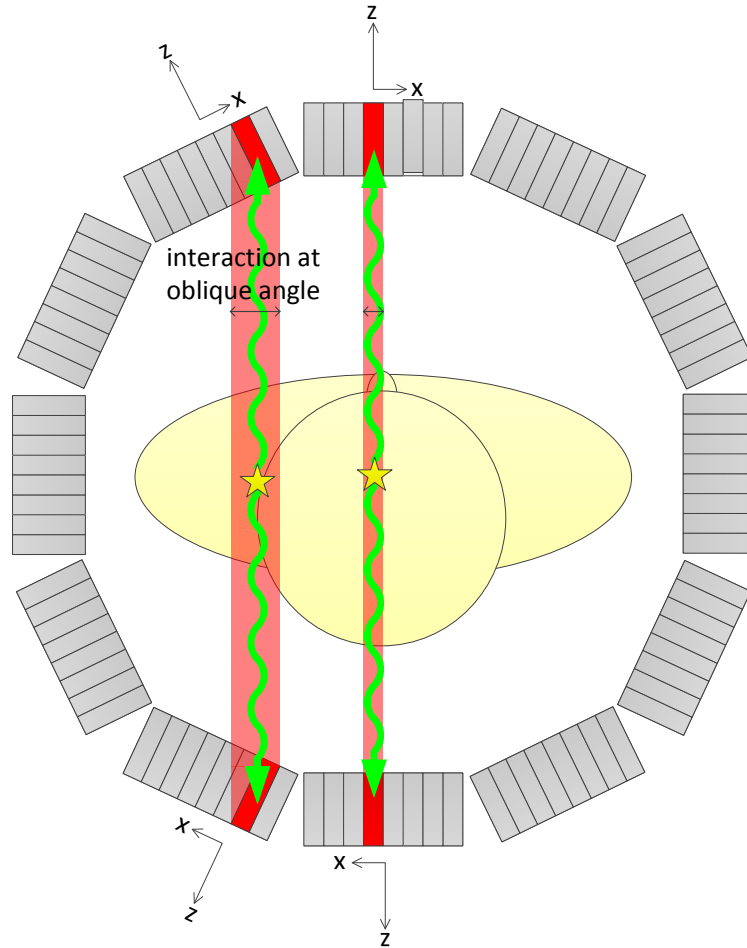


Figure 2.4: Parallax error occurs when photons interact at oblique angles with respect to detectors that do not have depth-of-interaction capability, resulting in non-uniform spatial resolution that varies as a function of radial position within the system. The uncertainty in the spatial positioning is indicated in light red.

Depth-of-interaction (DOI) detectors reduce parallax error by providing z-coordinate information (i.e., information about the depth of the interaction inside the detector) (Peng and Levin, 2010). Approaches include dual-ended readout with photodetectors on both ends of the scintillation crystals, phoswich detectors which use different types of scintillation crystal materials, and statistical positioning with monolithic crystals. DOI information can also be obtained with 3-D positioning photodetectors. We chose this latter approach in this thesis, and designed a detector with thin photodetectors sandwiched between arrays of  $1\text{x}1\text{x}1\text{mm}^3$  scintillation crystals, allowing interactions to be positioned to the nearest 1mm crystal element in all three dimensions. By reducing parallax error, depth-of-interaction PET detectors increase the resolution uniformity of PET, essential for earlier detection of disease and imaging of smaller structures.

### 2.1.3 Contrast resolution

The ability to visualize and accurately quantify the distribution of the concentrations of probe in the imaging subject depends on the contrast in the image. Contrast resolution is important for differentiating between tumor and background, reducing the scan time, and/or lowering the radioactive dose. Although the contrast is defined by the biodistribution of the probe to first order, the energy resolution and time resolution of a PET system affect the resulting contrast resolution.

#### Energy resolution

Energy resolution is the precision with which the PET system can measure the incoming annihilation photon energy. The energy of true coincidences should ideally be exactly 511keV. However, due to noise in the detectors or electronics, there is a variance in the measured energy. Good energy resolution enables a narrow energy window around 511keV to be defined, allowing the system to identify (and possibly reject) scattered coincidences without sacrificing system sensitivity. Many random coincidences are also a result of scatter, so a narrow energy window can also identify these cases.

The energy resolution of a PET system is characterized by plotting a histogram of energies measured (called an “energy spectrum”), fitting a function such as a Gaussian to the 511keV photopeak, and determining the full-width-at-half-maximum (FWHM) of the Gaussian fit. The FWHM is usually reported as a percentage, where the width in keV is divided by 511keV and multiplied by 100.

### **Time Resolution**

The time resolution is the precision in which the PET system can identify events that really originated from the same annihilation event. Neglecting the time of flight of the photon, the time difference between true coincident events should ideally be zero, but there is a variance in the measured time difference due to noise or measurement inaccuracies in the detectors or electronics. Good time resolution allows a narrow time window to be defined, enabling the system to identify (and possibly reject) random coincidences without compromising system sensitivity.

The time resolution of a PET system is determined by plotting a histogram of the time difference between events, fitting a Gaussian to the histogram, and reporting the FWHM of the Gaussian fit.

The energy and time resolution affect the contrast of the resulting image because they allow mis-positioned events with LORs that do not pass through the actual point of annihilation to be identified (and possibly rejected).

### **Time-of-Flight PET**

Time-of-flight PET is a technique for improving PET image contrast resolution that has gained popularity in the past few years. Recent improvements in PET detectors have lowered time resolution from a few nanoseconds to less than 300 picoseconds. This has allowed PET systems to estimate where along a LOR the annihilation occurred. As shown in Figure 2.5, instead of just assuming the annihilation occurred somewhere along the LOR, the time difference  $\Delta t$  in the time stamps of the two events can be used to estimate the position  $\Delta x$  of the annihilation point, with respect to the center of the field of view, using the formula below, where  $c = 3.8 \times 10^8$  m/s is the

speed of light:

$$\Delta x = \frac{c\Delta t}{2} \quad (2.1)$$

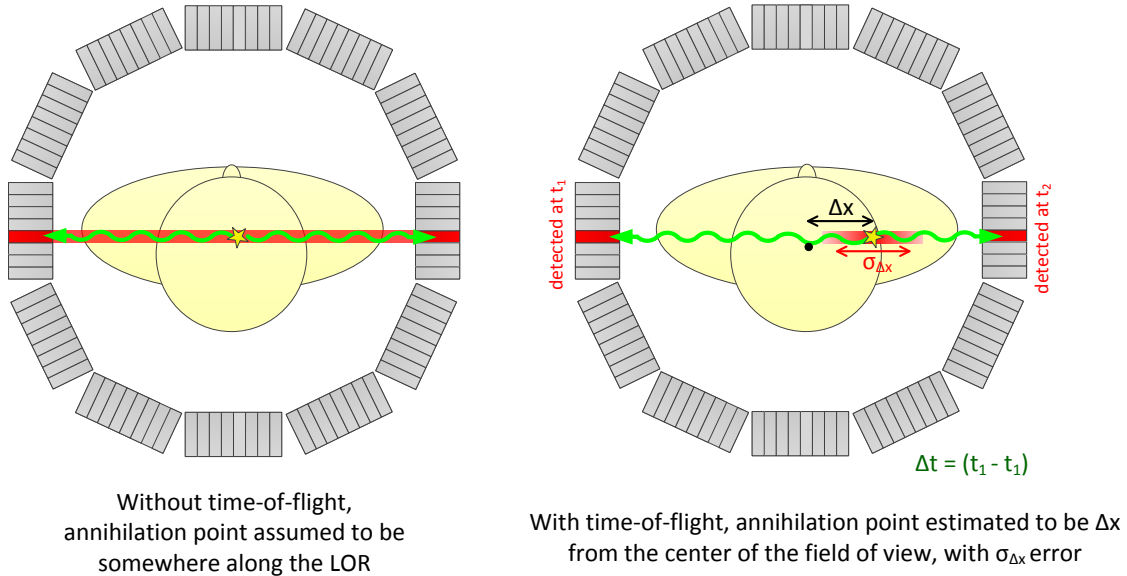


Figure 2.5: With time-of-flight PET, it is possible to estimate where along the LOR the point of annihilation occurred using the time difference  $\Delta t$  between the events. This estimate is limited by the time resolution of the system,  $\sigma_{\Delta t}$ .

If the time resolution of the PET detectors and electronics is 300ps, this translates into a position blurring of 4.5cm according to Equation 2.1, rather than over the entire LOR. So, time-of-flight is only useful if the time resolution is good and if the patient has a large diameter. Time-of-flight PET can increase the SNR and contrast of the reconstructed image, resulting in better lesion detectability, reduced scan time, and/or lower radioactive dose.

## 2.2 PET detectors

PET detectors are radiation detectors that convert annihilation photons into charge pulses. Most PET detectors do this conversion in two steps: a scintillator stops the 511keV photons and converts them into visible or ultraviolet light, and then a

photodetector converts this light into charge pulses. The charge pulses are processed by analog electronics.

Radiation detectors which convert the 511keV photons directly into charge also exist. These one-step radiation detectors are made out of semiconductor materials such as Cadmium zinc telluride (CdZnTe, or CZT) or Cadmium telluride (CdTe). The advantage of CZT or CdTe detectors is they have superior energy resolution ( $<4\%$  FWHM) (Gu et al., 2011), but the disadvantage is that the time resolution is worse due to temporal variance in the collection time of charge carriers in the detector (5-26 ns FWHM, depending on detector geometry (Gu and Levin, 2011; Okada et al., 2002; Shao et al., 2000)). This thesis will focus on the two-step detectors which comprise scintillation crystals and photodetectors.

### 2.2.1 Scintillators

Scintillators are materials that absorb ionizing radiation and convert some of the absorbed energy into visible or ultraviolet photons. Scintillators exist in a variety of forms, including inorganic, organic, liquid, plastic, crystalline, and non-crystalline. Most scintillators used in PET are inorganic crystals because those generally have higher density and atomic number, important for stopping the high energy 511keV photons. Some common scintillation materials in PET include sodium iodide activated with thallium (NaI(Tl)), bismuth germanate oxide (BGO), gadolinium oxyorthosilicate (GSO), lutetium oxyorthosilicate (LSO), and lutetium yttrium oxyorthosilicate (LYSO) (Melcher, 2000). These are summarized in Table 2.1.

LSO is an attractive scintillator due to its relatively high light output, fast decay time, emission wavelength at 420nm which matches many photodetectors, and high density. Typical measurements of energy resolution are about 10-12% (Knoll, 2000; Pepin et al., 2004). The disadvantage of LSO is that it is difficult and expensive to produce due to its high melting point ( $> 2000^{\circ}\text{C}$ ) and due to the high cost of raw lutetium oxide. LYSO is a good substitute for LSO since their properties are similar and LYSO is lower cost. The cost of raw yttrium oxide is several times less expensive than raw lutetium oxide and the melting point is  $100^{\circ}\text{C}$  less (Kimble et al.,

Table 2.1: Common scintillators used in PET

Scintillator	Chemical Formula	Density (g/cm <sup>3</sup> )	Effective Atomic Number	Light Output (Photons/ MeV)	Decay Constant (ns)	Emission Wavelength (nm)
<b>NaI(Tl)</b>	NaI(Tl)	3.67	51	37,700	230	415
<b>BGO</b>	Bi <sub>4</sub> (GeO <sub>4</sub> ) <sub>3</sub>	7.13	76	8,200	300	505
<b>GSO</b>	Gd <sub>2</sub> SiO <sub>5</sub>	6.71	59	10,000	60	430
<b>LSO</b>	Lu <sub>2</sub> (SiO <sub>4</sub> )O:Ce	7.40	65	30,000	40	420
<b>LYSO</b>	Lu <sub>2-x</sub> Y <sub>x</sub> SiO <sub>5</sub> :Ce	6.5	63	27,000	40	420

Table 2.2: Common PET photodetectors (adapted from (Spanoudaki and Levin, 2010; Wernick and Aarsvold, 2004))

	<b>PMT</b>	<b>APD</b>	<b>SiPM</b>
<b>Gain</b>	10 <sup>6</sup> – 10 <sup>7</sup>	50-1000	~ 10 <sup>6</sup>
<b>Rise time (ns)</b>	1-3	2-5	~ 1
<b>Detection efficiency at 420nm (%)</b>	~ 25 (quantum efficiency)	~ 70 (quantum efficiency)	25-75 (photon detection efficiency)
<b>Bias voltage (V)</b>	> 1000	300-2000	30-80
<b>Temperature sensitivity (<math>\frac{\%}{\circ C}</math>)</b>	< 1	~ 3	1-8
<b>Magnetic field sensitivity</b>	yes	no	no

2002). Therefore, the breast imaging system described in this thesis uses LYSO for the scintillator.

## 2.2.2 Photodetectors

After the scintillator converts the high energy photon into visible or ultraviolet light, a photodetector converts the light into electrical charge. There are several types of photodetectors used in PET, summarized in Table 2.2. Most PET systems in existence use photomultiplier tubes, but recent PET systems have shifted to using semiconductor photodetectors such as avalanche photodiodes and silicon photomultipliers.

### Photomultiplier tubes (PMTs)

A photomultiplier tube (PMT) is a vacuum tube that converts light photons into amplified charge pulses. A photosensitive cathode in the PMT emits electrons in response to light, and an electron multiplier structure (dynode) amplifies the signal. After multiplication, the charge is collected at the anode. The advantage of PMTs is their high gain of 10<sup>6</sup>-10<sup>7</sup> and their fast rise time. The disadvantage of PMTs is their large bulky size and low quantum efficiency. PMTs are also sensitive to magnetic



fields so they are ill-suited for imaging systems that combine PET and Magnetic Resonance Imaging (PET-MRI systems).

### Avalanche photodiodes (APDs)

An avalanche photodiode (APD) is a semiconductor photodiode that has a multiplication region with a large electric field, as illustrated in Figure 2.6. When light is incident on the photodiode, electron-hole pairs are created in the drift p-region. The charge carriers drift to the depleted multiplication region, where the high electric field causes an avalanche process where additional electron-hole pairs are created by impact ionization. The depleted layers are made thick to reduce the device capacitance.

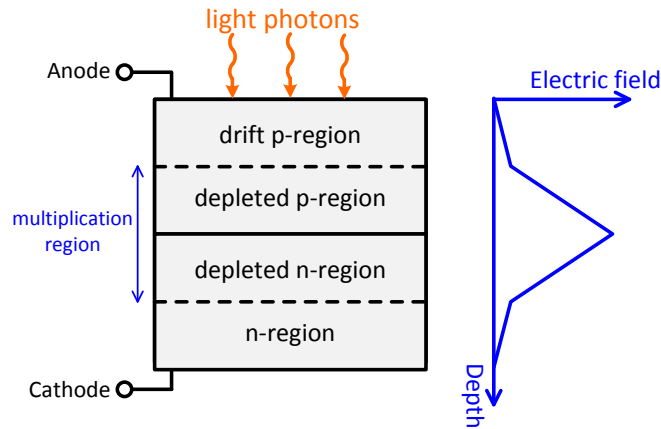


Figure 2.6: Basic structure for a silicon avalanche photodiode and plot of the electric field in the device

The noise of APDs is primarily from shot noise due to random statistical fluctuations in the leakage current. In an APD, the total leakage current  $I_D$  is equal to:

$$I_D = I_{DS} + I_{DB}M \quad (2.2)$$

where  $I_{DS}$  = surface leakage current

$I_{DB}$  = bulk leakage current

$M$  = APD gain

The shot noise without signal present (dark noise) is equal to (McIntyre, 1966):

$$i_n = \sqrt{2q(I_{DS} + I_{DB}M^2F)B} \quad (2.3)$$

where  $F = k_{eff}M + (1 - k_{eff})(2 - \frac{1}{M})$

$F$  is an excess noise factor due to the statistical nature of the avalanche process, and is dependent on the effective carrier ionization ratio ( $k_{eff}$ ).  $k_{eff}$  is the ratio of hole to electron ionization probabilities, after accounting for the electric field profile of the APD.  $B$  is the bandwidth over which the noise is integrated.

When there is signal present, the total shot noise is due to both the dark leakage current and the signal current. For a given incident optical signal power  $P_s$ , APD intrinsic responsivity  $R_o$ , and APD gain  $M$ , the total shot noise is (Elmer, 2010):

$$i_n = \sqrt{2q(I_{DS} + (I_{DB} + R_oP_s)M^2F)B} \quad (2.4)$$

APDs are much smaller in size compared to PMTs. This is important in applications where, for example, a photodetector needs to be placed on both ends of a scintillation crystal to create a depth-of-interaction (DOI) detector. APDs are insensitive to magnetic fields and are used in PET-MRI systems. The disadvantage of APDs include their slower response time and temperature-dependent gain. Also, the gain of APDs is usually around 50-300, much lower than that of PMTs. In this thesis, we study an APD manufactured by Radiation Monitoring Devices (RMD) with an exceptionally high gain of about 1000. The trade-off is that it requires a very high bias voltage of 1750V to create the large gain.

### Silicon photomultipliers

Silicon photomultipliers (SiPMs) have emerged in the past few years as an alternative to PMTs. Also known by names such as solid-state photomultipliers (SSPMs), multi-pixel photon counters (MPPCs), or Geiger-mode APDs, these devices are arrays of avalanche photodiode micro-cells which operate in Geiger-mode. These micro-cells are biased above their breakdown voltage, and therefore produce much larger currents

compared to APDs. In order to stop the breakdown, a quenching resistor is placed in series with the detector. When current is generated by the detector, the voltage drop across the resistor increases, which limits the bias voltage across the device and thus the breakdown.

Each of these micro-cells produces a “digital” signal, providing information about the detection of light but not about the intensity of the light. By summing the outputs of all the micro-cells together, the overall device is able to measure the number of incident photons, and thus the intensity of the light.

SiPMs have gains and rise times comparable to PMTs, are insensitive to magnetic fields, are compact in size, and require much lower bias voltages. They are emerging in popularity in applications that require fast timing, such as time-of-flight PET.

One limitation of SiPMs is its trade-off between photon detection efficiency (PDE) and dynamic range (Spanoudaki and Levin, 2010). A large dynamic range in response to the intensity of incident light needs a large number of micro-cells. However, a large number of micro-cells results in more dead area between the micro-cells, for the same overall SiPM detector area. Another disadvantage is its temperature dependent gain, so temperature regulation is usually needed.

### **Position Sensitive Avalanche Photodiodes (PSAPD)**

Avalanche photodiodes can be fabricated with a resistive sheet on one side, with contacts on the four corners of the resistive sheet. This device, called a Position Sensitive Avalanche Photodiode (PSAPD) (Shah et al., 2002; Zhang et al., 2007a) can readout a large number of scintillation crystal pixels with only a few electronics channels. The resistive sheet allows interactions to be positioned by evaluating the position-dependent charge splitting.

The Position Sensitive Avalanche Photodiode (PSAPD) used in this thesis is fabricated by Radiation Monitoring Devices (RMD), Inc (Watertown, MA) (Shah et al., 2002). As shown in Figure 2.7, this PSAPD has four corner contacts, called “spatial channels”, on a resistive sheet on the n-doped side for positioning interactions using a position dependent charge splitting. The p-doped side has one contact that is called the “common”. The quantum efficiency is about 60%. The device capacitance is

quite large, about 45-50pF (Dokhale et al., 2004). It has a gain of about 1000 and needs 1750V reverse bias voltage across the device to achieve this gain. Since there are four spatial channels versus only one common contact, the common contact is usually connected to -1750V through a bias resistor to allow the four spatial channels to be connected to ground through a bias resistor. The charge generated in the PSAPD from one 511 keV photon interacting in the LYSO array is about 1pC. The leakage current (dark current) is about 1uA at a bias voltage of 1750V. In this thesis, this PSAPD from RMD was used to readout an 8x8 array of scintillation crystals. The  $(x, y)$  coordinate of the interaction is calculated using equations similar to what is known as the Anger logic formula (Anger, 1958), where  $A, B, C, D$  is the signal measured at the four spatial channel corners:

$$\begin{aligned} x &= \frac{(A - B) + (D - C)}{A + B + C + D} \\ y &= \frac{(A - D) + (B - C)}{A + B + C + D} \end{aligned} \quad (2.5)$$

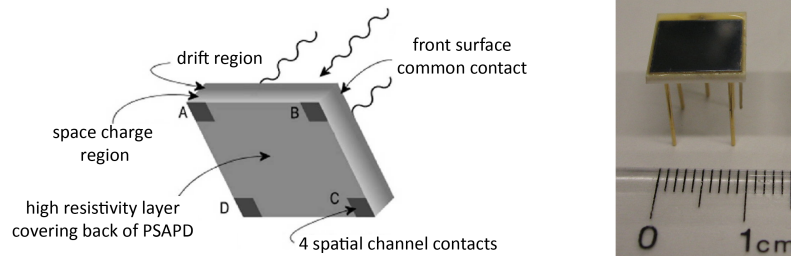


Figure 2.7:

Left: The Position Sensitive Avalanche Photodiode from RMD has a high resistivity layer covering the back side with four contacts, A, B, C, and D (called “spatial channels”). The front surface contact is called the “common”. Figure from (Shah et al., 2002).

Right: Photograph of a PSAPD from RMD, mounted on a ceramic substrate.

The spatial performance of this detector is characterized using a flood histogram. A flood histogram is produced by flood irradiating the detector with a radioactive source. The  $(x, y)$  coordinates of all the interactions are computed and a histogram is plotted. An example of a flood histogram produced by the PSAPD from RMD

coupled with a  $8 \times 8$  LYSO scintillation crystal array is in Figure 2.8. 64 peaks are seen in the flood histogram, corresponding to events occurring in each of the 64 crystals in the array. The flood histogram has a pin-cushion distortion due to the non-linearity of charge sharing between contacts from the PSAPD's sheet resistance.

The distance between the peaks in the flood histogram and the width of the peaks indicate the likelihood of correctly assigning an event to the crystal in which the interaction actually occurred (it's crystal identification ability). Therefore, the spatial resolution capabilities of the PSAPD can be predicted from its flood histogram. Strictly speaking, the flood histogram is not a perfect indicator of the detector spatial resolution since there is the chance that an interaction in one crystal appears right in the center of the peak corresponding to another crystal in the flood histogram. A better way to measure the spatial resolution would be to scan a collimated radioactive source across the detector because then it would be known where the interaction actually occurred. A procedure to do this is described in Section 5.3.

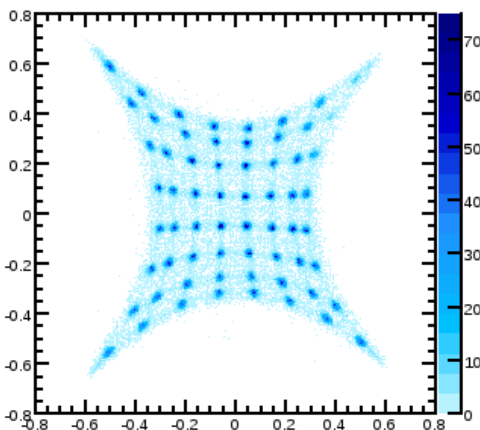


Figure 2.8: Example of a flood histogram from a PSAPD coupled to an  $8 \times 8$  array of  $1\text{mm}^3$  LYSO scintillation crystals

We developed a method to quantitatively analyze the flood histogram (Lau et al., 2010). First, 64 peaks were identified in the flood histogram using a peak finding algorithm (e.g., using Matlab or using the peak finding algorithm (Morh et al., 2000) as implemented in the ROOT data analysis software (Brun and Rademakers, 1997)). Then, a minimum distance norm was used to assign each individual event to one of

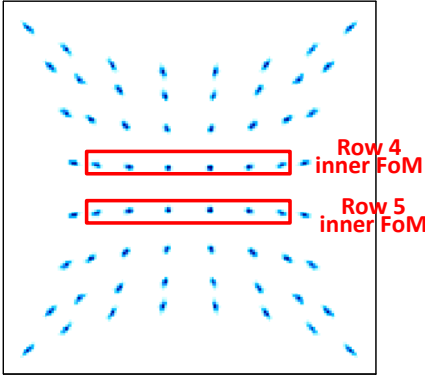
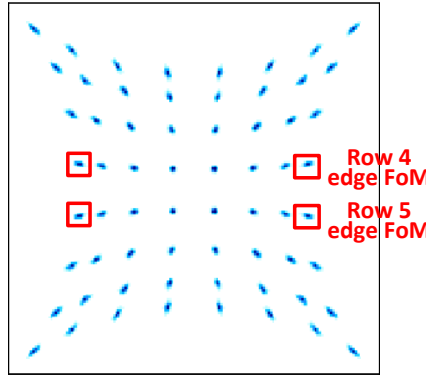
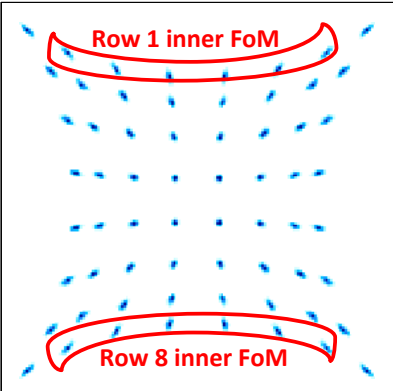
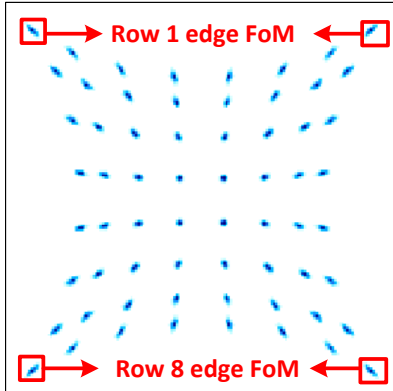
the 64 crystals. A Gaussian was fit to the histogram of the x-coordinates for every crystal for those events with energy within three sigma of the photopeak. For each row of peaks, the distance between adjacent peaks (as measured from the mean of the Gaussian fits) and the FWHM of the Gaussian fits were combined into a Figure of Merit (FoM) metric:

$$FoM = \frac{\text{avg distance between adjacent peaks in flood}}{\text{avg width (FWHM) of peaks in flood}} \quad (2.6)$$

There are systematic differences between the characteristics of the peaks in the inner portion of each row and the edge of each row due to the pin-cushion effect and non-uniform gain across the PSAPD. Therefore, two separate FoM metrics were calculated for each row. As explained in Table 2.3, the inner FoM is computed using the inner six peaks in the row, whereas the edge FoM is computed using the peak on the left-hand-side edge and the peak on the right-hand-side edge in the row. All the crystals were analyzed, but sometimes to condense the results, we only report the FoM for the “middle-rows” and the “outer-rows” using the following definitions: FoM for the “middle-rows” is the average FoM for Row 4 and Row 5, and FoM for the “outer-rows” is the average FoM for Row 1 and Row 8.

Measurements made with PSAPDs coupled with scintillation crystal arrays exhibit differences in gain depending on which crystal in the array the interaction occurred. These gain differences are due to the non-uniform gain of the PSAPD and the non-uniform light yield of the scintillation crystals. Therefore, it is necessary to compensate for per-crystal gain differences. To characterize the energy resolution of a PSAPD, first, a separate energy spectrum for the events assigned to each crystal in the 8x8 array was plotted, and the 511keV photo-peak position for each crystal was determined by a Gaussian fit. Then, each spectrum was scaled so that their 511keV photo-peaks lined up with each other and inter-channel offset from the electronics was removed. The scaled spectra from all the crystals were then combined to produce a single overall per-crystal gain corrected energy spectrum. A function, such as a Gaussian, was fit to the 511keV photo-peak of this overall energy spectrum, and the FWHM of this photo-peak fit was reported as the energy resolution.

Table 2.3: Definition of Figure of Merit (FoM) Metrics

	inner FoM	edge FoM
middle rows		
outer rows		

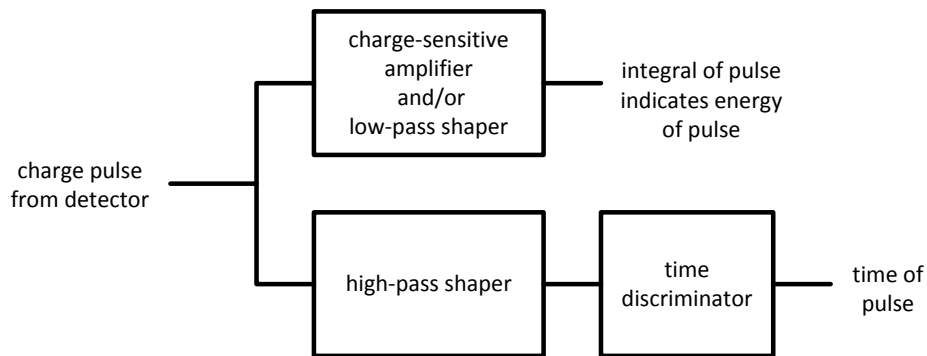
PMTs and silicon photomultipliers can also be fabricated with a resistive sheet on one side to create Position Sensitive Photomultiplier Tubes (PMTs) (Kume et al., 1985) and Position Sensitive Solid-State Photomultipliers (PS-SSPMs) (McClish et al., 2010). Some topics in this thesis for PSAPDs are also applicable to these detectors.

## 2.3 Front-end electronics

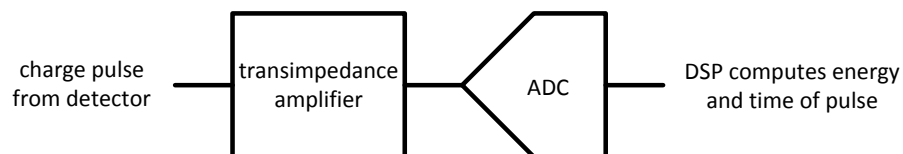
After the PET detector converts the scintillation photon into a charge pulse, the pulse is processed by the electronics. Two common architectures for the electronics are shown in Figure 2.9. In the first approach, the analog signal is split into two paths — one for energy measurement and one for time measurement. This avoids the

problem of optimizing the system for energy measurement and time discrimination simultaneously since energy measurement requires low noise in the integral of the pulse whereas time discrimination requires low jitter in the rising edge of the pulse. The RENA-3 Application Specific Integrated Circuit (ASIC) used in the breast cancer imaging system described in this thesis uses this architecture. The second configuration uses analog electronics which preserve the shape of the original pulse waveform (e.g., transimpedance amplifier). An analog-to-digital converter (ADC) then samples and digitizes the signal and digital signal processing extracts the energy and time information from the digitized waveform.

Both of these configurations are comprised of electronics as building blocks which can be roughly grouped into five categories: 1) charge-sensitive amplification, 2) transimpedance amplification, 3) time discrimination, 4) shaping, and 5) waveform digitization. The following sections will describe the five types of building blocks.



(a) The signal is split into two paths, one for energy measurement and one for time measurement



(b) The pulse waveform is digitized and digital signal processing (DSP) extracts both energy and time information

Figure 2.9: Two common architectures for PET front-end electronics



### 2.3.1 Charge-sensitive amplification

In a PET system, the charge in the pulse may be computed using analog circuits or using digital signal processing. If the analog option is chosen, a charge sensitive amplifier is usually used. This amplifier integrates the charge in the current pulse on its feedback capacitor. Figure 2.10 shows a charge-sensitive amplifier with a feedback capacitor  $C_F$ . It is connected to a detector that is modelled by a current source and a capacitor  $C_D$ .  $Q_{IN}$  is the charge from the detector. Assuming the amplifier is an inverting amplifier with a large gain  $A$  and a high input impedance, all the signal current flows into the feedback capacitance so  $Q_F = Q_{IN}$ . The voltage across  $C_F$  is  $v_F = (A + 1)v_{IN}$ . The input capacitance  $C_{IN}$  is magnified by the open loop gain of the amplifier (Spieler, 2005):

$$C_{IN} = \frac{Q_{IN}}{v_{IN}} = \frac{Q_F}{v_{IN}} = \frac{C_F v_F}{v_{IN}} = \frac{C_F(A + 1)v_{IN}}{v_{IN}} = C_F(A + 1) \quad (2.7)$$

The magnitude of the output voltage  $v_{OUT}$  is

$$v_{OUT} = Av_{IN} = A \frac{Q_{IN}}{C_F(A + 1)} \approx \frac{Q_{IN}}{C_F} \quad (2.8)$$

The conversion from charge to voltage is not dependent on the detector capacitance as long as the input capacitance  $C_{IN}$  is much larger than the detector capacitance.

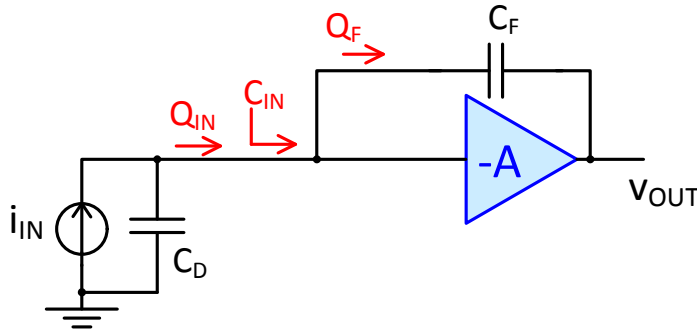


Figure 2.10: Charge sensitive amplifier

Noise, however, does depend on the detector capacitance  $C_D$ . The SNR is higher with lower  $C_D$  because the amplifier noise, modeled at the amplifier input as a noise

voltage source  $v_{nA}$ , passes through the amplifier and is fed back to the input, appearing as  $v_{nf}$  with opposite phase.  $v_{nf}$  decreases the output noise from its open loop value. The magnitude of the fed back signal depends on the capacitor divider at the input (created by  $C_D$  and  $C_F$ ) and increases with decreasing  $C_D$ . So, the output noise decreases with  $C_D$  whereas the output signal is independent of  $C_D$  (Equation 2.8). A derivation of this follows.

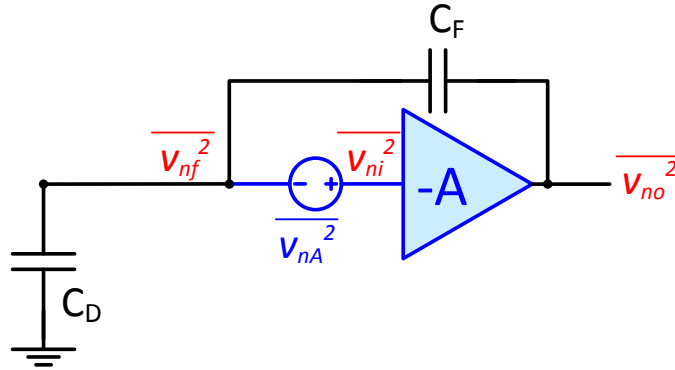


Figure 2.11: Diagram for charge sensitive amplifier noise calculation

Capacitor divider at input: 
$$v_{no} = v_{nf} \frac{C_F + C_D}{C_F} \quad (2.9a)$$

Also: 
$$\begin{aligned} v_{no} &= -A v_{ni} \\ &= -A(v_{nf} + v_{nA}) \end{aligned} \quad (2.9b)$$

Substituting 2.9b into 2.9a, 
$$\begin{aligned} v_{no} &= v_{nf} \frac{C_F + C_D}{C_F} \\ -A(v_{nf} + v_{nA}) &= v_{nf} \frac{C_F + C_D}{C_F} \\ v_{nf} &= -v_{nA} \frac{1}{1 + \frac{1}{A} + \frac{C_D}{AC_F}} \end{aligned} \quad (2.9c)$$

If  $(A \gg 1)$  and  $(AC_F \gg C_D)$ , 
$$v_{nf} \approx -v_{nA} \quad (2.9d)$$

So, the equivalent noise charge (ENC) at the input is

$$Q_{ni} = |v_{no}|C_F \quad (\text{From Equation 2.8})$$

$$= |v_{nf}| \frac{C_F + C_D}{C_F} C_F \quad (\text{From Equation 2.9a})$$

$$\approx |v_{nA}|(C_F + C_D) \quad (\text{From Equation 2.9d})$$

The signal is  $Q_{IN}$ , so the signal-to-noise ratio is

$$SNR = \frac{Q_{IN}}{Q_{ni}} = \frac{Q_{IN}}{|v_{nA}|(C_F + C_D)} \quad (2.9e)$$

$$\approx \frac{Q_{IN}}{|v_{nA}|C_D} \quad (\text{if } C_D \gg C_F) \quad (2.9f)$$

The SNR is higher when the detector capacitance  $C_D$  is lower because the noise decreases but the signal stays the same. This increase in noise as a function of capacitance is called the noise slope.

The charge sensitive amplifier is good for low noise applications since the integration operation averages noise out. The disadvantage is that the resulting pulse has a slow rise time, roughly equal to the decay time of the pulse from the detector (Knoll, 2000, p.296), so it is not suitable when low jitter in determining the time of the pulse rising edge is a priority.

### 2.3.2 Transimpedance amplification

For applications where it is important to preserve the fast rising edge of the pulse, such as in Time-of-Flight PET, a transimpedance amplifier is often used. Razavi (2003) provides an excellent description of transimpedance amplifier architectures, from which this section is based.

#### Single Resistor TIA

The simplest type of transimpedance amplifier that could be used to convert a photodetector current into a voltage is simply a resistor, for example,  $R_L$  in Figure 2.12.

The transimpedance gain is  $R_L$  and the bandwidth is limited by the time constant  $R_L C_D$ . The total integrated output noise is  $\overline{v_{n,out}^2} = \frac{kT}{C_D}$ , which, when referred to the input, results in a total input-referred noise current of  $\overline{i_{n,in}^2} = \frac{kT}{R_L^2 C_D}$  (Razavi, 2003, p.63). Therefore, a large  $R_L$  is necessary for low noise and high transimpedance gain, but it directly degrades bandwidth. Although simple, this architecture may not be sufficient for high performance applications.

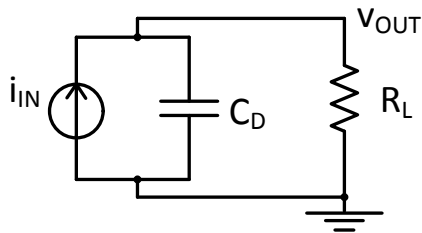


Figure 2.12: A resistor acts as a transimpedance amplifier with gain  $R_L$  for a photodetector with capacitance  $C_D$

### Common Gate TIA

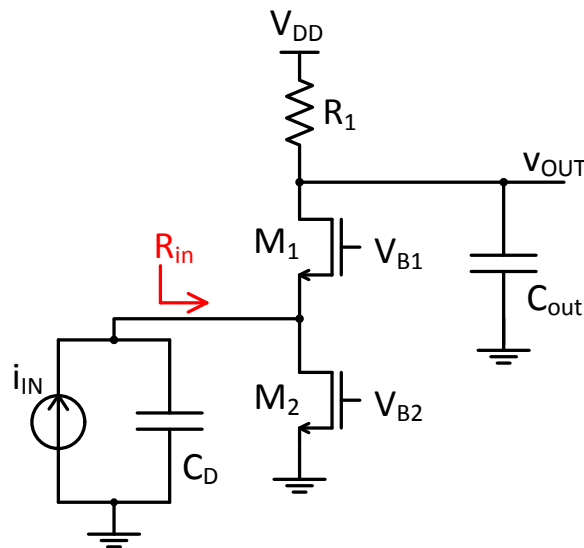


Figure 2.13: Common gate transimpedance amplifier with main transistor  $M_1$  and bias transistor  $M_2$  for a photodetector with capacitance  $C_D$ .

A common gate (or common base) amplifier can be used to relax the tight trade-off between bandwidth and noise in the single resistor architecture by simultaneously providing a low input impedance and a high gain. The input impedance is approximately equal to  $Z_{in} = 1/g_{m1}$ , where  $g_{m1}$  is the transconductance of the input transistor  $M_1$ . The input time constant,  $R_{in}C_{in}$ , is usually the time constant which limits the circuit bandwidth. The bandwidth can be increased by increasing the current and the width of  $M_1$  to increase  $g_{m1}$  and thus lower  $R_{in}$ , but this strategy is limited since it increases power consumption. Also, increasing the width of  $M_1$  increases the  $M_1$  gate capacitance  $C_{GS1}$ , and  $C_{in}$  primarily consists of  $C_D$  and  $C_{GS1}$ .

Ignoring frequency-dependent effects, the transimpedance gain of the common gate amplifier is approximately  $R_1$ . If the bias current is implemented with transistor  $M_2$  with transconductance  $g_{m2}$ , and we assume the output impedance of  $M_2$  is infinite for simplicity, then the input-referred noise is (Razavi, 2003, p.76):

$$\overline{i_{n,in}^2} = 4kT(\gamma g_{m2} + 1/R_1) \quad (2.10)$$

So, a large  $R_1$  results in high transimpedance gain and low noise. Compared to the single resistor topology, the common gate amplifier can achieve higher bandwidth and lower noise simultaneously. However, the noise current of  $M_2$  and  $R_1$  are referred to the input with a unity factor, which limits how low the noise can be. The noise of  $M_1$  doesn't appear in equation 2.10 since the output impedance of  $M_2$  is infinite, and so the noise current of  $M_1$  does not flow through  $R_1$ . Equation 2.10 is the noise

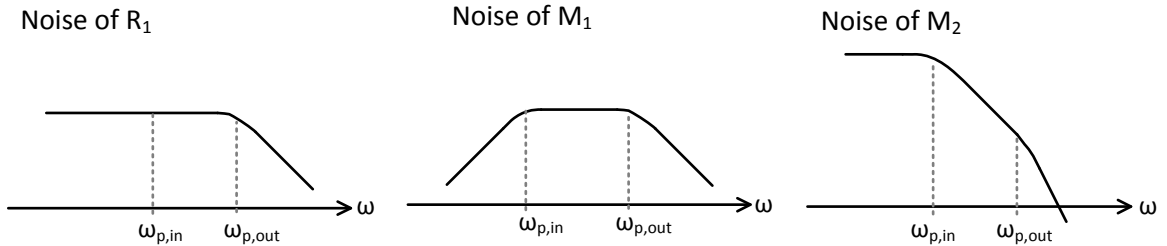


Figure 2.14: Sketch of the three main noise contributors in the common gate amplifier as a function of frequency. Each needs to be integrated over frequency to obtain the total integrated noise. From Razavi (2003, p.84).

power spectral density at the input, ignoring frequency-dependent effects. Although it provides some design insights, frequency-dependent effects need to be included to compute the total integrated noise. The noise power spectral density components for  $R_1$ ,  $M_1$ , and  $M_2$ , illustrated in Figure 2.14, need to be integrated over frequency. The noise power spectral density referred to the output is (Razavi, 2003, p.83):

$$\begin{aligned} \overline{v_{n,in,tot}^2} &= \frac{\overline{i_{n,R_1}^2} R_1^2}{\left[\left(\frac{\omega}{\omega_{p,out}}\right)^2 + 1\right]} + \frac{\overline{i_{n,M_1}^2} R_1^2 \frac{\omega}{\omega_{p,in}}}{\left[\left(\frac{\omega}{\omega_{p,in}}\right)^2 + 1\right] \left[\left(\frac{\omega}{\omega_{p,out}}\right)^2 + 1\right]} \\ &+ \frac{\overline{i_{n,M_2}^2} R_1^2}{\left[\left(\frac{\omega}{\omega_{p,in}}\right)^2 + 1\right] \left[\left(\frac{\omega}{\omega_{p,out}}\right)^2 + 1\right]} \end{aligned} \quad (2.11)$$

where  $\omega_{p,in} = \frac{g_{m1}}{C_D}$  and  $\omega_{p,out} = \frac{1}{R_1 C_{out}}$

After integrating Equation 2.11 over frequency, you obtain (Razavi, 2003, p.84),

$$\begin{aligned} \overline{i_{n,in,tot}^2} &= \left(\frac{4kT}{R_1}\right)(\omega_{p,out}/4) + (4kT\gamma g_{m1})(\omega_{p,out}/4) + (4kT\gamma g_{m2})(\omega_{p,in}/2) \end{aligned} \quad (2.12)$$

where  $\omega_{p,in} = \frac{g_{m1}}{C_D}$  and  $\omega_{p,out} = \frac{1}{R_1 C_{out}}$

The component for  $R_1$  makes sense because if we multiply by  $R_1^2$  to translate to integrated voltage noise at the output, we obtain  $\frac{kT}{C_{out}}$ , which matches the integrated output voltage noise of a standard low-pass RC circuit (Sarpeshkar et al., 1993). The  $R_1$  noise component in Equation 2.12 can be interpreted as the noise of  $R_1$  integrated over an equivalent bandwidth of  $\frac{\omega_{p,out}}{4}$ .

The noise from  $M_1$  is integrated from  $\omega_{p,in}$  to  $\omega_{p,out}$  since it has a zero and two poles, but if we assume  $\omega_{p,in} \ll \omega_{p,out}$ , then it is just like a low-pass circuit. So it can be interpreted as the noise of  $M_1$  integrated over an equivalent bandwidth of  $\frac{\omega_{p,out}}{4}$ .

The  $M_2$  noise component has two poles, at  $\omega_{p,in}$  and  $\omega_{p,out}$ , and it can be interpreted as the noise of  $M_2$  integrated over an equivalent bandwidth of  $\frac{\omega_{p,in}}{2}$ . Usually  $g_{m1} \gg 1/R_1$ , so the noise component from  $R_1$  can often be ignored.

The common gate amplifier also has challenging voltage headroom constraints, so it is difficult to design in deep sub-micron technologies such as 65nm which have

a 1V supply. From Equation 2.10, in order to minimize the input-referred noise,  $g_{m2} = \frac{2I_{D2}}{v_{GS2} - V_{TH2}}$  should be minimized, and so  $v_{DS2}$  should be maximized since it should be larger than  $(v_{GS2} - V_{TH2})$ . This requires voltage headroom. The input-referred noise can also be reduced by maximizing  $R_1$ , but this also requires voltage headroom.

### Shunt-Shunt Feedback TIA

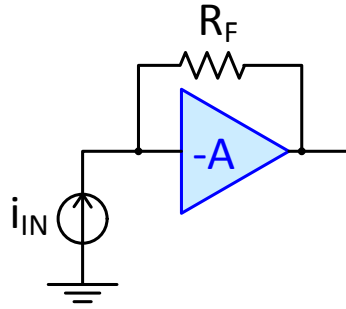


Figure 2.15: Shunt-shunt feedback transimpedance amplifier with feedback resistor  $R_F$  around voltage amplifier with gain  $-A$ .

The common gate amplifier is usually chosen when simplicity and low input impedance are the priority. On the other hand, the shunt-shunt feedback topology, shown in Figure 2.15, is usually selected when the designer wants a transimpedance amplifier with low input-referred noise. If the noise in the circuit is represented as shown in Figure 2.16, then the input referred noise current is (Razavi, 2003):

$$\overline{i_{n,in}^2} = \frac{4kT}{R_F} + \frac{\overline{v_{n,A}^2}}{R_F^2} \quad (2.13)$$

So, by choosing a large  $R_F$ , the input-referred noise can be minimized.

However, a large  $R_F$  is not good if low input impedance is also required. Assuming an ideal voltage amplifier with infinite input impedance and zero output impedance, the input impedance is of the circuit is:

$$Z_{in} = \frac{R_F}{1 + A} \quad (2.14)$$

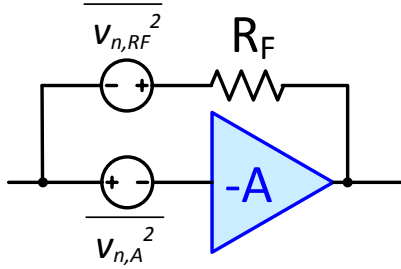


Figure 2.16: Shunt-shunt feedback transimpedance amplifier noise sources.

The  $(1 + A)$  factor helps decrease the input impedance, but a small  $R_F$  is still preferred if low input impedance has the highest priority.

The transimpedance gain is:

$$\begin{aligned}
 v_{out} &= -Av_{in} \\
 i_{in} &= (v_{in} - v_{out})/R_F = (v_{in} + Av_{in})/R_F \\
 Gain &= \frac{v_{out}}{i_{in}} = \frac{-A}{1 + A}R_F
 \end{aligned} \tag{2.15}$$

The voltage amplifier in the shunt-shunt feedback topology can be implemented with a common source amplifier to provide gain and a high input impedance, followed by a source follower to provide a low output impedance, as shown in Figure 2.17.

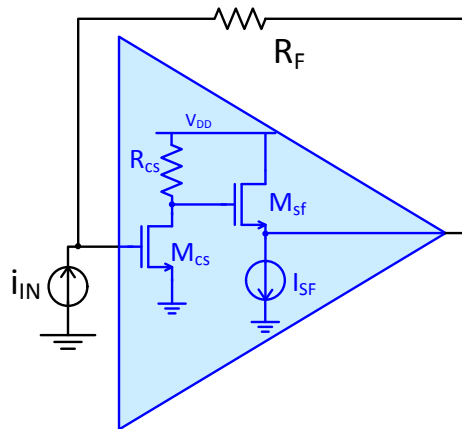


Figure 2.17: Shunt-shunt feedback transimpedance amplifier implementation. The voltage amplifier consists of a common source amplifier and a source follower.



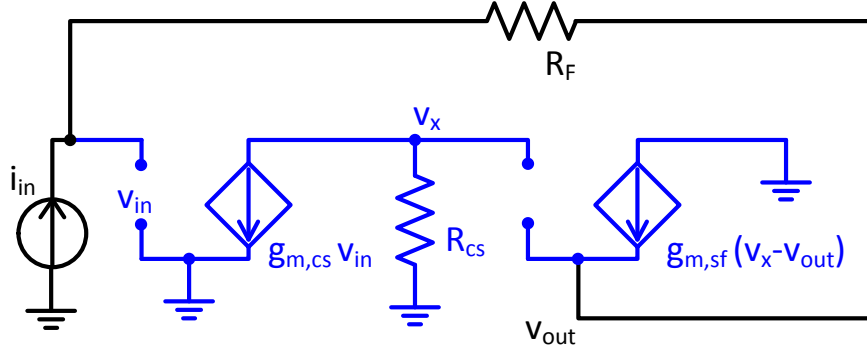


Figure 2.18: Shunt-shunt feedback transimpedance amplifier small signal diagram.

Even though the source follower has a low output impedance, it is not zero, as was assumed in the derivation of Equation 2.14 and 2.15. The small signal diagram in Figure 2.18 can be used to derive more accurate equations for the input impedance and gain.

$$i_{in} = -g_{m,sf}(v_x - v_{out}) \quad (2.16a)$$

$$v_x = -g_{m,cs}v_{in}R_{cs} \quad (2.16b)$$

$$v_{in} - v_{out} = R_F i_{in} \quad (2.16c)$$

Combining Equations 2.16a-c,

$$Z_{in} = \frac{v_{in}}{i_{in}} = \frac{(1/g_{m,sf}) + R_F}{1 + g_{m,cs}R_{cs}} \quad (2.17)$$

$$Gain = \frac{v_{out}}{i_{in}} = \frac{(1/g_{m,sf}) - g_{m,cs}R_{cs}R_F}{1 + g_{m,cs}R_{cs}} \quad (2.18)$$

These equations simplify to Equations 2.14 and 2.15, originally derived for an ideal voltage amplifier, if it is assumed that the output impedance of the amplifier

was zero, i.e.,  $g_{m,sf}R_F \gg 1$  and  $1/g_{m,sf} \approx 0$ :

$$Z_{in} = \frac{v_{in}}{i_{in}} = \frac{1 + g_{m,sf}R_F}{g_{m,sf}(1 + g_{m,cs}R_{cs})} \approx \frac{R_F}{1 + g_{m,cs}R_{cs}} \quad (2.19)$$

$$Gain = \frac{v_{out}}{i_{in}} = \frac{(1/g_{m,sf}) - g_{m,cs}R_{cs}R_F}{1 + g_{m,cs}R_{cs}} \approx \frac{-g_{m,cs}R_{cs}}{1 + g_{m,cs}R_{cs}}R_F \quad (2.20)$$

For applications where low input impedance is more important than low noise,  $R_F$  should be small. So what happens if  $R_F$  is zero ohms? If  $R_F$  is zero ohms and the additional small change of adding a resistor to the drain of  $M_{sf}$  and taking the output at the drain of  $M_{sf}$  is made, then the circuit transforms into a topology called the regulated cascode topology.

### Regulated Cascode TIA

The regulated cascode TIA (Park and Yoo, 2004; Nissinen and Kostamovaara, 2006; Sackinger, 2010) can be viewed as a shunt-shunt feedback TIA with  $R_F$  set to zero in order to reduce the input impedance. Alternatively, it can be interpreted as a common gate amplifier with a helper amplifier, as shown in Figure 2.19. This helper amplifier regulates the  $M_1$  gate voltage to help prevent the  $M_1$  source voltage from changing, reducing the input impedance. The helper amplifier can be implemented as a common source amplifier.

The input impedance is calculated as follows using the small signal diagram in Figure 2.20:

$$v_{out} = i_{in}R_1$$

$$\text{KCL: } v_{out}/R_1 + (v_{out} - v_{in})/r_{o1} = g_m(g_{m,cs}v_{in}(R_{cs}||r_{o,cs}) - v_{in}) = 0$$

$$Z_{in} = \frac{v_{in}}{i_{in}} = \frac{r_{o1} + R_1}{1 + g_{m1}r_{o1}(1 + g_{m,cs}(R_{cs}||r_{o,cs}))}$$

$$Z_{in} \approx \frac{r_{o1} + R_1}{g_{m1}r_{o1}(1 + g_{m,cs}(R_{cs}||r_{o,cs}))} \quad (2.21a)$$

$$\text{If } r_{o1} \gg R_1, \text{ then } Z_{in} \approx \frac{1}{g_{m1}(1 + g_{m,cs}R_{cs})} \quad (2.21b)$$

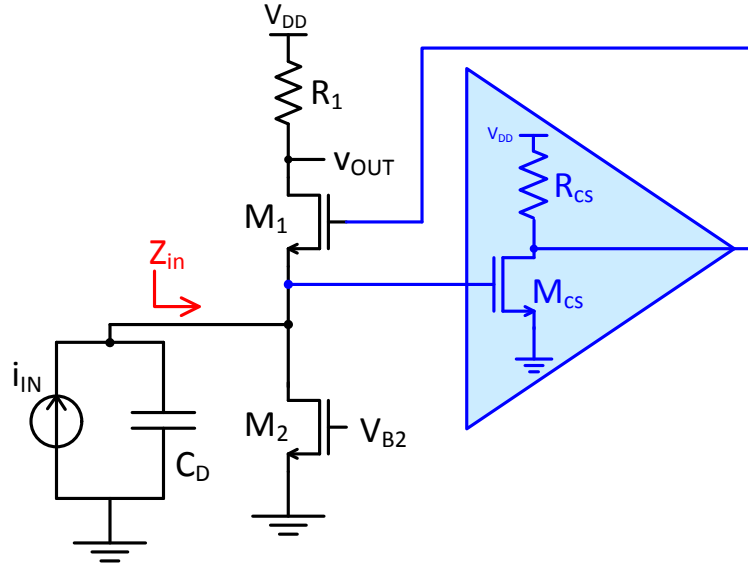


Figure 2.19: Regulated cascode transimpedance amplifier

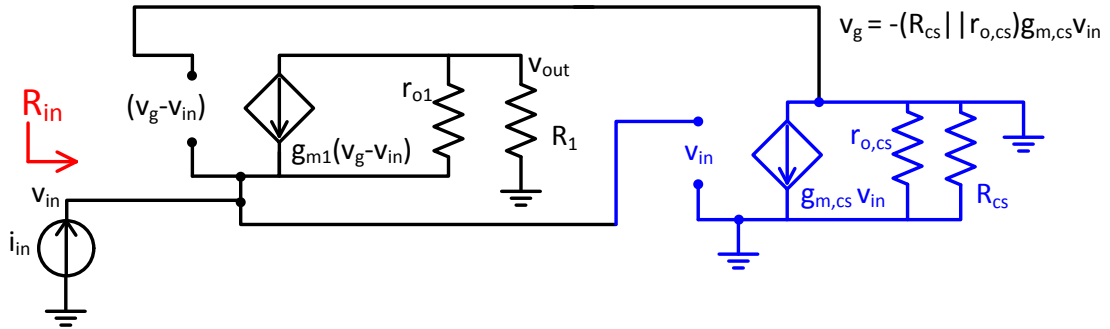


Figure 2.20: Small signal diagram of a regulated cascode transimpedance amplifier

Equation 2.21b matches Equation 2.14 for the shunt-shunt feedback TIA if  $R_F$  is replaced with the output impedance of the source follower, supporting the explanation that the shunt-shunt feedback TIA transforms into the regulated cascode TIA if there is no physical resistor  $R_F$ .

Since the circuit has a feedback loop, it is important to ensure the loop is stable and has enough phase margin. For a system with a dominant pole  $\omega_p$  and a non-dominant pole  $\omega_{p2}$ , unity gain frequency  $\omega_c$  and  $(\frac{\omega_c}{\omega_p}) \gg 1$ , the phase margin ( $PM$ ) is

(Razavi, 2003):

$$\begin{aligned}
PM &\equiv 180^\circ + \text{Phase}[T(j\omega)]|_{\omega=\omega_c} \\
&= 180^\circ - \tan^{-1}\left(\frac{\omega_c}{\omega_p}\right) - \tan^{-1}\left(\frac{\omega_c}{\omega_{p2}}\right) \\
&\approx 180^\circ - 90^\circ - \tan^{-1}\left(\frac{\omega_c}{\omega_{p2}}\right) \quad \text{since } \left(\frac{\omega_c}{\omega_p}\right) \gg 1 \\
PM &\approx \tan^{-1}\left(\frac{\omega_{p2}}{\omega_c}\right) \tag{2.22}
\end{aligned}$$

In the regulated cascode TIA, if  $T_o$  is the loop gain at DC, then  $\omega_c = \omega_p(1 + T_o)$  (Gray et al., 2001), and

$$\omega_p = \frac{g_{m1}}{C_D} \quad \text{since we want this pole to dominate} \tag{2.23a}$$

$$\omega_{p2} = \frac{1}{R_{cs}C_1} \tag{2.23b}$$

$$T_o = g_{m,cs}R_{cs} \tag{2.23c}$$

$$\begin{aligned}
\omega_c &= \omega_p(1 + T_o) \\
&= \frac{g_{m1}}{C_D}(1 + g_{m,cs}R_{cs}) \\
&\approx \frac{g_{m1}}{C_D}g_{m,cs}R_{cs} \tag{2.23d}
\end{aligned}$$

Substituting into the equation for phase margin results in an expression that can be used to design a regulated cascode TIA with a specified phase margin:

$$\begin{aligned}
PM &\approx \tan^{-1}\left(\frac{\omega_{p2}}{\omega_c}\right) \\
PM &\approx \tan^{-1}\left(\frac{\frac{1}{R_{cs}C_1}}{\frac{g_{m1}}{C_D}g_{m,cs}R_{cs}}\right) \\
\tan(PM) &\approx \frac{g_{m,cs}}{\frac{g_{m1}}{C_D}(g_{m,cs}R_{cs})^2C_1} \tag{2.23e}
\end{aligned}$$

### 2.3.3 Shaping

The shape of the signal pulse can be further manipulated using “shaper” blocks if amplifiers are not sufficient. Shapers are filters, comprised of either active components and/or passive components (e.g., simply CR or RC filters), which integrate (low pass) and/or differentiate (high pass) the pulse.

For energy discrimination, the goal is to maximize the signal-to-noise ratio, where the signal is defined as the measurement of the charge in the pulse. In general, this is achieved with a bandpass structure. The integration time constant is set to limit the noise while maintaining a sufficiently large signal and fast rise-time, whereas the differentiation time constant is set to limit the pulse width to prevent pile-up of pulses while maximizing SNR (Spieler, 2005).

For time discrimination, it is optimal to have the rise time of the amplifier match the rise time of the detector. If the amplifier was much slower, the output pulse would have a slower rising edge, increasing timing jitter. This is because voltage noise  $v_n$  is translated into timing jitter via the equation:

$$t_{jitter} = \frac{v_n}{dv/dt} \quad (2.24)$$

If the amplifier rise time was much faster than the detector signal rise time, the amplifier bandwidth would be higher than necessary, integrating more noise without being able to increase the output signal slope.

If a fixed threshold is used for timing discrimination, a slower rise time also results in more “time walk”, as will be explained in Section 2.3.4. If the time discrimination block input signal was much faster, the noise would increase without substantial increase in the output pulse rise time.

Another consideration for the shaper parameters is there may be the need to limit the pulse duration to prevent pile-up of successive pulses to accept a higher rate of incoming pulses.

### 2.3.4 Time discrimination

The analog approach to time discrimination requires an analog time discrimination circuit which triggers and produces a digital-like signal to indicate the pulse arrival time, and a time-to-digital converter which stores the value of a continuously running counter when it detects that the analog circuit has triggered.

#### Leading edge discrimination

The simplest analog time discrimination circuit uses a fixed threshold. For example, a comparator with a fixed threshold set near the base of the pulse triggers when the rising edge of the pulse crosses the threshold. The disadvantage of this method is that there may be “time walk”. If the signal amplitude changes, the rising edge slope of the signal may also change, resulting in an difference in the time at which the signal crosses the threshold, as shown in Figure 2.21. However, if the signal amplitude is also measured, time walk can be corrected in post-processing (Reynolds et al., 2010b). Also, if the signal rising edge slope is large, time walk will be small. Due to its simplicity, leading edge discriminators are often used despite the potential for time walk. The RENA-3 ASIC used in the breast-dedicated PET system described in this thesis uses this type of discriminator.

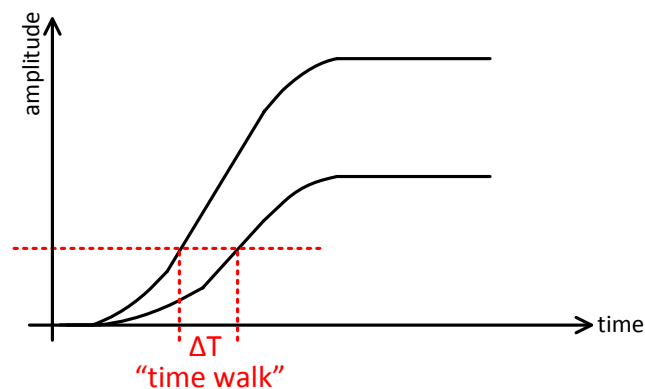


Figure 2.21: “Time walk” refers to the dependence of the threshold crossing time on signal amplitude and slope

### Constant fraction discrimination

A constant fraction discriminator (CFD) is a timing discriminator that compensates for time walk by triggering at a constant fraction of the pulse amplitude (Ortec, 2012). Figure 2.22 shows the operation of a CFD. The input signal is delayed and a constant fraction  $f$  of the input signal is subtracted from it. This produces a bipolar pulse. The zero crossing of the bipolar pulse is the time at which the CFD triggers. However, this zero crossing comparator may be easily triggered by noise, so the top branch acts as an arming discriminator, with threshold  $V_{TH}$  set above the noise floor. When the delay is set to be larger than the pulse rise time, the CFD is triggered on a constant fraction of the pulse amplitude, which is equivalent to a constant fraction of its rise time. The CFD is good for scintillator-photodetector detectors in PET which produce pulses with a wide range of amplitudes but a narrow range of rise times and pulse widths. The drawback of the CFD is its added complexity over the leading edge discriminator. The CFD can be implemented using analog circuits, or the waveform can be digitized and the CFD (or another timing algorithm) can be implemented digitally in a Field Programmable Gate Array (FPGA) or in software.

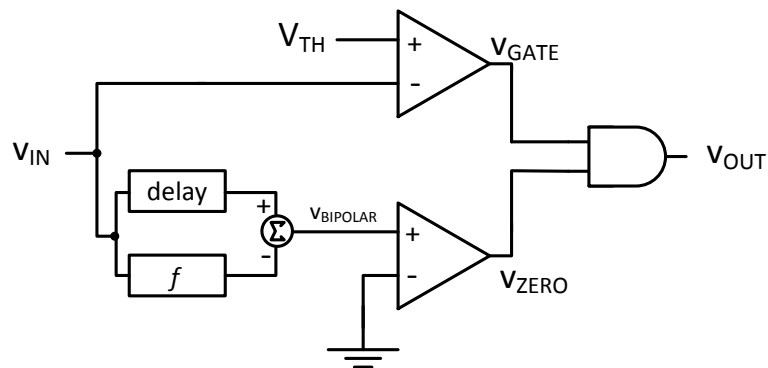


Figure 2.22: Functional diagram of a constant fraction discriminator (CFD)

### 2.3.5 Waveform digitization

Instead of using analog circuits to determine the energy and arrival time of the pulse using charge-sensitive amplifiers and analog time discriminator circuits, the pulse

waveform can be sampled and digitized using a free-running ADC. An algorithm implemented in software or on an FPGA can then compute the integral and arrival time of the pulse (Guerra et al., 2008; Peng et al., 2007; Mann et al., 2006; Fontaine et al., 2006).

The advantages of free-running ADCs include flexibility, robustness, pile-up detection, and superior time resolution. This method is flexible since it can be adapted for various detectors that require different shaping parameters by modifying the algorithms in software and the easily customizable digital hardware in FPGAs. It uses a minimal number of analog blocks and relies on digital techniques which are generally more robust in the presence of noise and process/temperature variations. The algorithms can detect if pulse pile-up has occurred and reject or correct it (Wang et al., 2012). It is possible to obtain superior time resolution using a free-running ADC and software algorithms instead of analog techniques (Peng et al., 2007).

The disadvantage of the free-running ADCs is higher power and cost. The general rule of thumb is that at least four samples are required in the pulse rising area (Cho et al., 2011). Time-of-flight PET applications use fast detectors, such as LSO or LYSO coupled to fast PMTs, which produce pulses with a rise time of about 2.2ns. For this case, a sampling rate of 1.3GSps is required to achieve time resolutions of 200-300 ps FWHM (Cho et al., 2011). This sampling rate corresponds to about four samples on the rising edge. Even in non-time-of-flight PET applications, a sampling rate of at least 100MSps is required to achieve at least 1.7 ns FWHM time resolution. For the digitized pulse waveform to be used for energy determination as well, we found through simulation that about 8 bits are required. It is not trivial to design power-efficient ADCs with these specifications. A state-of-the-art ADC with above 1 GSps sampling rate has a power consumption ranging from 2mW (for 5-6 bits) to a few hundred mWs (for 10 bits). A state-of-the-art ADC with about 100 MHz sampling rate has a power consumption ranging from a 0.1mW (for 7 bits) to tens of mW (for 10 bits) (Murmans, 2012). Due to the high power consumption and cost of free-running ADCs, many PET systems use analog circuits instead of waveform digitization.

With this understanding of PET front-end electronics and detectors, we proposed



to build PET system that pushes the boundaries of PET contrast and spatial resolution. We decided to use detectors comprised of LYSO scintillation crystals and PSAPDs, to use analog circuits for charge integration and time discrimination, and to target breast cancer as an application.

## 2.4 Breast cancer and PET

Improving the spatial and contrast resolution of PET may have great contributions to breast cancer. Currently, there are difficulties associated with the detection, diagnosis and staging of breast cancer. Mammography is accepted as the best means to screen for non-palpable breast cancer, but the sensitivity of mammography is only 68-85% for women with radio-dense breasts, and 54% for women below 40, although it improves to 82-98% for other cases (Rosenberg et al., 1998; Kerlikowske et al., 1996). 30% of screened cases are inconclusive due to radio-dense or distorted breast tissue. The non-specific nature of the structural signatures (micro-calcifications and masses) for breast cancer determined by mammography results in a poor positive predictive value of only 15-30% (from studies in the United States) (Kopans, 1992), resulting in many unnecessary biopsies. Although biopsy is a safe procedure, it increases patient anxiety, costs \$1000-3000 per procedure, and may result in scarring that could cause difficulties in the interpretation of future mammograms. Staging breast cancer through axillary dissection causes significant trauma and often yields negative results. Finally, there is no practical imaging technique to guide or monitor therapy and treatments.

PET has the potential to be a specific, sensitive, and non-invasive breast cancer identification technique that could fill the gaps in standard methods. Many studies have reported that PET has higher sensitivity and higher specificity than other imaging modalities in breast cancer imaging. However, PET has not been incorporated into standard practice for breast cancer. Most PET systems currently in the clinic are whole body imaging systems and not appropriate for breast imaging due to low photon sensitivity geometry, inadequate spatial and contrast resolutions for detecting small lesions, relatively high cost, and long scan times. As a result, PET's role in breast cancer management is currently limited to only the evaluation and re-staging

of recurrent breast cancer and distant metastasis.

In order for PETs role in other phases of breast cancer management to increase, its spatial and contrast resolution needs to improve (Rosen et al., 2007). Tumor size less than 1 cm and low tumor grade is a significant predictor of a false-negative 18F-FDG PET results using whole body PET scanners (Kumar et al., 2006), which typically have an inadequate spatial resolution of  $> 7 \times 7 \times 7 \text{mm}^3$  and a poor photon sensitivity of only 1%. A number of breast-dedicated PET designs are under development and evaluation at a number of research groups and companies, where the PET detectors are placed close to the breast to improve photon sensitivity (MacDonald et al., 2009; Abreu et al., 2006; Raylman et al., 2008; Wu et al., 2009; Wang et al., 2006; Weinberg et al., 2005; Doshi et al., 2001; Furuta et al., 2009; Freifelder and Karp, 1997).

The next chapter describes an overview of a breast-dedicated PET system we are building at Stanford. In contrast to the breast-dedicated designs under development elsewhere, this work aims to further push the spatial resolution down to  $1 \text{mm}^3$ , and places the PET detectors close to the breast to facilitate a high photon sensitivity of 8-14% (Zhang et al., 2007b). This system is intended to act as an adjunct to mammography, by helping to resolve inconclusive mammograms, screening high risk patients, visualizing early stage primary breast cancer, guiding needle biopsy, monitoring therapy, and staging axillary metastasis.

## Chapter 3

# Breast-Dedicated PET System Electronics

Our breast-dedicated PET system consists of two imaging panels, each with a 16cm x 9cm x 2cm detector head (see Figure 3.1). The panels are comprised of 4608 Position Sensitive Avalanche Photodiodes (PSAPDs) attached to an 18,432 channel data acquisition system. In contrast to clinical systems that typically only detect about 1% of the photon coincidences, simulations showed that this two panel geometry captures 8 to 14% of the photons for a panel separation of 4-8cm (350-650 keV energy window; 6 ns time window) (Zhang et al., 2007b).

The system is designed to be modular, with 9 “cartridges” stacked to form a panel.

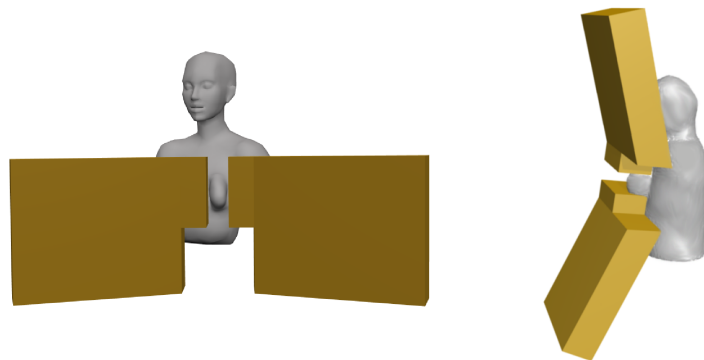


Figure 3.1: Imaging panels in two potential breast imaging orientations

Table 3.1: Electronics modules in cartridge

Module	Quantity	Description
HV Bias Board	1	Supplies high voltage to detectors in one cartridge
RENA Board	4	Data acquisition electronics board, housing 8 RENA-3 ASICs and 4 FPGAs
Discrete Board	8	Board with signal conditioning, detector biasing, thermistor readout, and leakage current monitoring circuitry
Pitch Adapter	8	Flexible circuit that separates high voltage from low voltage detector signal routing
Flat Flexible Cable	8x8=64	Flat Flexible Cables route signals from the Pitch Adapters to the Discrete Boards
Fin of detectors	8	Aluminum fin heatsink holds 16 Dual LYSO-PSAPD modules placed side-by-side
Dual LYSO-PSAPD module	8x16=128	Detector module, consisting of two 8x8 LYSO scintillation crystal arrays and two PSAPDs
LYSO scintillation crystal array	8x16x2=256	LYSO scintillation crystal array, consisting of 64 1x1x1mm <sup>3</sup> crystals in an 8x8 grid
PSAPD	8x16x2=256	Position Sensitive Avalanche Photodiode

This thesis focuses on the design of two of these cartridges, which will be replicated to construct the full system in the future. Figure 3.2 and Figure 3.3 show the major electronics components in one cartridge: 1) high resolution detectors, 2) interconnect between the detectors and the electronics, 3) high voltage distribution, 4) RENA-3 data acquisition board, and 5) “Discrete Board”. This chapter will describe these electronics components. Table 3.1 lists the electronics and detector modules in one cartridge, and the quantity of each module in one cartridge.

The development of this system was a large project that required the collaborative effort of many individuals. My role was to design high voltage distribution for the detectors, investigate multiplexing and signal conditioning to allow the detectors to be read out by the electronics with the best performance possible, design a compact and cost-efficient method to connect the detectors to the electronics, integrate the system components together to build two cartridges of the system, and characterize the performance. This thesis focuses on these contributions.



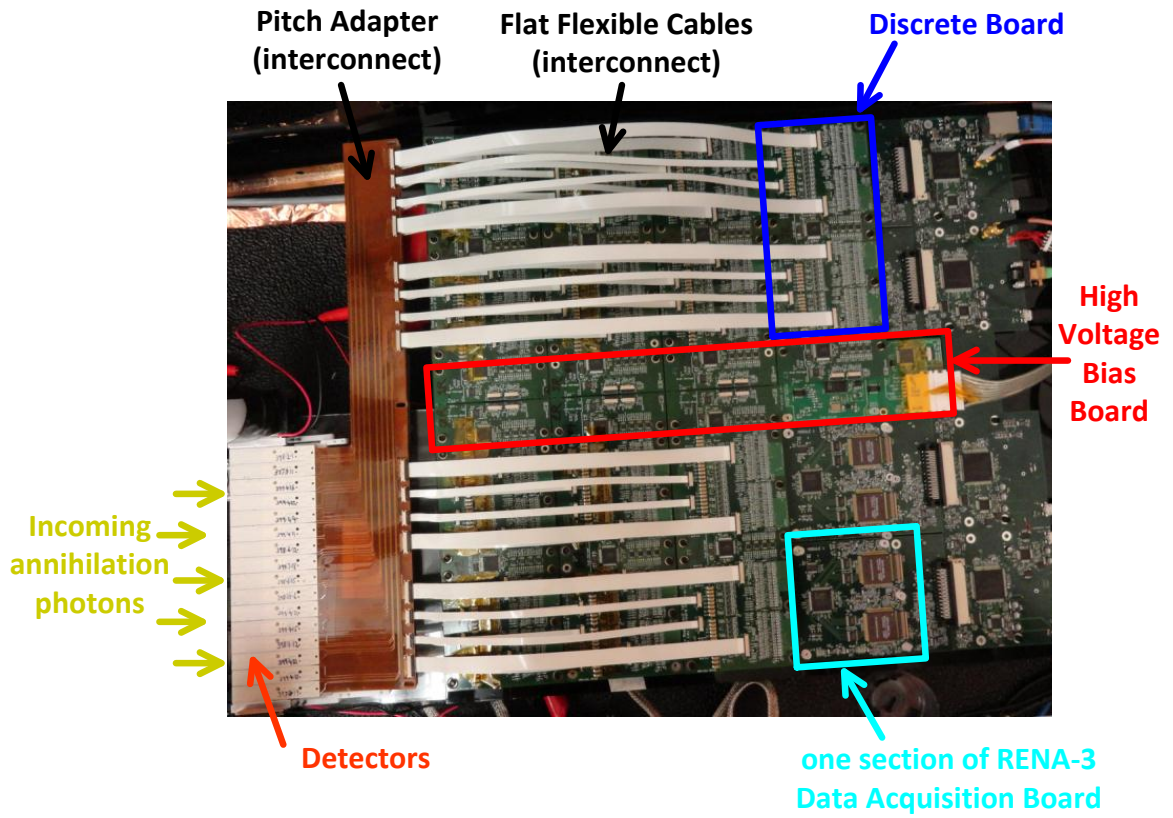


Figure 3.3: Picture of one cartridge, with electronics components discussed in this thesis labeled.

### 3.1 High resolution detector

The detector is comprised of stacked layers of 8x8 arrays of  $1 \times 1 \times 1 \text{mm}^3$  LYSO (lutetium yttrium oxyorthosilicate) scintillation crystals coupled to thin PSAPDs. A Dual-LYSO-PSAPD module, shown in Figure 3.4, consists of two LYSO arrays, each coupled to a PSAPD mounted on a flexible circuit. An alumina frame in the detector module provides mechanical support. The PSAPDs used are those described in Section 2.2.2, manufactured by Radiation Monitoring Devices (RMD), Inc. (Watertown, MA), except they are mounted on flexible circuits instead of ceramic. The PSAPD has a sensitive area of  $8 \times 8 \text{mm}^2$  and a gain of about 1000 when biased with 1750V. The  $1 \times 1 \times 1 \text{mm}^3$  crystals are separated by a 3M VM2000 reflector.

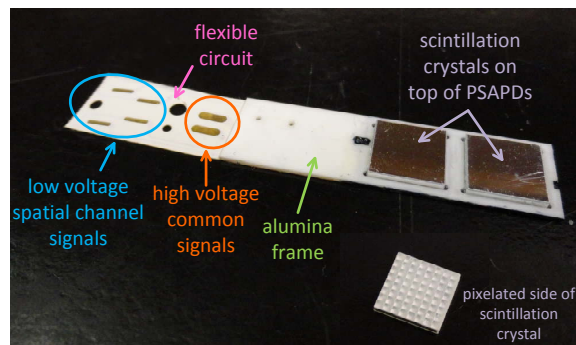


Figure 3.4: A Dual-LYSO-PSAPD module. Two PSAPDs are mounted on a flexible circuit. An LYSO scintillation crystal array is mounted on each PSAPD, with the pixelated side coupled to the PSAPD. An alumina frame provides mechanical support.

The flexible circuit is made out of Liquid Crystal Polymer (LCP) (Espanex L Series from Nippon Steel Chemical Company) instead of typical flexible circuit materials such as Polyimide or Kapton. The water vapor transmission rate (WVTR) is  $0.13 \text{ [g-20um/(m}^2\text{/day)]}$  for LCP, compared to  $105 \text{ [g-20um/(m}^2\text{/day)]}$  for Polyimide. Low moisture permeability was critical because moisture could provide a conductive path from the high voltage (about 1750V) traces to the low voltage traces (Units for WVTR is grams per meter squared per day, for a 20um thick film, measured at  $40^\circ\text{C}$  at 90% relative humidity). The flexible circuit was designed so that the distance between the high voltage traces and exposed contacts far exceeded the dielectric breakdown

distance for 2000V. There are two common terminal contacts on the flexible circuit, one for each PSAPD. There are only four spatial channel contacts since the spatial channels for the two PSAPD are multiplexed. This will be described in more detail in the next chapter.

Compared to the majority of existing PET systems, this design uses a unique “edge-on” configuration for the detectors (Levin, 2002; Vandembroucke et al., 2010). As shown in Figure 3.5, the Dual-LYSO-PSAPD modules are stacked and high energy photons hit the modules “edge-on”. This provides “depth of interaction” (DOI) positioning (DOI explained in 2.1.2), enabling 1mm resolution in all three dimensions. In the final system, the detector modules will be irradiated in this “edge-on” config-

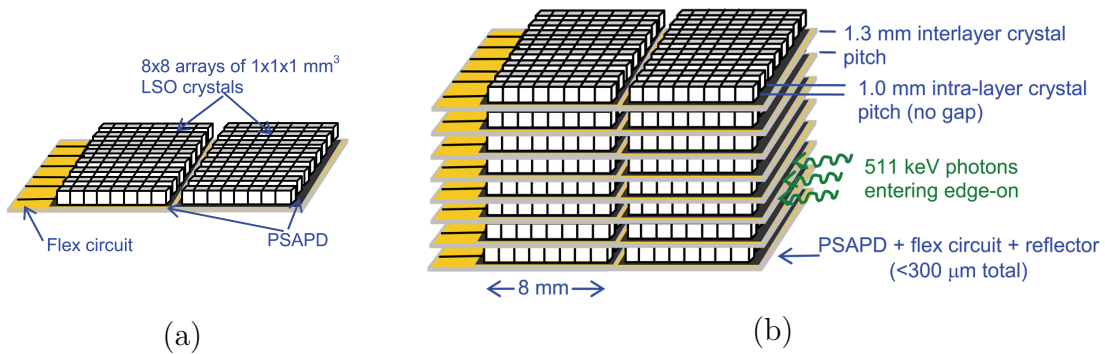


Figure 3.5: Stacking of Dual-LYSO-PSAPD modules (a) Depiction of one Dual-LYSO-PSAPD module, which consists of two scintillation crystal arrays and two PSAPDs configured two units deep with respect to incoming 511 keV photons, mounted directly on a flex circuit. (b) A stack of Dual-LYSO-PSAPD modules with 511 keV photons entering edge-on. The design enabled 1 mm<sup>3</sup> intrinsic resolution, directly measured 1 mm DOI resolution, the capability to position the 3D interaction coordinates of multiple interaction photon events, and >90% scintillation light collection efficiency, independent of interaction location.

uration. However, it is useful to irradiate the detector in a “face-on” configuration, as shown in Figure 3.6, when producing flood histograms. In a face-on configuration, the number of counts in each crystal in the array is more evenly distributed than in the edge-on configuration so it is easier to evaluate the detector’s crystal identification ability. Also, a larger number of total counts are obtained in a shorter amount



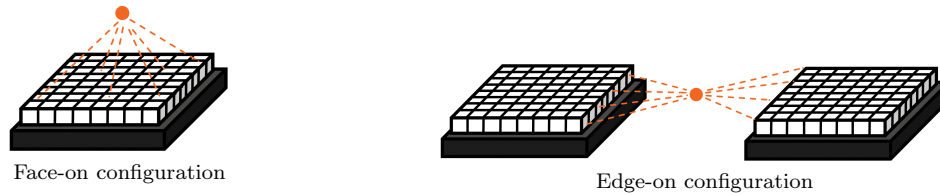


Figure 3.6: Face-on versus edge-on configurations. In the face-on configuration, the Na-22 point source was placed above the detector. In the edge-on configuration, the Na-22 source irradiated the edge of the detector.

of time. Some characterization results presented in this thesis will be specified that they were acquired in this “face-on” configuration.

Each cartridge of the camera has 128 Dual-LYSO-PSAPD modules, arranged with 16 placed side-by-side and 8 in a stack. To aid modularity, facilitate assembly, and enable thermal regulation, 16 Dual-LYSO-PSAPD modules are first placed side-by-side and attached to an aluminium fin using miniature screws (Figure 3.7) (Spanoudaki et al., 2008). There is a gap between the aluminum fin and the PSAPDs to prevent high voltage arcing. An alumina piece with windows for the scintillation crystal arrays provides mechanical support for the region near the PSAPDs and scintillation crystal arrays, and is held in place by the notches in the aluminum fin. A fin of detectors was treated as one unit — as will be described in the following sections, one Pitch Adapter, one Discrete Board, and two quarter-sections of a RENA-3 Board are used to readout one fin.

8 fins are stacked to assemble each cartridge, with a pitch of 56.5 mils (1.435 mm). The aluminum fin is slid into an aluminum sidewall to form the stack. This sidewall is attached to a heatsink. In the final system, the temperature of this heatsink will be controlled by a water cooling system. Currently, air from fans attached to plastic pipes blows air on the heatsink to draw heat away. The plastic pipes were necessary to keep the motor in the fan further away from the detectors and electronics to reduce electromagnetic interference.

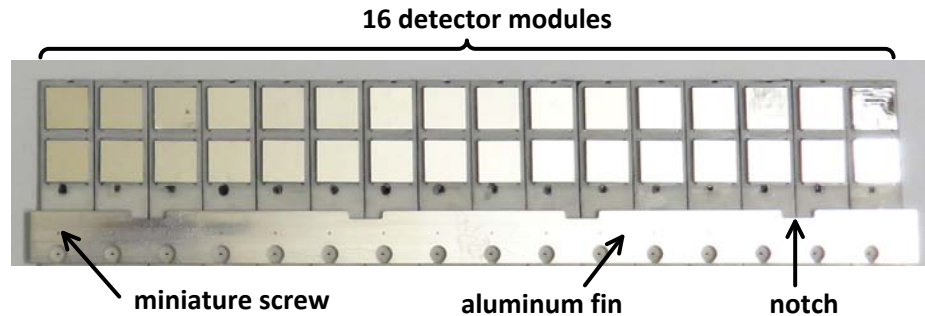


Figure 3.7: A fin of detectors consists of 16 Dual-LYSO-PSAPD modules placed side-by-side, attached to an aluminum fin

## 3.2 Interconnect

The contacts on the Dual-LYSO-PSAPD modules need to be attached to the readout electronics PCBs in the most space-efficient and economical manner possible. To achieve this, a two step approach is used: first the contacts are epoxied to a “Pitch Adapter” which fans out and changes the pitch of the contacts on the detector modules to match the electronics and separates high voltage from low voltage signals. Then, flat flexible cables (FFCs) and flat flexible cable connectors (FFC connectors) are used to connect to the electronics.

The Pitch Adapter also groups the high voltage signals from four detector modules together so that one 8-position, 0.5mm pitch FFC connector (Molex 54548-0870-c) can connect to the 8 high voltage terminals from 4 detector modules. Similarly, it groups the low voltage signals from four detectors together so that one 18-position, 0.5mm pitch FFC connector (Molex 54548-1870-c) can connect to the 16 low voltage terminals from 4 detector modules. The flexible circuit is made with a 2 mil thick Polyimide base, which has a dielectric strength of 3 kV/mil or more, so it is fine to have low voltage and high voltage traces cross on different layers.

There are two Pitch Adapter designs, “even” and “odd”, as shown in Figure 3.8. The Pitch Adapters are stacked with a pitch of 56.5 mils (1.435mm). There are cut-outs so that when the Pitch Adapters are stacked, the FFC connectors have twice the pitch of the fins (56.5 mils x 2, or 1.435 mm x 2), which gives more room for the

FFC connectors which are 1.2mm tall.

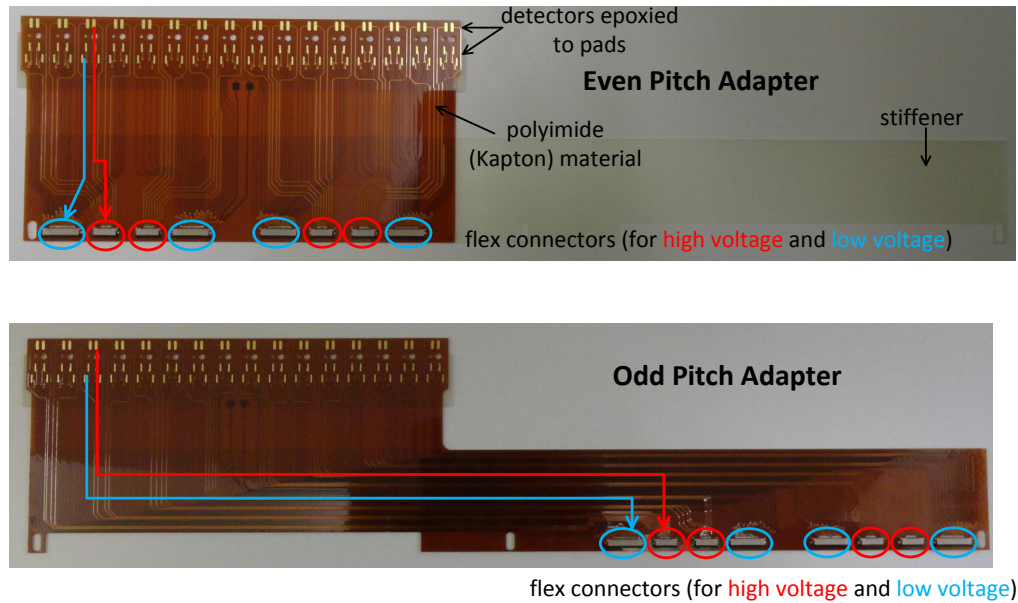


Figure 3.8: Pitch Adapter “even” and “odd” designs. The high and low voltage signals from the PSAPDs are routed to separate FFC connectors. The high voltage FFC connectors are indicated by a red circle. The low voltage FFC connectors are indicated by a blue circle. For example, the signal routing path for the 3rd module is shown by the arrows (red for high voltage; blue for low voltage).

The contacts on the Dual-LYSO-PSAPD modules were attached to the Pitch Adapter with conductive silver epoxy, as shown in Figure 3.9. Silver epoxy was preferred over solder since we wanted to avoid exposing the detectors to the high temperatures ( $>220$  degrees Celsius) required for solder, and because it made it possible to have all the contacts encapsulated by flexible circuit material, which was especially important for the high voltage contacts. Conductive silver epoxy only needs to be baked at  $85^{\circ}\text{C}$  for curing.

The FFC connectors were attached to the Discrete Board using flat flexible cables (FFCs). The advantage of this design is that it costs much less to purchase FFCs with custom lengths versus designing flexible circuits with custom lengths. For mechanical support, stiffener was attached to the portion of the Pitch Adapter where the contacts to the detectors are located, as well as the portion of the Pitch Adapter where the FFC

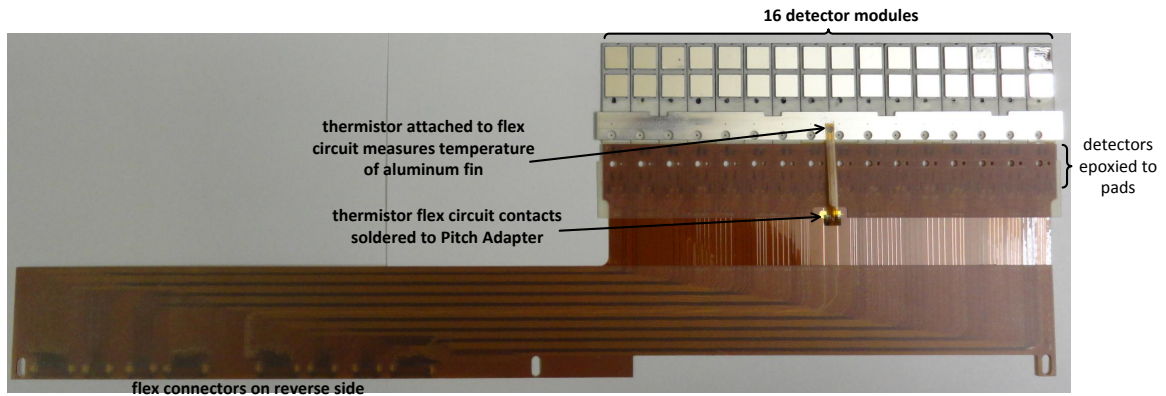


Figure 3.9: Fin epoxied to an “odd” Pitch Adapter. There is a thermistor which measures the temperature of the aluminum fin to estimate the temperature of the detectors. This is explained in Section 3.5.

connectors are placed. So, only the center portion of the Pitch Adapter is flexible. This flexible portion enables the system electronics to be tilted 20 degrees away from the detectors, as shown in Figures 3.1 and 3.2, to facilitate the imaging of patients.

### 3.3 Programmable high voltage distribution

The performance of the system is highly dependent on the PSAPD bias voltage. The bias voltage dictates the PSAPD gain, which in turn determines the fraction of the dynamic range of the electronics that is used and whether the electronics are saturated. Also, each PSAPD has an optimal bias voltage which, when coupled to the readout electronics, gives the best energy resolution, flood histogram, and time resolution. Temperature and process variations affect this optimal bias voltage (Vandenbroucke et al., 2012). In this system with 2304 detector modules, it is inevitable that the detector modules do not all have same optimal bias voltage. Plus, even though the system has temperature regulation, our simulations showed that there could be up to a 4°C gradient across the detectors in a fin (Lau et al., 2008). Being able to adjust the bias voltage of each detector module individually enables us to compensate for temperature and process variations.

The nominal PSAPD bias voltage is -1750V, and most commercially available high voltage (at least 2000V) power supplies only have 8-16 output channels per unit. Purchasing hundreds of these units requires a prohibitively large amount of money and space. Fortunately, only an adjustment of 100V around the nominal voltage of -1750V is really necessary to compensate for process and temperature variations (i.e., from -1700V to -1800V). It is not necessary to adjust from 0V to -1800V. Vandenbroucke et al. (2012) showed that the optimal bias voltage (as indicated by the coincidence time resolution) for temperatures ranging from 5°C to 40°C was in the range of 1700V to 1770V.

By taking advantage of the fact that only an adjustment of 100V was necessary, we were able to design a programmable high voltage (HV) distribution system by taking a high density multi-channel DAC with an output range of at least 100V and floating the entire DAC so that the DAC's reference is at -1800V (Lau et al., 2012d). This produced outputs ranging from -1700V to -1800V relative to earth ground. Figure 3.10 shows a block diagram of this idea.

The Analog Devices AD5535 14-bit DAC chip was used. This chip can actually be configured to have a 200V output range, but in this case the output range was set to 100V to reduce heat generation since 100V was sufficient. The AD5535 provides 32 outputs in a compact BGA package of only 15 mm x 15 mm. The AD5535 needs to be powered by three supply voltages: +5V, -5V, and +125V. Cosel SUCS1R5 DC-DC converters produced the +5V and -5V and the Ultravolt AA series DC-DC converter produced the +125V. These DC-DC converters were also floating with their reference at -1800V, and were powered by +12V. This +12V was produced by an isolated DC-DC converter (Cincon EC3A) which can withstand 3000V between its inputs and outputs. It took an input of +24V relative to earth ground, and output +12V relative to the floating ground (-1800V). The -1800V floating ground was established using a high voltage power supply.

Communication with the AD5535 DAC was done with signals from USB transmitted through the OPI1268S opto-isolator, and sent to the ATmega16a microcontroller which was also floating with its reference at -1800V. The microcontroller implemented the AD5535 DAC communication protocol to set its individual output voltages.

Figures 3.11 and 3.12 are pictures of the PCBs that implement this idea. The DC-DC converters are all housed on a PCB (called the High Voltage (HV) Floating Power Supply) in a crate, away from the detectors and rest of the PET system data acquisition electronics, to prevent electromagnetic noise from contaminating the sensitive detectors and electronics. RC filters were placed at all the DC-DC converter outputs to reduce noise. This includes filters with capacitors between the output and the floating reference as well as filters with capacitors to earth ground. A custom-made, shielded high voltage cable brings the supply voltages and references to the High Voltage (HV) Bias Board which houses the microcontroller and four AD5535 DACs. So,  $32 \times 4 = 128$  programmable high voltage outputs (ranging from  $-1700\text{V}$  to  $-1800\text{V}$  relative to earth ground) are produced from one HV Bias Board, enough for one cartridge. There is a  $1\text{M}\Omega$  resistor in series with each DAC output for current limiting and filtering.  $1\text{M}\Omega$  was chosen since it resulted in an acceptable  $1\text{V}$  drop (since the current drawn is about  $1\mu\text{A}$  per channel) and provided sufficient current limiting and filtering. We measured  $20\text{mV}_{\text{pp}}$  of bias ripple, which is small since the average bias voltage is about  $-1750\text{V}$ .

The power consumption of each AD5535 DAC is over  $300\text{mW}$  and the chips are in a tightly confined space, so a method to cool the chips was necessary. 370HR was chosen for the PCB material. It has a thermal conductivity of  $0.4\text{W}/\text{mK}$  (slightly better than FR4 which is  $0.36\text{W}/\text{mK}$ ). A 20-28 mil thick copper heat sink was attached to the back side of the board with Ventec V-4A2, a thermally conductive dielectric material, sandwiched in between the board and the heat sink. Ventec V-4A2 has a thermal conductivity of  $2.2\text{W}/\text{mK}$ . The heat sink draws the heat to the back end of the system where the cooling pipes are.

An alternative solution that does not require floating the entire DAC at  $-1800\text{V}$  is to have the common terminal of the PSAPD fixed at  $-1800\text{V}$  and to allow the anode to range from  $0\text{V}$  to  $+100\text{V}$  using the DAC. Then, the DAC's reference would be at  $0\text{V}$ , but then all the bias resistors, signal conditioning circuits, and leakage current monitoring circuitry on the Discrete Board would need to be referenced to the DAC output instead of  $0\text{V}$ . Despite the engineering challenge of floating the entire DAC at  $-1800\text{V}$ , we decided that it would be preferable to do that so that everything else

could have a 0V reference.

Each detector module was individually tested before it was bonded to the Pitch Adapter and placed in the system. The testing procedure involved taking energy resolution and flood histogram measurements at the bias voltage that RMD tested the module at, as well as 10V above and below that voltage. This testing was performed at 27°C. The bias voltage that produced the best flood histogram figure of merit and energy resolution was recorded as the optimal bias voltage for that detector module. In the system, the AD5535 DAC was programmed to bias each detector module at this optimal bias voltage.

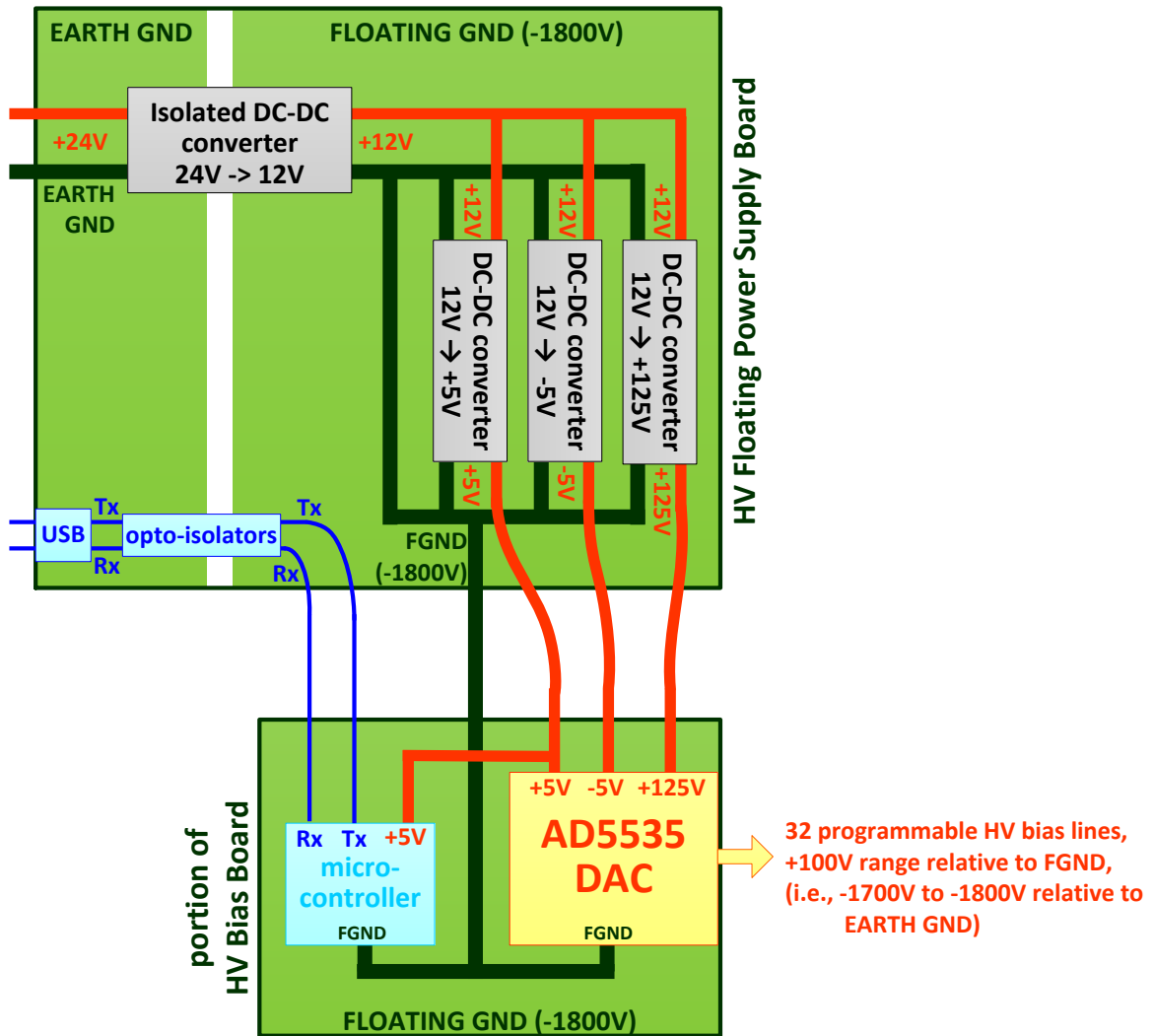


Figure 3.10: Programmable high voltage block diagram. The AD5535 DAC floating with its reference at -1800V produces 32 channels of programmable high voltage. The AD5535 is powered by DC-DC converters which produce +5V, -5V, and +125V relative to -1800V.



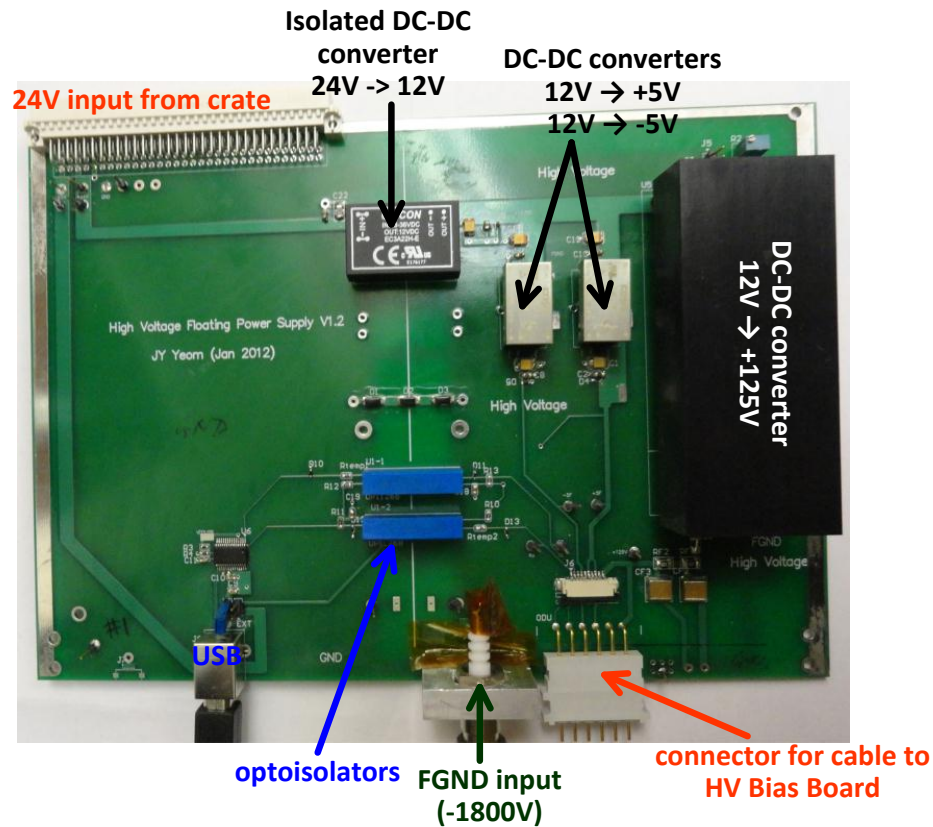


Figure 3.11: Picture of High Voltage (HV) Floating Power Supply Board, with DC-DC converters to produce +5V, -5V, and +125V relative to the floating ground of -1800V.

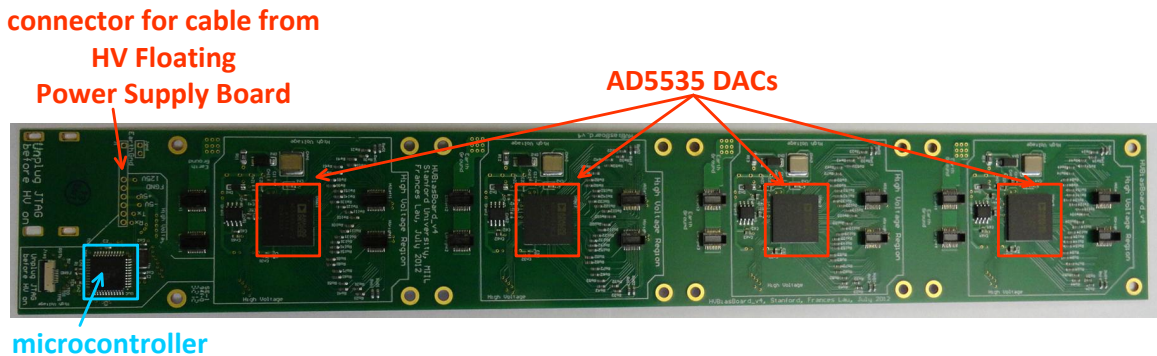


Figure 3.12: Picture of High Voltage (HV) Bias Board, with four DACs, providing 128 outputs of programmable high voltage

### 3.4 RENA-3 ASIC and Board

The front-end electronics in the data acquisition primarily use analog circuits for charge integration and time discrimination, rather than taking the waveform digitization approach. These analog circuits are inside the RENA-3, a 36 channel ASIC developed by NOVA R&D (Riverside, CA) (Tumer et al., 2006, 2008). Each channel consists of a charge sensitive preamplifier, a shaper, and a sample-hold circuit which computes the integral of the pulse. Each channel can also be configured to generate a time stamp for pulses detected using a leading edge discriminator. The RENA-3 has a self-triggering sparse readout mode for reading out only the channels that triggered or only user-selected channels. When a pulse is detected, data from the sample-hold circuits of the channels of interest are stored and output sequentially on a differential analog bus. Figure 3.13 shows a board that houses eight RENA-3 ASICs and their supporting circuitry, and allows 32 detector modules to be readout (Reynolds et al., 2010a). There are four of these boards in one cartridge.

The two user-selectable full-scale input dynamic ranges are 9fC and 54fC (NOVA R&D, 2007). With the 54fC setting, we found experimentally that the amplifier begins to be non-linear beyond 54fC, although the saturation only becomes severe above about 130fC. The estimated charge output from a PSAPD coupled to LYSO is roughly 1pC (see Section 2.2.2), exceeding the maximum dynamic range of the RENA-3 preamplifier. Actually, the discrepancy is not as large as these numbers indicate. The effective input capacitance of the charge sensitive preamplifier inside the RENA-3 is only 30pF, even smaller than the PSAPD capacitance of 45-50pF. So, only 40% of the 1pC generated arrives at the RENA-3 input, and the remainder stays inside the detector capacitance. It is usually not desired to have the preamplifier effective input capacitance lower than the detector capacitance, but in this particular situation it was acceptable since we needed to attenuate the signal. There was also attenuation due to the parasitic capacitance of the interconnect between the detectors and electronics (e.g., from FFCs that are up to 30 cm long). Even with these two factors decreasing the signal, the charge was still about 2-4 times too large for the dynamic range of the RENA-3, depending on if the channel is a spatial channel or

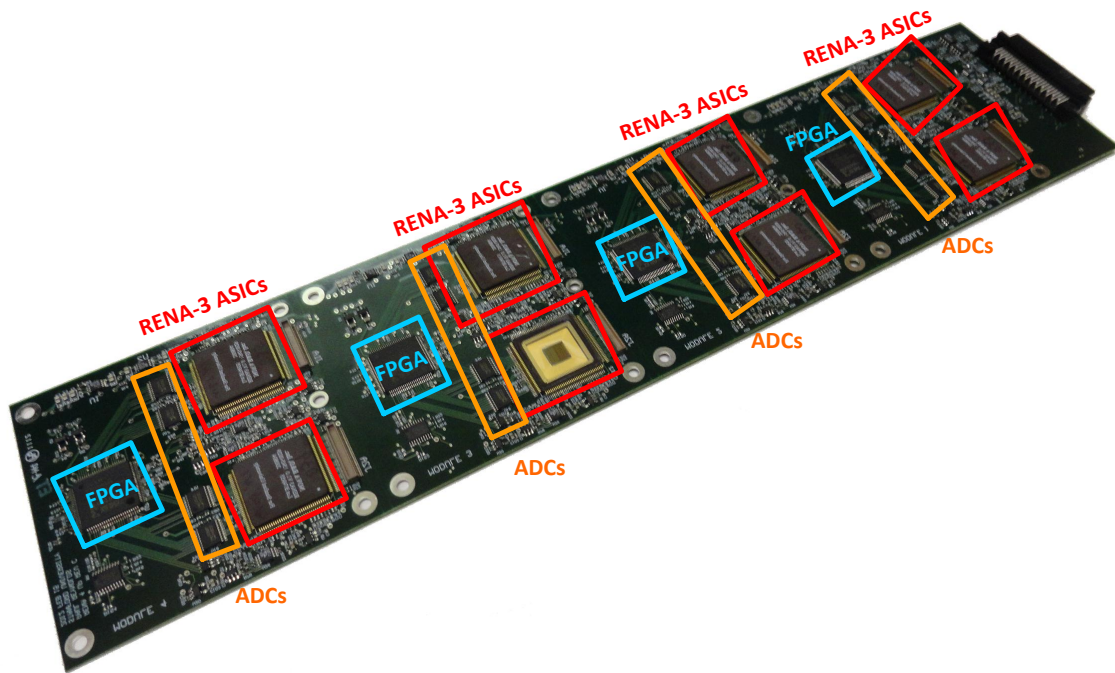


Figure 3.13: Photograph of RENA Board, with RENA-3 ASICs, ADCs, and FPGAs labeled. In this picture, the chip package cover for one of the RENA-3 ASICs was removed so that the silicon die can be seen.

a common. So, additional attenuation was achieved using signal conditioning and charge division circuits on the Discrete Board (see Section 3.5).

The RENA-3 ASIC's differential analog output was digitized by a 3MSamp/s ADC, and the digitized data was processed by an FPGA. The FPGA also controlled the RENA-3 configuration logic. A prototype USB 2.0 backend electronics interface was used to acquire the data for this thesis. This backend will be replaced by Ethernet in the final system. With the prototype interface, the data was transferred from each FPGA at a rate of 12Mbaud to the FT232H USB UART integrated circuit, which output the data to the computer via USB 2.0. The hardware coincidence gating window allowed events within  $1\mu\text{s}$  of each other to be output to the software. The data acquisition software had a finer coincidence gating window, based on the measured time resolution of the system, to remove singles.

The prototype interface between the RENA Board FPGA and the FT232H USB UART integrated circuit, combined with the existing data acquisition software, was limited to processing only about 25,000 events/sec, although software buffering prevented packets from being dropped to a certain degree. This count rate was insufficient for the activity rate we would ideally like to have when acquiring phantom images. Work is ongoing to increase the bandwidth between the FPGA on the RENA Board and the backend electronics, use two Gigabit ethernet ports to interface with the computer, narrow the hardware coincidence gating window, and improve the data acquisition software.

### 3.5 Discrete Board

The original role of the “Discrete Board” was to house discrete passive components (capacitors and resistors) for AC coupling and detector biasing, hence the name “Discrete Board”. However, it evolved to include other circuitry (both discrete components and small integrated circuit chips) for signal conditioning, temperature monitoring, and leakage current monitoring. Figure 3.14 is a picture of the final Discrete Board which has circuitry for 16 detector modules (one fin).

The Discrete Board has two Atmel ATmega16a microcontrollers which implement the communication protocols of the programmable capacitor and enables the readout of the thermistor temperature and leakage current. The USART (Universal Synchronous and Asynchronous serial Receiver and Transmitter) inside the microcontroller is used to communicate with the computer. To enable all 16 Discrete Board microcontrollers in one cartridge to communicate to the computer via one interface in the back-end, the microcontroller USART transmit and receive lines are connected to LVDS (low voltage differential signaling) chips, and daisy chained together.

The Discrete Board also reads out the temperature of the detectors. A thermistor is attached to each fin to indirectly sense the temperature of the detectors, as shown in Figure 3.9. This thermistor is connected to the Discrete Board via the Pitch Adapter and FFCs. The Maxim IC MAX6691 thermistor temperature-to-pulse-width converter chip on the Discrete Board converts the thermistor measurement into a

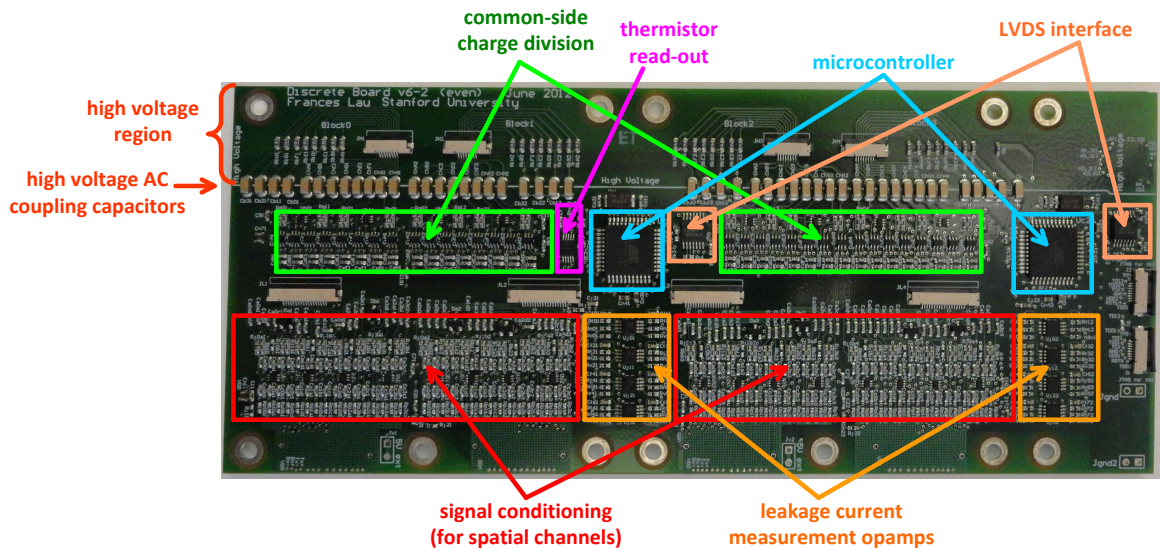


Figure 3.14: Photograph of Discrete Board

pulse-width-modulated signal, which is interpreted by the microcontroller. This temperature information is used in a control loop to adjust the voltage of Peltier coolers used to keep the temperature of the detectors constant. This is important since the gain of PSAPDs depends exponentially on temperature (Vandenbroucke et al., 2012).

Figure 3.15 shows an overview of some of the remaining circuits on the Discrete Board. The PSAPDs are biased via  $10\text{M}\Omega$  resistors on the HV side and  $1\text{M}\Omega$  resistors on the LV side, which also act as current limiting and filtering resistors. High voltage rated capacitors ( $2000\text{V}$ ) AC couple the signals from the PSAPD to remove the high voltage bias. The board is designed so that the high voltage section is in the top half.

After the AC coupling, the signals undergo signal conditioning or charge division using discrete resistors and capacitors. I investigated methods to scale the dynamic range of the spatial channel signals as well as the common signals to fit within the RENA-3 ASIC dynamic range, with the least amount of signal-to-noise-ratio (SNR) degradation possible. The method for scaling the dynamic range of the spatial channel signals is explained in the next chapter in Section 4.3. The method for scaling the dynamic range of the common signals is described in the next section.

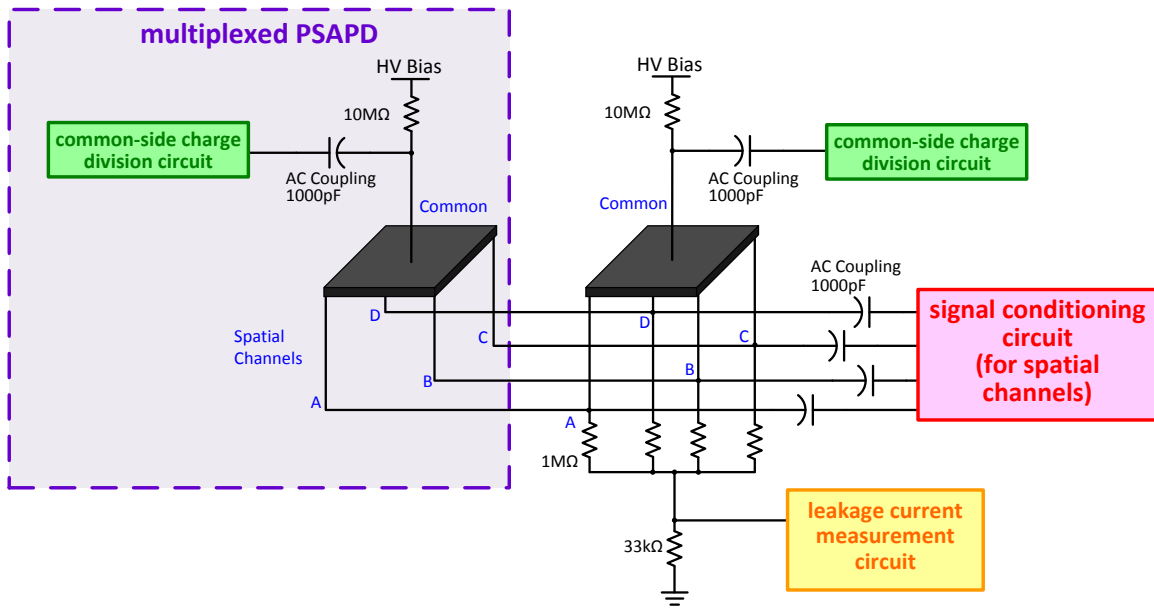


Figure 3.15: An overview of most of the circuits on the Discrete Board. The following sections will describe each aspect in more detail: Section 3.5.2 will describe the leakage current measurement, Section 3.5.1 will describe the common-side charge division, Section 4.2 will describe the multiplexing of PSAPDs, and Section 4.3 will describe the signal conditioning circuit for spatial channels. As will be described in Section 4.2, in this system, two PSAPDs are multiplexed together, so the items inside the purple dotted line are added.

### 3.5.1 Common-side charge division

To scale the dynamic range of the common signal, the signal was split into two RENA-3 channels using a capacitive divider (see Figure 3.16), choosing a division ratio so that one is a low gain common used for measuring the energy of the signal pulse, and the other is a saturated high gain common used for measuring the time of the pulse. To allow for variations in PSAPD gain, the MAX1474 programmable capacitor was used, providing 32 programmable capacitance values ranging from 6.4pF to 13.3pF, with the default set to 9.7pF. The capacitance values used in the final version of the Discrete Board are shown in Figure 3.16, and has a nominal charge division ratio of 2.7:1, which was sufficient considering charge was already lost due to the low effective input capacitance of the RENA-3 and the parasitic capacitance of the interconnect.



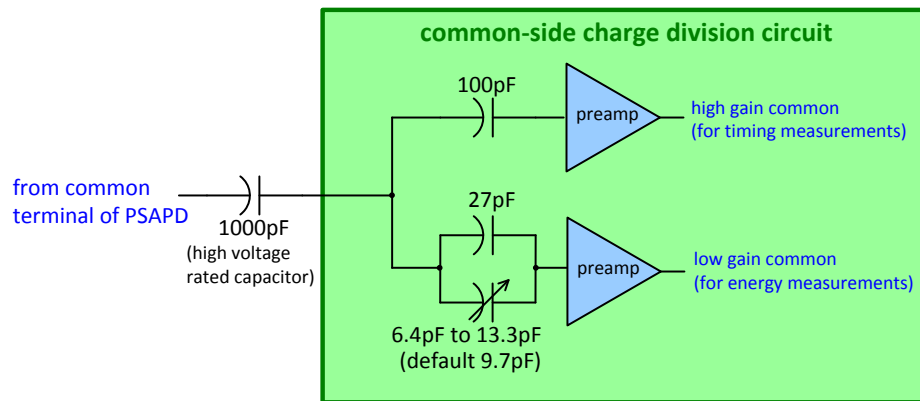


Figure 3.16: Charge division circuit for the common signal. The low gain common has a programmable capacitor with values ranging from 6.4pF to 13.3pF in 0.22pF increments.

Splitting the charge has the advantage of utilizing some of the excess charge instead of simply shunting all the excess charge to ground using a capacitor. The charge in the high gain common saturates the preamplifier into a slew rate limiting operating mode. In this mode, the time walk caused by the leading edge discriminator is decreased (although not eliminated). Also, by triggering on both commons, each with a different threshold, two independent measurements of the time of the pulse can be used to improve time resolution (Reynolds et al., 2010b). Another advantage of using two RENA-3 channels instead of using a capacitor to shunt the charge to ground is that the capacitance at the input of either preamplifier, and hence the input referred preamplifier noise, is almost the same as in a design without this dynamic range scaling.

### 3.5.2 PSAPD leakage current monitoring

The leakage current (dark current) of the PSAPD is a very important parameter to monitor since it indirectly indicates the PSAPD bias voltage, gain, and temperature. It can also show if the PSAPD is disconnected or if it has failed. Therefore, it is essential to monitor the leakage current of each of the 2304 detector modules individually rather than just having one measurement for the sum of the leakage currents from all the modules.

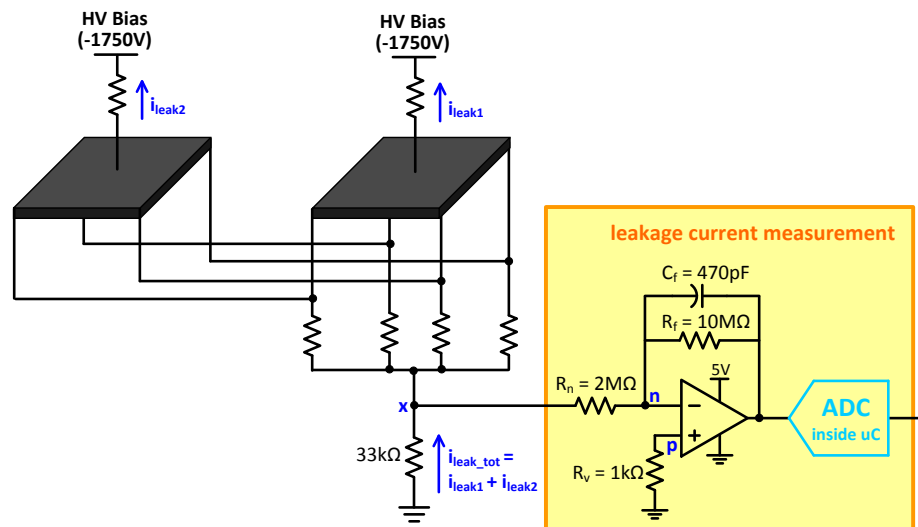


Figure 3.17: Leakage current measurement circuit. The opamp amplifies the voltage across the  $33\text{k}\Omega$  resistor to measure  $i_{\text{leak\_tot}}$ .

The leakage current from one module is about 1-2 $\mu\text{A}$ . This current passes through a  $33\text{k}\Omega$  resistor and the voltage across this resistor is digitized. Figure 3.5.2 shows a schematic of the leakage current monitoring circuit. The circuit is at the spatial channels side of the PSAPD, where there are four spatial channel terminals, so the terminals first need to be tied together before the  $33\text{k}\Omega$  resistor. An opamp is used to buffer the voltage and to minimize the fraction of the small 1 $\mu\text{A}$  leakage current that is diverted away from  $33\text{k}\Omega$  resistor. The voltage produced across the resistor (node x) is actually a negative voltage because the bias voltage is -1750V, not +1750V. In order to amplify this negative voltage, a negative supply voltage is normally needed for the opamp. This is problematic since a noisy switching regulator would be needed to convert the positive 5V supply voltage available into a negative supply voltage. Fortunately, this problem was overcome by using a AD822 opamp which has an input voltage range which extends 0.2 V below its negative rail. Therefore, it could be used with +5V for its positive rail and ground as its negative rail, and its input range would then extend down to -0.2V. This opamp is configured in an inverting amplifier configuration, so that the output is a positive voltage.

The gain of the opamp was chosen to be 5, created using  $R_f=10\text{M}\Omega$  and a



$R_n=2M\Omega$ . The AD822 also has a very low input bias current of 2pA and a very high input impedance of  $10^{13}\Omega$  due to its n-channel JFET input stage, so a negligible amount of leakage current is diverted into the opamp. Some leakage current is diverted into  $R_n$ , but only about 1.6% since  $2M\Omega$  is much larger than  $33k\Omega$ . Although a resistor value larger than  $33k\Omega$  could have been used without resulting in a voltage below  $-0.2V$ ,  $33k\Omega$  was chosen because it minimizes the amount of current diverted away. Also, the linearity of the opamp degrades when the input voltage is close to  $-0.2V$  and we wanted to be able to handle the case when the leakage current increases up to  $5\mu A$  during PSAPD failure. In order to keep the percentage of current diverted into the  $R_n$  at 1.6%, the gain of the opamp is limited to 5 since it was difficult to find a resistor in the 0402 package that is larger than  $10M\Omega$ . The amplified voltage is digitized by the 10-bit successive approximation ADC inside the ATmega16a microcontroller. The  $1k\Omega$  current limiting resistor  $R_v$  was added as recommended by the AD822 datasheet to prevent damage to the opamp if an input voltage greater than the opamp positive rail is accidentally applied, forward biasing the n-channel JFET device junction. Since the current flowing into the opamp terminals is almost zero, node p is essentially at zero volts. However, the voltage at node n is a very small negative voltage, not exactly zero volts, since the opamp does not have infinite gain. Therefore, it is important to use the AD822 opamp since it could handle voltages as low as  $0.2V$  at its input even if its negative rail is at ground.

An alternative solution is to measure the leakage current at the common terminal. In this case, the voltage measured would be positive so the opamp would not need to be able to accept input voltages below its negative rail. However, then the leakage current measurement circuit would need to be floating with its reference at high voltage so this solution was not chosen.

## 3.6 Summary of components studied

This chapter described the detector, interconnect, high voltage distribution, RENA-3 board, and Discrete Board in the system. I integrated the components for which I was responsible with the software and hardware components my colleagues designed

to build two cartridges of the system. Results from these two cartridges are presented in Chapter 5.

During the design process, I did in-depth investigations on detector multiplexing and signal conditioning for scaling the dynamic range of the spatial channels signals. I also modeled the detectors and electronics to understand the behavior of the detector when coupled to the preamplifier in the RENA-3 ASIC. This is described in the next chapter.

# Chapter 4

## Detector interface circuit design

This chapter describes in-depth investigations done during the process of designing the Discrete Board, which houses circuits that interface with the detectors. Section 4.2 presents a method used to multiplex the detectors and Section 4.3 describes the signal conditioning circuits on the Discrete Board. To help analyze these two design issues, I first developed a model and simulation framework for the PSAPD and the associated electronics.

### 4.1 PSAPD and electronics modeling and simulation

The goal of the simulation was to produce a simulated flood histogram that models experimental results and to predict how adding circuit components or multiplexing PSAPDs would affect the quality of the flood histogram and the signal-to-noise ratio (SNR). So, it was important to model the light photon distribution on the surface of the PSAPD, the PSAPD capacitance and resistive sheet, the RENA-3 preamplifier, and any added signal conditioning circuit components. It was also critical to model noise contributors from the scintillator, PSAPD, and electronics.

The detector and circuits, including their noise components, were modeled using a combination of H-SPICE, Verilog-A, and Matlab. Three main noise sources were

modeled: i) the LYSO scintillation crystal, ii) the PSAPD, and iii) the electronics.

To model noise, the noise components were categorized into three types: a) independent noise, b) distributed noise, and c) proportional noise. Independent noise (represented by the random variable  $A_{noise}$ ) is noise that is independent between spatial channels. Distributed noise (represented by the random variable  $\delta_A$ ) is noise that is distributed across the detector. Proportional noise ( $kA_{light}$ ) is proportional to the signal and correlated between the spatial channels. Table 4.1 summarizes how noise from the three noise sources can be categorized into these three types of noise. Each type of noise is treated differently in the simulation flow, as shown in Figure 4.1.

Table 4.1: Categorization of noise sources

Noise Source	Type of Noise		
	Independent Noise ( $A_{noise}$ )	Distributed Noise ( $\delta_A$ )	Proportional Noise ( $kA_{light}$ )
Scintillation Crystal	<ul style="list-style-type: none"> <li>• none</li> </ul>	<ul style="list-style-type: none"> <li>• none</li> </ul>	<ul style="list-style-type: none"> <li>• Poisson variance in number of light photons produced from each interaction               <ul style="list-style-type: none"> <li>– modeled in Matlab</li> </ul> </li> <li>• secondary scintillator effects               <ul style="list-style-type: none"> <li>– modeled in Matlab</li> </ul> </li> </ul>
PSAPD	<ul style="list-style-type: none"> <li>• none</li> </ul>	<ul style="list-style-type: none"> <li>• leakage current shot noise               <ul style="list-style-type: none"> <li>– modeled in FEM (Verilog-A)</li> </ul> </li> <li>• thermal noise from resistive sheet               <ul style="list-style-type: none"> <li>– modeled in FEM (H-SPICE)</li> </ul> </li> </ul>	<ul style="list-style-type: none"> <li>• shot noise due to light signal               <ul style="list-style-type: none"> <li>– modeled in Matlab</li> </ul> </li> <li>• Poisson variance in PSAPD gain               <ul style="list-style-type: none"> <li>– modeled in Matlab</li> </ul> </li> <li>• Excess noise factor               <ul style="list-style-type: none"> <li>– modeled in Matlab</li> </ul> </li> </ul>
Electronics	<ul style="list-style-type: none"> <li>• RENA-3 ASIC thermal noise               <ul style="list-style-type: none"> <li>– modeled in Matlab</li> </ul> </li> </ul>	<ul style="list-style-type: none"> <li>• none</li> </ul>	<ul style="list-style-type: none"> <li>• none</li> </ul>

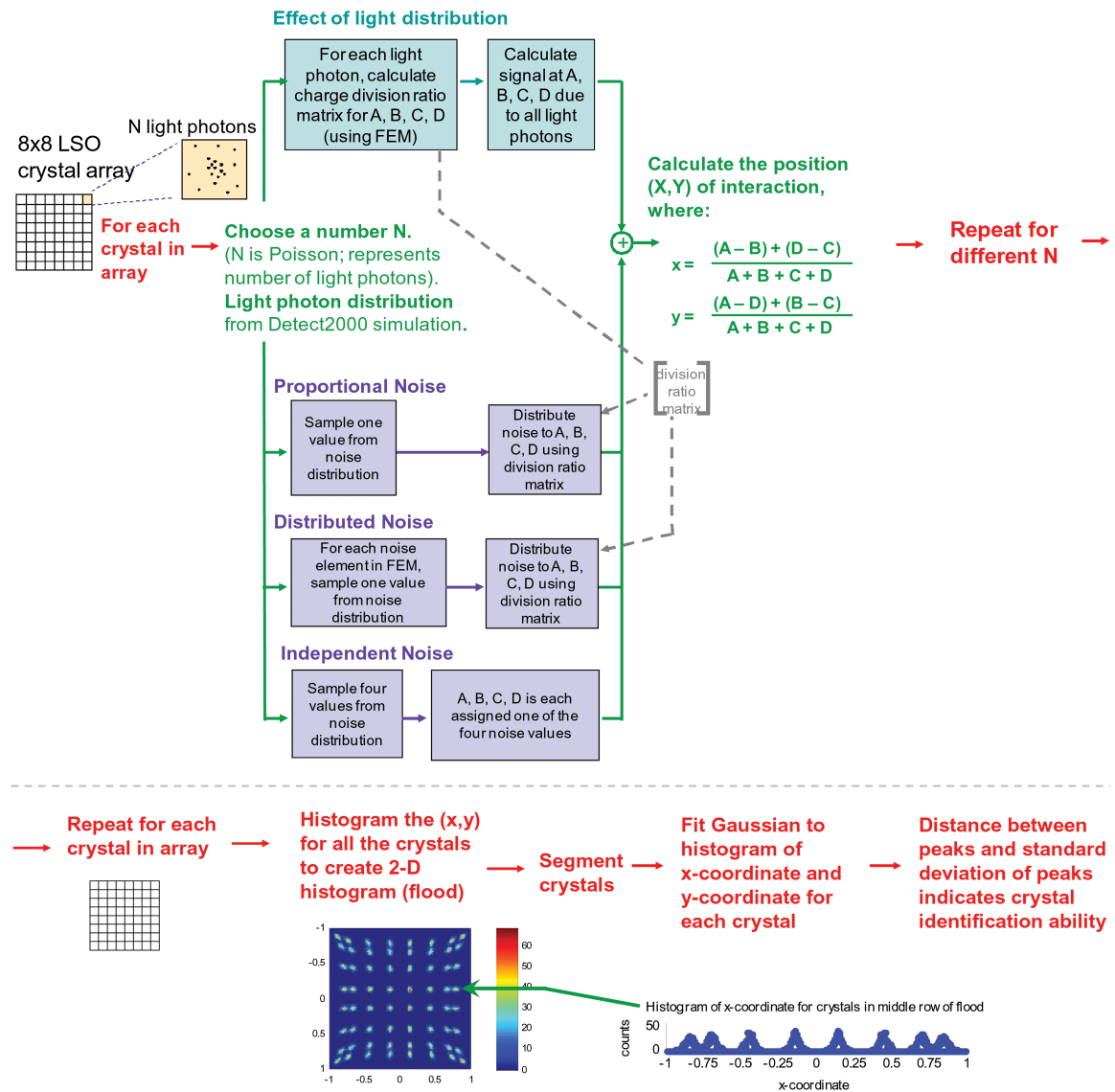


Figure 4.1: Simulation flow chart for creating a simulated flood histogram, used to evaluate the crystal identification ability. An example simulated crystal flood histogram is shown at the bottom along with a profile through one crystal row.

### 4.1.1 LYSO scintillation crystal array modeling

The first step towards creating a simulated flood histogram was to model the scintillation crystal. With a face-on configuration for the detector, the number of 511keV

photons interacting in each pixel of the scintillation crystal array is on average equal. Therefore, to produce a flood histogram, we assumed one 511keV photon interacts in each crystal and produces  $N$  light photons. For each crystal in the array, a Poisson distributed number  $N$ , with mean  $N_{avg}$ , was chosen in Matlab to represent the number of light photons created by a 511keV photon interacting in that crystal. This is shown in the simulation flow in Figure 4.1. The noise from LYSO is proportional to the signal since the variance of a Poisson random variable is equal to its mean. The mean of  $N$  was computed by assuming 25 visible light photons are produced in LYSO per keV (Knoll, 2000) and the efficiency of visible light photons hitting the PSAPD was 0.9.

In addition to the Poisson variance, we added an additional variance in Matlab to account for secondary effects such as scintillator transfer efficiency, non-proportionality, and inhomogeneities. These effects were lumped together because they are difficult to model and study (Wernick and Aarsvold, 2004; Moses et al., 2008). The standard deviation of this additional variance was chosen so that the sum of all the noise sources added together in quadrature matches the energy resolution of 14.5% FWHM measured by Lau et al. (2010). Fortunately, the contribution of this type of noise to the flood histogram simulation is minor.

These light photons have a certain spatial distribution. Detect2000 (Cayouette et al., 2003) was used to simulate the spatial distribution of the light photons produced by that crystal.  $N$  light photons were randomly chosen from this spatial distribution to be the light photons that hit the PSAPD.

### 4.1.2 PSAPD and electronics modeling

The PSAPD produces charge at each point where a light photons hits. To understand how this charge is divided by the PSAPD resistive sheet to produce signals at the four corners, a Finite Element Model (FEM) was created for the PSAPD. The FEM was constructed in H-SPICE, with 10x10 subunits. Figure 4.2 illustrates one subunit of the FEM. The total device capacitance was assumed to be 45pF (Dokhale et al., 2004). So, each subunit consisted of a 0.45pF capacitor in parallel with a noise current

source. The subunits were connected together with a high resistivity resistor grid representing the resistive sheet on the n-doped side for the spatial channels and a low resistivity grid for the common channel. Resistor elements of  $5.2\text{k}\Omega$  and  $250\Omega$  were used to model the sheet resistance at operating bias for the high and low resistivity layers respectively (Farrell, 2009).

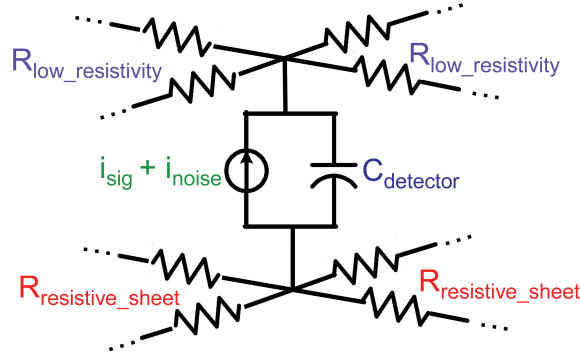


Figure 4.2: One subunit of the FEM circuit model for PSAPD.  $C_{\text{detector}}$  is the PSAPD capacitance,  $i_{\text{sig}}$  is the photodetection signal, and  $i_{\text{noise}}$  is the combination of all the noise sources.  $R_{\text{resistive sheet}}$  models the high resistivity layer on the n-doped side of the PSAPD that is connected to the spatial channels.  $R_{\text{low resistivity}}$  models the low resistivity layer that is connected to the common. This FEM section is replicated 100 times.

Injection of charge into the FEM was simulated at the points where the light photons hit and the signal at the four corners,  $A_{\text{light}}$ ,  $B_{\text{light}}$ ,  $C_{\text{light}}$ , and  $D_{\text{light}}$ , was estimated. It is computationally intensive to repeat this FEM simulation for each light photon. To avoid this, a charge division ratio matrix was created by injecting charge in each node of the FEM and recording the magnitude of the signal at the four corners,  $A_{\text{light}}$ ,  $B_{\text{light}}$ ,  $C_{\text{light}}$ , and  $D_{\text{light}}$ . Then, in the simulation of the flood histogram, this charge division matrix was interpolated to determine the magnitude of the signal at the four corners for each light photon that hit the PSAPD at a certain location. A current pulse was simulated at each of the four corners and the amplitude was scaled by the charge division ratio matrix. The current pulse was assumed to have  $0.5\text{ns}$  rise time and  $46\text{ns}$  decay time (Moszynski et al., 1996; Shao, 2007),

Noise was also incorporated into the FEM and in the calculation of the magnitude of the total charge created when a light photon hit. The PSAPD has five noise sources:

shot noise due to the leakage current, thermal noise in the resistive sheet, Poisson variance in the PSAPD gain, an excess noise factor, and shot noise due to the light signal.

The shot noise due to leakage current (measured to be roughly  $1\mu\text{A}$  at a 1750V bias) was modeled using Verilog-A as noise sources distributed in the FEM. The thermal noise from the high resistivity sheet was modeled by the resistors in the FEM grid implemented in H-SPICE, although it is optional to include it since it is about 100x lower than the shot noise of the PSAPD. The bulk and surface leakage currents were not modeled since these DC currents will be blocked by an AC coupling capacitor. A probability distribution of this noise at the four corners was estimated, and this probability distribution was sampled from for each light photon that hit.

The gain of the PSAPD has a variance which is described by Poisson statistics. Since the number of light photons in each typical interaction is large (over 10,000 for 511 keV photoelectric event), the distribution is approximated as Gaussian in Matlab. The avalanche process in the PSAPD generates current fluctuations which degrade performance by an excess noise factor, which is assumed to be 2.5 (Shah, 2005).

The shot noise due to the light signal is a type of proportional noise. It is difficult to create a detailed model since it is a time-varying noise process. Therefore, it was treated in the same manner in which secondary scintillator effects such as non-proportionality were treated. That is, it was assumed to be an additional variance, with standard deviation chosen so that the sum of all the noise sources matched the experimentally measured energy resolution. Again, fortunately, the contribution of this type of noise to the flood histogram simulation is minor (Lau et al., 2010).

The four corner outputs of the PSAPD model were connected to an H-SPICE model of the preamplifier and shaper via the signal conditioning circuits from Figure 3.16 and Section 4.3. Voltage pulses were created at the spatial channel shaper outputs. The peak of the voltage pulses was identified since there is a peak detector in the RENA-3. We created a probability distribution of the noise of the RENA-3 preamplifier based on experimental data, and sampled from this distribution to add noise to each event.



### 4.1.3 Simulation of flood histogram

Figure 4.1 outlines how the noise sources were combined with the total signal to obtain the total signal for each spatial channel. For example, for the first corner, the total signal,  $A$ , was  $A = A_{light} + A_{noise} + \delta_A + kA_{light}$ . The total signal at each corner,  $A$ ,  $B$ ,  $C$ , and  $D$ , was used to calculate the position  $(x, y)$  of the interaction:

$$\begin{aligned} x &= \frac{(A - B) + (D - C)}{A + B + C + D} \\ y &= \frac{(A - D) + (B - C)}{A + B + C + D} \end{aligned} \quad (4.1)$$

This entire process was repeated for one thousand values of  $N$ , representing one thousand 511 keV photon interactions in that crystal. Then, this was repeated for every crystal in the array to obtain a 2-D histogram (flood) for the entire array. This framework for modeling, simulating, and analyzing the detector and front-end electronics will be used to study the multiplexing and signal conditioning schemes used in the breast-dedicated PET system.

## 4.2 PSAPD analog signal multiplexing

As seen in the overview of the breast-dedicated PET system (Chapter 3), the tight packing of the detectors prevented the placement of the RENA-3 ASICs close to the detectors. Therefore, dense interconnect was required between the detectors and the front-end ASIC. This section will describe the method used to multiplex some of the analog signals on the interconnect to simplify the interconnect and readout electronics (also presented in Lau et al. (2010)).

Multiplexing has previously been used for photomultiplier tubes (PMTs) (Siegel et al., 1996; Doshi et al., 2001; Popov et al., 2001, 2006; Olcott et al., 2005). Multiplexing has also been investigated for silicon photomultiplier detectors (Olcott et al., 2009). However, PSAPDs typically have a factor of 1000 to 10,000 less gain than PMTs and silicon photomultipliers. This lower gain limits the number of channels that can be multiplexed together before the energy, time, and spatial resolution of the

system are degraded. None of the prior work on multiplexing avalanche photodiodes (APDs) can be used in our design. Since our limitation is in the wiring from the detector to the ASIC, APD multiplexing ideas in prior work, such as digital multiplexing (Shimazoe et al., 2006) and analog front-end multiplexing inside an ASIC (Abreu et al., 2006), do not address our issues. Zhang et al. (2006) solved a similar problem using transformers, but transformers have the disadvantage of being bulky and cannot be used in our solution.

### 4.2.1 Analog signal multiplexing configuration

The readout circuit for two PSAPDs with multiplexing implemented in our breast-dedicated PET system is shown in Figure 4.3. The output terminals of the spatial channels of the two PSAPDs are connected directly together. In our design, this connection is done directly on the Dual-LYSO-PSAPD flexible circuit, as shown in Figure 3.4. The common signals are kept independent (un-multiplexed) so the LYSO-PSAPD in which an interaction occurred can be identified. Unlike multiplexing schemes where the channel count is reduced after the first stage of electronics (Shimazoe et al., 2006; Abreu et al., 2006), this scheme multiplexes the PSAPD spatial channel outputs directly. Since the multiplexing is performed on the analog PSAPD outputs instead of on the signals after digitization, this proposed technique is called “analog signal multiplexing”. This multiplexing scheme is feasible with the PSAPDs used in our system which have a gain of about 1000, unlike the APDs used in other designs which only have a gain of about 50-150 (Grazioso et al., 2005; Abreu et al., 2006; Pichler et al., 2004; Grazioso et al., 2006; Judenhofer et al., 2007). In those designs, there is a preamplifier and associated circuitry for every APD pixel. Other designs with PSAPDs (Shah et al., 2004) need four spatial channel preamplifiers for one scintillation crystal array coupled to one PSAPD. In contrast, we multiplex two PSAPDs together, enabling the readout of two scintillation crystal arrays coupled to two PSAPDs using four spatial channel preamplifiers.

This approach obtains time information from the un-multiplexed common and position information from the multiplexed spatial channels. Energy information can be

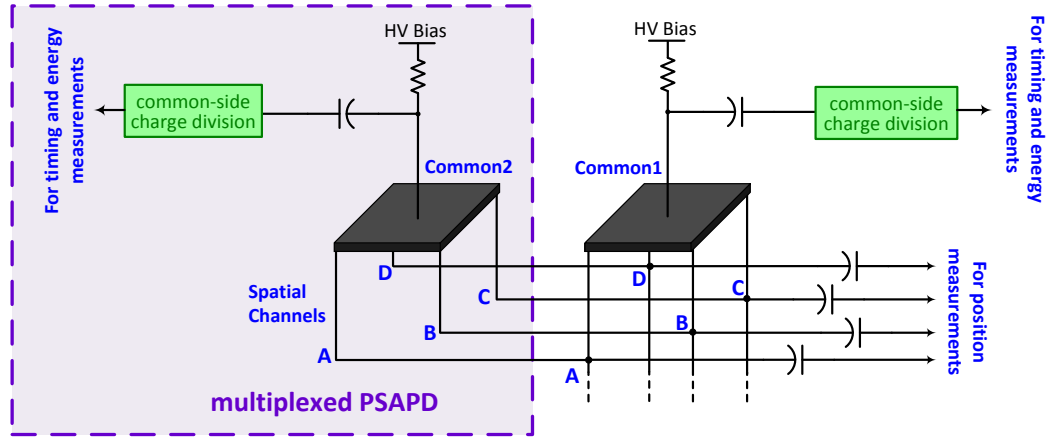


Figure 4.3: Multiplexing circuit configuration. Simplified version of Figure 3.15, with emphasis on circuit configuration for multiplexing.

obtained from either the un-multiplexed common or the sum of the spatial channels. In contrast, Zhang et al. (2006) ignored the common terminal and obtained energy, time, and position information from the multiplexed spatial channels. Although their technique requires one less channel, the disadvantage is that there may be degradation in energy and time measurements. In addition, their technique cannot reject interactions that occurred in both PSAPDs of the dual-module.

This study furthers the work done by my Stanford colleague (Olcott et al., 2005) by doing a more thorough study of the multiplexing scheme on the detectors and electronics used in the breast-dedicated PET system. Another modification is that this scheme multiplexes the signals before the AC coupling capacitors instead of after. This allows the number of AC coupling capacitors to be halved and the channels to be multiplexed directly on the Dual-LYSO-PSAPD flexible circuit, reducing the number of traces coming out of the detector.

### 4.2.2 Simulation and experimental setup

A good multiplexing scheme should not degrade the performance of the system. To study this, the detector and circuits, including their noise components, were modeled using the framework described in Section 4.1. A SNR simulation was also done to predict whether multiplexing would affect the energy, time, and spatial resolution of

the system. To simulate the signal, a 511 keV photon was assumed to interact in the detector, and a voltage pulse was generated at the output of the preamplifier and shaper in the RENA-3 chip. Since the RENA-3 contains a peak detector, the peak of the pulse was recorded and denoted as the signal. Using the noise simulations described in Section 4.1, the output referred noise was computed, and then the SNR was computed. This SNR simulation assumed that the charge divided equally to the four corners of the PSAPD, so it is mainly relevant for the case when the interaction occurred at the center of the scintillation crystal array. To consider the case when the interaction is not necessarily at the center, a flood histogram simulation was performed, using the simulation framework described in Section 4.1.

The simulations were verified experimentally using ceramic-mounted PSAPDs (Figure 4.4) since the ceramic package has pins allowing easier mounting on printed circuit boards for testing. Each  $1\text{cm}^2$  PSAPD was coupled using optical grease to an  $8\times 8$  array of  $1\text{mm}^3$  LSO scintillation crystals to create a ceramic-mounted LSO-PSAPD detector. In this experiment with the ceramic-mounted detectors, LSO crystals were used instead of LYSO since it was only later in the project that we switched to LYSO due to the cost savings and similar performance. Also, the RENA-3 evaluation board (designed by NOVA R&D) which contained the RENA-3 ASIC and AD9243 analog-to-digital-converter (ADC) was used for data acquisition. In the final system, this evaluation board was replaced with the RENA-3 board designed at Stanford, described in Section 3.4.

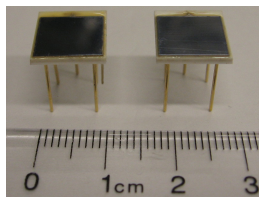


Figure 4.4: Ceramic-mounted PSAPDs used in multiplexing study

In both the simulation and experiment, the common-side charge division circuit described in Section 3.5.1 was used. On the spatial channels, the signal conditioning circuit used was the one that will be described in Section 4.3.1 because at that time, we found it was suitable for the short traces in this test setup. Eventually the final

system used another signal conditioning circuit, described in Section 4.3.4, but this experiment was performed before those changes were made.

For energy and flood measurements, the detector was flood irradiated with a  $4\mu\text{Ci}$  Na-22 point source placed 1.5 cm above the LSO array with a face-on configuration (see Figure 3.6). Per-crystal energy differences were compensated (method described in Section 2.2.2) to produce a single overall gain-corrected energy spectrum for each array.

In addition to windowing the flood histograms on 440 to 590 keV events (which represents events in the 511 keV photo-peak), low energy windows were also used (energy windows 200-300keV and 300-400keV). This was done to evaluate the system's ability to localize the coordinates of individual interactions outside the 511 keV photo-peak created by Compton scatter or photoelectric absorption of lower energy photons. Including these low energy events may be useful in improving system sensitivity, as will be described in Section 4.2.4. The events are windowed using the gain corrected energy spectrum from the low-gain common.

For the pair coincidence time resolution measurements, two PSAPDs were configured edge-on, pointing toward each other with 5.2 cm separation. A 250  $\mu\text{m}$  diameter  $10\mu\text{Ci}$  Na-22 source was placed between the two LSO-PSAPD detectors so that it irradiated the LSO arrays edge-on. The coincidence time resolution was corrected in post-processing for amplitude walk, correlated noise, and crystal location using convex optimization (Reynolds et al., 2010b).

Single photon count rate measurements were performed to evaluate sensitivity. Two ceramic-mounted LSO-PSAPDs were irradiated edge-on with a  $10\mu\text{Ci}$  Na-22 source, with one PSAPD in the front (labeled "PSAPD #1") and one PSAPD in the back (labeled "PSAPD #2"), as shown in Figure 4.5. The edge of the LSO crystal array in the front was 3.6 cm away from the source and the edge of the LSO crystal array in the back was 5.9 cm away from the source. Data was acquired for a period of time (ranging from 6 to 7 minutes) and the number of energy depositions detected was recorded. From that, the number of detected single photon events per second was calculated. For the multiplexed case, PSAPD #1 and PSAPD #2 were multiplexed together.

The SNR, energy resolution, time resolution, crystal identification, and sensitivity of the architectures were compared using simulation and experiment. All error bars in the results were estimated by determining the statistical error in the measurement and using error propagation formulas; systematic error was not accounted for.

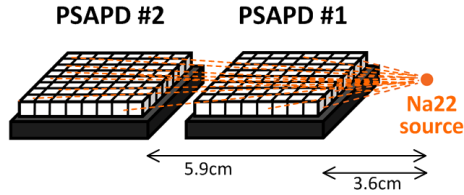


Figure 4.5: Experimental setup to evaluate sensitivity with and without multiplexing.

### 4.2.3 Simulation results

#### Signal-to-noise ratio (SNR) simulation

As shown in Table 4.2, SPICE simulations showed an almost negligible  $1.9 \pm 1.3\%$  degradation in SNR for the spatial channels from multiplexing. No significant SNR difference was observed for the low and high gain common signals. The simulation produced a SNR of 16.2 for the low gain common. This result was as expected since the simulation assumed an energy resolution of 14.5% FWHM ( $\sigma=6.17\%$ ) for the low gain common and  $1/0.0617 = 16.2$ .

Table 4.2: Multiplexing study SNR from SPICE simulations (signal is generated from the energy deposited by a 511 keV photon)

Channel	No multiplexing	Multiplexing
Low gain common	$16.2 \pm 0.1$	$16.2 \pm 0.1$
High gain common	$16.3 \pm 0.1$	$16.3 \pm 0.1$
Spatial channel	$10.5 \pm 0.1$	$10.3 \pm 0.1$

The simulated SNR for the low gain and high gain commons were unchanged with multiplexing, predicting that the energy and time resolution of the system would not be affected by multiplexing since the energy and time is measured from the non-multiplexed commons. The SNR of the spatial channels decreased by  $1.9 \pm 1.3\%$

(Table 4.2), predicting that the spatial resolution and the flood histograms should only degrade slightly.

### Flood histogram simulation

The simulated flood histograms and the computed Figure of Merits (FoMs) are shown in Figure 4.6. As we will explain in Section 4.2.4, it is also useful to separate the FoM into its two components — the distance between the peaks and the width of the peaks in the flood histogram — to understand why the FoM degrades. Figure 4.7 shows these two components used in the inner FoM calculation (definition of inner FoM in Table 2.3). With multiplexing, the distance decreases and the width increases.

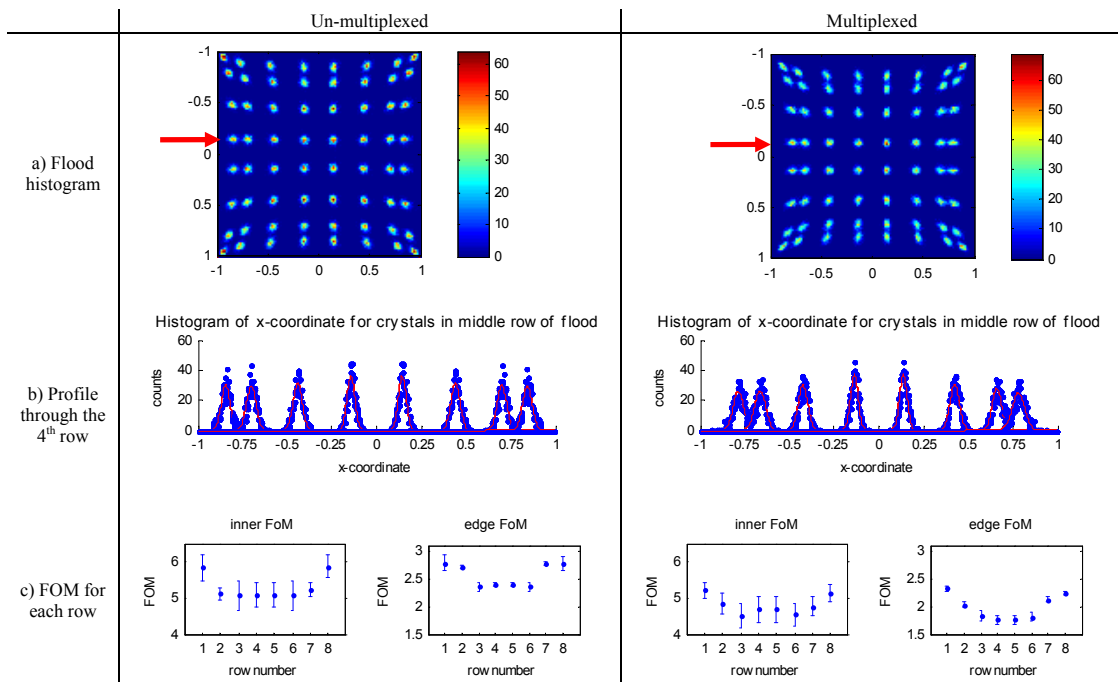


Figure 4.6: Multiplexing study simulation results, assuming face-on irradiation of an  $8 \times 8$  array of  $1 \text{ mm}^3$  LSO crystals coupled to a PSAPD (Lau et al., 2010). a) flood histograms, b) profile through the 4th row of the flood, c) Inner FoM and Edge FoM for each row of the flood (definition of inner FoM and edge FoM in Table 2.3). A small degradation is seen.

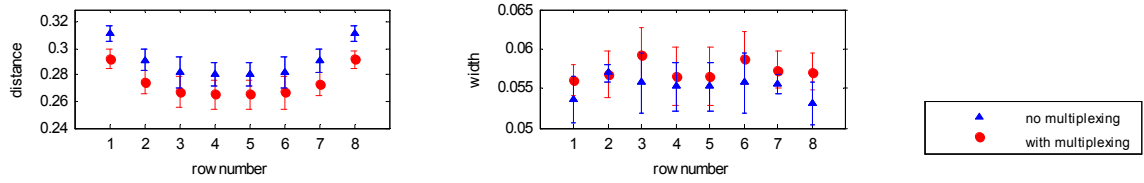
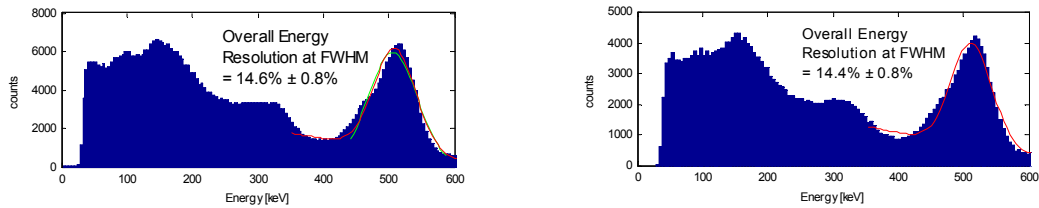


Figure 4.7: Multiplexing study simulation results: average distance between peaks and average width (FWHM) of the inner peaks for each row in the flood histogram in Figure 4.6, comparing the un-multiplexed and multiplexed results. The values for the distance and width are relative to the grid used for the flood histogram which has a maximum range spanning from -1 to 1. The small degradation in the FoM is due to both the decrease in distance between peaks and the increase in the width of the peaks (Lau et al., 2010).

## 4.2.4 Experimental results

### Energy and time resolution

The overall energy spectrum for the data obtained from the common channel is in Figure 4.8. The data has been compensated for per-crystal gain differences using the method in Section 2.2.2. The overall energy resolution for the face-on flood irradiated ceramic-mounted LSO-PSAPD detector is  $14.6\% \pm 0.8\%$  FWHM for the un-multiplexed case and  $14.4\% \pm 0.8\%$  FWHM for the multiplexed case.



a) Overall energy spectrum for un-multiplexed case. Overall energy resolution is  $14.6\% \pm 0.8\%$  FWHM for the 511 keV photopeak.

b) Overall energy spectrum for multiplexed case. Overall energy resolution is  $14.4\% \pm 0.8\%$  FWHM for the photopeak.

Figure 4.8: Multiplexing study experimental results: overall energy spectrum, after calibrating out per-crystal gain differences, obtained from the common channel of the PSAPD (Lau et al., 2010).



The coincidence time resolution, measured in an edge-on configuration, was  $7.3 \pm 0.2$  ns paired for the un-multiplexed case and  $7.3 \pm 0.2$  ns paired for the multiplexed case, as shown in Figure 4.9.

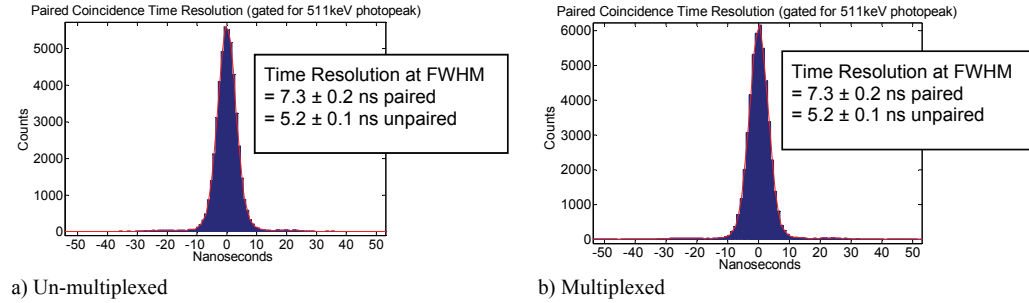


Figure 4.9: Multiplexing study experimental coincidence time resolution for events in the photo-peak (i.e., events with energy 440-590 keV), using the RENA-3 ASIC (leading edge discriminator) (Lau et al., 2010).

The experimental results for energy and time resolution for events in the 511keV photopeak with and without multiplexing are the same within statistical errors (see Figures 4.8 and 4.9). This is expected since the common was not multiplexed. This was also predicted by the SPICE simulation which showed that the SNR of the low gain common was unchanged with multiplexing. It was also expected that the timing resolution doesn't degrade because from Equation 2.24, timing jitter is related to the voltage noise and the slope of the output waveform, and both these parameters did not change significantly since the common terminal was not multiplexed.

### Flood histograms

The flood histograms, profiles, and FoM for the flood irradiated detectors for the 511keV photo-peak are shown in Figure 4.10. Figure 4.11 shows the distance between the peaks and the average width of the peaks for each row in the flood histogram. Flood histograms were created for two energy ranges outside the 511keV photopeak: 200-300 keV and 300-400 keV, shown in Figure 4.12.

The flood histogram FoM (Figures 4.6 and 4.10) show that there is a small degradation due to multiplexing which is tolerable because individual crystals are still

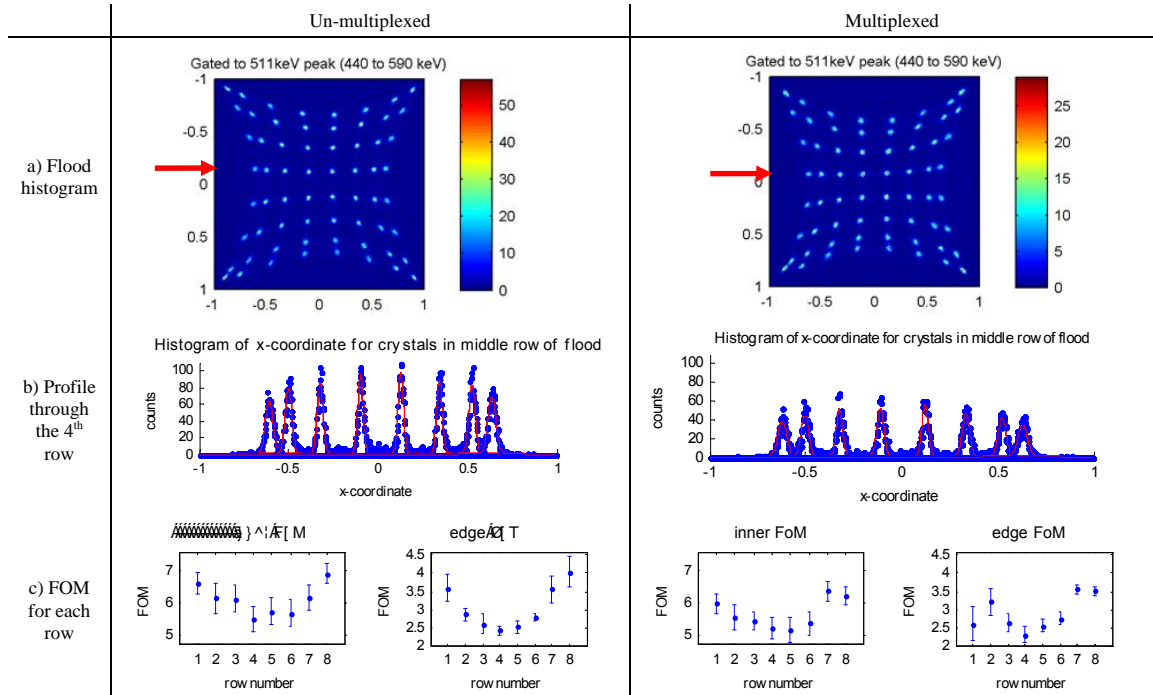


Figure 4.10: Multiplexing study experimental results for events in the photo-peak (i.e., between 440 and 590 keV) a) Flood histograms. b) Profile through the 4<sup>th</sup> row of the flood. The total acquired number of photons that hit the PSAPD of interest was less for the multiplexed case, so those peaks are lower. c) Inner FoM and Edge FoM for each row of the flood (definition of inner FoM and edge FoM in Table 2.3). For all figures, the overall energy spectra from Figure 4.8 was used to gate for events in the photo-peak (Lau et al., 2010).

well separated. The FoM is a useful metric for quantitatively comparing flood histograms as it captures the degradation in the flood histogram due to multiplexing while avoiding issues with binning and background that are inherent in the peak-to-valley ratio metric. In both the simulated and experimental results (Figures 4.7 and 4.11), the width increases and the distance between peaks decreases, so both factors contributed to the degradation in FoM. The increase in the width of the peaks was due to the increase in PSAPD leakage current noise and thermal noise. Also, the effective detector capacitance as seen from the spatial channels doubled, which increases the input-referred noise of the preamplifiers (see Section 2.3.1). The decrease

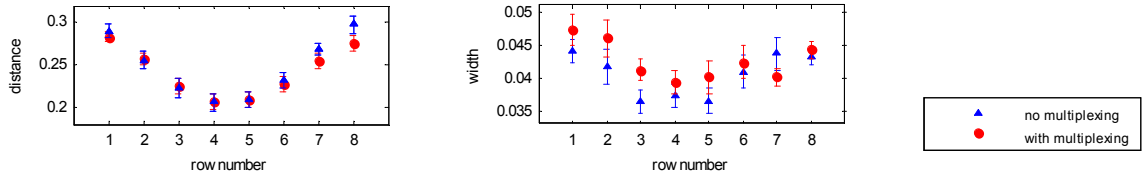


Figure 4.11: Multiplexing experimental results: average distance between peaks and average width (FWHM) of the inner peaks for each row in the flood histogram. The values for the distance and width are relative to the grid used for the flood histogram which has a maximum range spanning from -1 to 1 (Lau et al., 2010).

in the distance between the peaks occurs because connecting the spatial channels together connected the sheet resistors of the two PSAPDs in parallel, effectively halving the sheet resistance. Since the preamplifiers have finite input impedance, reducing the sheet resistance increases the amount of charge sharing between the four corners and thus decreases their dynamic range. This results in a compression of the flood histogram. The decrease in the distance between peaks is not captured by the SNR, so the simulated flood histogram is useful for understanding the crystal identification ability.

The small discrepancies between the simulation and the ceramic-mounted detector experimental data can be attributed to a number of factors. Estimates were used for parameters such as noise, PSAPD sheet resistance and avalanche gain, preamplifier input capacitance, preamplifier gain and dynamic range, and scintillation crystal light output and quantum efficiency. In reality, these parameters vary from detector-to-detector by up to 10% due to process variations. There is less “pin-cushion distortion” in the simulation (Figure 4.6). This caused discrepancies in the percent degradation with multiplexing in the distance between peaks for inner crystals and in all the results for the edge crystals. This may be because the position and size of the contacts on the PSAPD high resistivity sheet may be slightly different from the estimate. The pin-cushion distortion is highly dependent on the value of parameters used for the sheet resistance and capacitance of the PSAPD as well as the input impedance of the preamplifier. In addition, there are secondary effects that are not modeled in simulation, such as the non-uniform gain of the surface of the PSAPD and the

saturation of the preamplifier for large signals. Although the absolute numbers for the simulation and the experiment cannot be compared, the trend and the conclusion for all three studies is the same: multiplexing degrades the FoM slightly, but all the crystals in the flood histogram can still be clearly identified.

### **Detection of low energy events**

System photon sensitivity is improved by including energy depositions outside the 511keV photo-peak due to the high chance that Compton scattered photons will escape the small ( $1 \text{ mm}^3$ ) scintillation crystal elements. The detectors can localize the 3-D coordinates of these individual interactions, provided each interaction is above the electronic noise threshold, which currently is 200keV. Monte Carlo simulations showed that only about 42% of all events have individual interaction energy depositions above 400keV whereas about 61% of all events have individual energy depositions above 200 keV (“all events” refers to events where the sum of all the individual energy depositions in that event sum to an energy value within the photo-peak window (Gu et al., 2010)). Algorithms (Pratx and Levin, 2009) can estimate the first interaction location for an event comprising a sequence of multiple interactions. Figure 4.12 showed that the crystals are still easily separable for interaction energy depositions from 200 to 400keV. Hence, these low energy events may be used to possibly improve system sensitivity (Gu et al., 2010). However, the raw time resolution degrades (Table 4.3) so we are studying how to best extract time information from multi-interaction photons.

The time resolution for coincidence between an interaction in one detector with energy outside the 511keV photopeak (200-300keV, 300-400keV) with an interaction in the other detector with energy within the 511keV photopeak is in Table 4.3.

### **Sensitivity**

To evaluate sensitivity, the count rate, defined as the number of events per second recorded by each PSAPD in the edge-on arrangement, is shown in Table 4.4.

The count rate for each PSAPD (PSAPD #1 or PSAPD #2) was similar with or

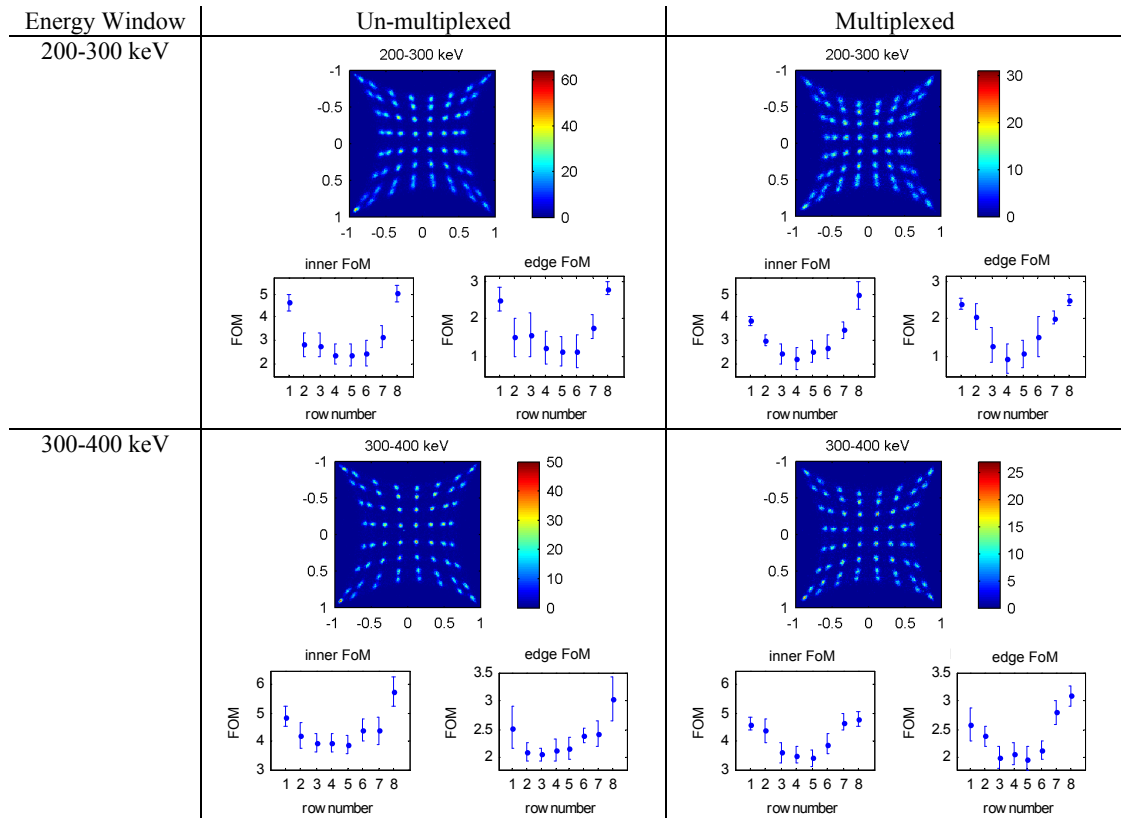


Figure 4.12: Multiplexing experimental low energy window results: Flood histograms, inner FoM, and edge FoM with and without multiplexing for events in two energy windows outside the photo-peak (Lau et al., 2010).

without multiplexing of the spatial channels, which was expected since the number of events was measured from the common which was not multiplexed. The small discrepancies between the numbers could be due to experimental error, such as small differences in the manual placement of the source. In both the un-multiplexed and multiplexed case, the number of events per second was larger in PSAPD #1 than in PSAPD #2 because PSAPD #1 was closer to the source.

Table 4.3: Coincidence Time Resolution for Interaction Between Event in an Energy Window Outside the PhotoPeak with an Event in an Energy Window Inside the Photopeak

	Energy Window Outside the Photopeak	
	200-300 keV	300-400 keV
<b>Un-multiplexed</b>	$13.7 \pm 0.1$ ns paired	$8.8 \pm 0.1$ ns paired
<b>Multiplexed</b>	$18.9 \pm 0.1$ ns paired	$10.5 \pm 0.1$ ns paired

Table 4.4: Count Rate (Number of Events Per Second in each PSAPD)

	All events (above noise floor)		Photo-peak events ( $\sim 440$ - $590$ keV)	
	PSAPD #1	PSAPD #2	PSAPD #1	PSAPD #2
<b>Un-multiplexed</b>	$282.2 \pm 0.8$	$77.4 \pm 0.4$	$70.2 \pm 0.4$	$14.7 \pm 0.2$
<b>Multiplexed</b>	$286.3 \pm 0.9$	$75.2 \pm 0.5$	$72.6 \pm 0.4$	$14.8 \pm 0.2$

#### 4.2.5 Conclusions from multiplexing study

Multiplexing two PSAPDs together reduces the number of signal routing traces from the detector to the front-end electronics. This advantage is particularly relevant for high resolution PET with DOI where there are many tightly packed detectors and a large distance between the detectors and front-end electronics. Since the common is split into two readout channels close to the ASIC (for the dynamic range scaling, see Section 3.5.1), only one long common routing trace is needed per PSAPD. Therefore, without multiplexing, there are 2304 modules and 10 routing traces per module (4 spatial + 1 common + 4 spatial + 1 common), resulting in 23,040 traces. With multiplexing, there are 6 routing traces per module (4 spatial + 1 common + 1 common) so there are 13,824 traces, a 40% reduction.

Multiplexing also reduces the number of readout channels, decreasing the system cost and complexity. Originally, with 2304 Dual-PSAPD modules and 12 signals per module (4 spatial + 2 common + 4 spatial + 2 common; see Section 4.2.1), 27,648 readout channels would be needed. With the multiplexed design, which has 8 signals per module (4 spatial + 2 common + 2 common), 18,432 channels are needed, a 33% reduction. This is a significant improvement, although system integration is still not trivial.

What limits the number of detectors that can be multiplexed together in a system?

To first order, the gain and SNR of the detector are the most limiting effects. Although the noise of the common does not increase, the noise of the spatial channels does. In addition, inter-module scatter within a group of multiplexed detectors cannot be positioned to the correct module, resulting in a reduction in contrast. Gu et al. (2010), found that multiplexing the two PSAPDs on our Dual-PSAPD module results in only  $<0.4\%$  reduction in the number of detected events when used in our system geometry.

Finally, the signal rate from multiplexed detectors cannot exceed the count rate performance of the electronics. Multiplexing allows more PSAPDs to be readout by a single RENA-3 chip and also doubles the number of events measured on each spatial channel. However, this should not be a problem for the RENA-3 in our system since preliminary simulations showed that the predicted maximum count rate per RENA-3 with multiplexing in should be only 15kHz whereas the RENA-3 can handle over 80kHz of events (NOVA R&D, 2007). Note that we did have a count rate limitation in the existing system used to acquire phantom data for this thesis, as explained in Section 3.4, but that was due to the bandwidth of the preliminary backend electronics, not the RENA-3, and work is ongoing to remove this limitation in the future.

In conclusion, both simulation and experiments showed that the analog signal multiplexing scheme did not significantly degrade energy, temporal, spatial, or count rate performance. This multiplexed front-end architecture reduced wire routing density by 40% and the number of required readout electronics input channels by 33%.

### 4.3 Signal conditioning

The flood histogram shape and crystal identification ability is dependent on various factors, including the magnitude of the signal from the detector, the input impedance and noise of the front-end charge sensitive amplifier, and any extra signal conditioning circuitry added before the charge sensitive amplifier.

The magnitude of the signal produced by the detector is important because if it is small compared to the noise of the detector and electronics, then the peaks in the flood histogram will be wide and the crystal identification will be poor. However, if the signal is too large, it will saturate the front-end electronics. As saturation gets

worse, the peaks at the corners of the flood histogram begin to move inward, as shown in Figure 4.13, and it becomes impossible to segment the peaks.

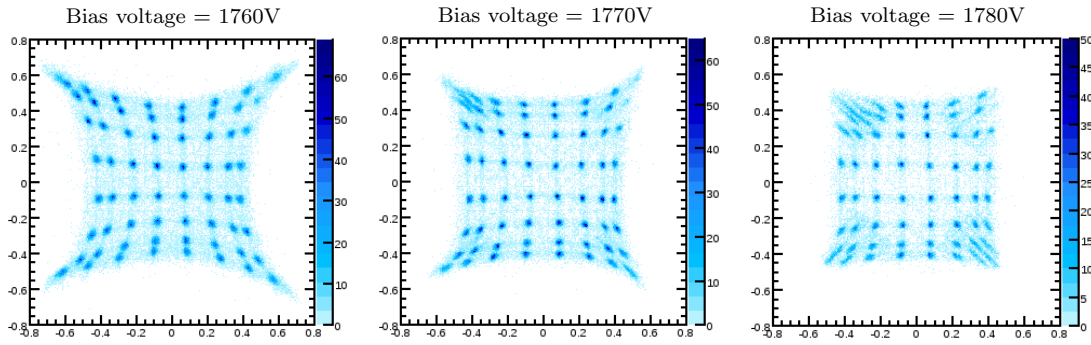


Figure 4.13: When the bias voltage is increased, the signal begins to saturate the electronics and the peaks at the corners of the flood histogram begin to move inward. Measurements are of detector module #398-9-1-1.

The detector signals exceed the dynamic range of the RENA-3 ASIC (Section 3.4). As explained in Section 3.5.1, this dynamic range problem was solved for the common signal by splitting the charge into a saturated and unsaturated common. For the spatial channels, splitting each signal into two channels was not feasible because that would have required over 9,000 additional readout channels in the system. In the process of designing this PET system, various techniques that do not require extra RENA-3 channels were investigated to prevent saturation of the spatial channels and to manipulate the shape of the flood histogram to improve crystal identification. These include shunt capacitor, shunt resistor, series capacitor, and charge sharing signal conditioning techniques. These methods were implemented with discrete capacitors and resistors on the Discrete Board (Figure 4.14). The method that was finally used in the system was the charge-sharing signal conditioning (Section 4.3.4).

### 4.3.1 Shunt capacitor signal conditioning

The signal could be attenuated by shunting some charge to ground using a capacitor. Figure 4.14 shows how the signal conditioning circuits for each spatial channel are connected to the PSAPD and Figure 4.15 shows the capacitor-based charge division



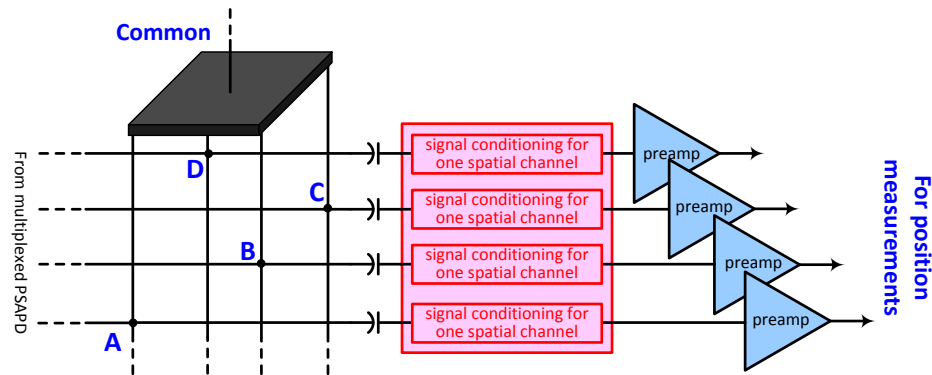


Figure 4.14: Signal conditioning circuits are added for each spatial channel as shown. The following sections will describe the details of the signal conditioning circuits.

circuit for one spatial channel. The fraction of charge that goes to ground depends on the ratio between  $C_{\text{atten}}$  and  $C_{\text{c,spatial}}$ . The ground of  $C_{\text{atten}}$  is connected to the analog ground pins of the RENA-3, which is the reference for the preamplifiers inside the RENA-3. The disadvantage of this method is that it increases the capacitance at the input of the preamplifier and hence increases the input-referred preamplifier noise (Section 2.3.1). So, whether this technique is suitable or not depends on the noise slope of the preamplifier and the  $C_{\text{atten}}$  needed for sufficient attenuation. This preamplifier noise restricts the absolute capacitance values from becoming too large.

On the other hand, choosing extremely small absolute capacitance values for  $C_{\text{c,spatial}}$  and  $C_{\text{atten}}$  is not beneficial either. If the capacitance values are smaller than the detector parasitic capacitance, then the charge from the detector will stay inside the detector rather than entering the preamplifier, decreasing the signal charge. This will be explained in more detail in Section 4.3.3 on series capacitor signal conditioning.

The same PSAPD as the one used to produce Figure 4.13 (#398-9-1-1), biased at 1770V, was connected to a capacitor-based signal conditioning circuit. With  $C_{\text{c,spatial}} = 75\text{pF}$  and  $C_{\text{atten}} = 22\text{pF}$ , it is not saturated anymore.  $C_{\text{c,spatial}} = 75\text{pF}$  in series with the RENA-3 effective input capacitance of  $30\text{pF}$  is about  $21\text{pF}$ , so about half the charge was shunted to ground through  $C_{\text{atten}}$ . Figure 4.16 shows how the flood histogram changed.

This method was used in the PSAPD analog signal multiplexing study (Section

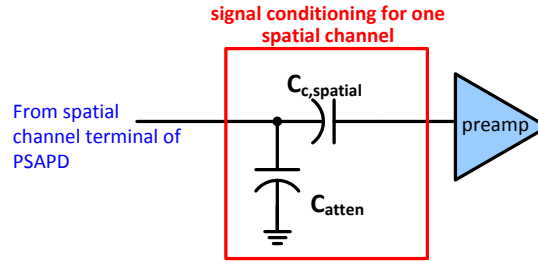


Figure 4.15: Capacitor-based signal conditioning scheme for the spatial channels.  $C_{atten}$  and  $C_{c,spatial}$  form a capacitive divider.

4.2). In that study, the RENA-3 evaluation board and ceramic-mounted capacitors were used. In that case,  $C_{atten}$  and  $C_{c,spatial}$  both equal to 1000pF provided sufficient attenuation and produced the best results.

### 4.3.2 Shunt resistor signal conditioning

Another method to attenuate the signal is to shunt some charge to ground using a resistor instead of a capacitor, as shown in Figure 4.17.  $R_{spatial}$  and  $C_{c,spatial}$  form a high pass filter which attenuates the some components of the signal. Figure 4.18 shows how the flood histogram changed when  $R_{spatial}$  was added to prevent saturation.

A detailed study of the influence of the resistor ( $R_{spatial}$ ) and capacitor ( $C_{c,spatial}$ ) values in the signal conditioning circuit and PSAPD bias voltage on the flood histogram and energy resolution was done and the results are in Lau et al. (2012c). An excerpt of the results are included here. The conclusion was that adding  $R_{spatial}$  allowed the signal to be attenuated without degradation in the flood histogram Figure of Merit (FoM) (Equation 2.6). For these experiments, the detector was flood irradiated at room temperature (22°C) with a 30uCi Na-22 point source 3.5cm away for 25 minutes to acquire 500,000 counts. These experiments were performed on two detector modules, Module 0 and Module 1 of #395-3-16. The PSAPD bias voltage was fixed at 1740V and  $C_{c,spatial}$  was fixed at 27pF.

The flood histograms for Module 1 with each  $R_{spatial}$  value is shown in Figure 4.19. Reducing  $R_{spatial}$  causes the spatial dynamic range of the flood histogram to expand, i.e., the x- and y-coordinates fill a larger portion of the range from -1 to 1. This does

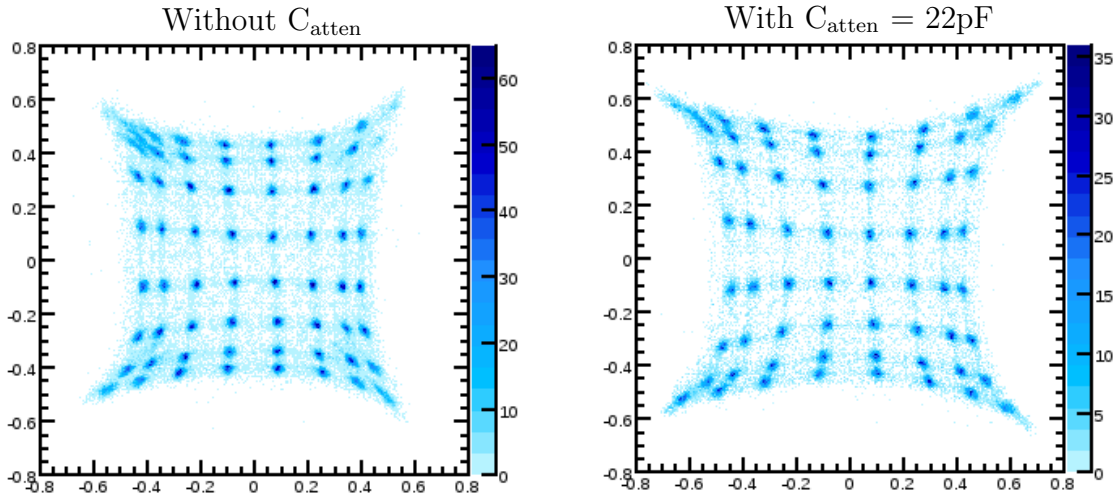


Figure 4.16: Flood histogram without capacitor to ground is slightly saturated. With the 22pF  $C_{\text{atten}}$  capacitor to ground, the peaks near the corners of the flood histogram become more well defined and are not pulled inward. Both floods are of detector module #398-9-1-1 at a bias voltage of 1770V (The flood histogram without  $C_{\text{atten}}$  is repeated from Figure 4.13 for ease of comparison).

not necessarily improve crystal identification, as the width of the peaks also increases.

Quantitative results for this study for both Module 0 and 1 are shown in Figure 4.20. The attenuation of the signal conditioning circuit increases when smaller  $R_{\text{spatial}}$  values are used (i.e., the gain, indicated by the ADC index, decreases). There is degradation in energy resolution, and hence SNR, when a low  $R_{\text{spatial}}$  value of 5k $\Omega$  is used. There is no clear optimal  $R_{\text{spatial}}$  based on the FoM metric since differences in FoM are less than the error bars of the experiment. This implies that the gain can be changed using  $R_{\text{spatial}}$  without degrading the FoM.

A flood histogram simulation paralleling the shunt resistor experiment was also done. The LYSO array, PSAPD, and signal conditioning circuit was simulated using the model and framework described in Section 4.1, where one thousand 511keV photon interactions were simulated. The results are in Figure 4.21. In the simulation results, the peaks in the flood histogram appear more well separated and the FoM is higher because intercrystal scatter is not modeled and there may be inaccuracies in the parameters chosen for the noise contributors. Pin-cushion distortion is over-estimated due to a number of factors not included in the simulation, such as the non-uniform

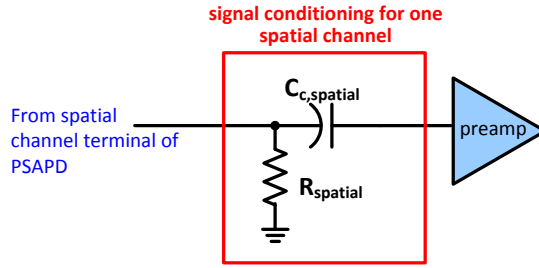


Figure 4.17: Resistor-based signal conditioning scheme for the spatial channels.

gain of the PSAPD, possible intrinsic non-linearity of the electronics, and error in the estimation of the size and position of contacts on the PSAPD. Therefore, the absolute value of the numbers obtained through the simulation cannot be compared with those obtained through the experiment. However, the trend seen in the simulation can be used to confirm the observation in the experiment that reducing  $R_{\text{spatial}}$  causes the spatial dynamic range of the flood histogram to expand.

Conceptually, the spatial dynamic range of the flood histogram expands when  $R_{\text{spatial}}$  is small since  $R_{\text{spatial}}$  dominated over the sheet resistance of the PSAPD, resulting in less sharing of signal between the spatial channels. To explain this further, we reduce the problem to one dimension and only consider two spatial channels, A and B, as shown in Figure 4.22, where the interaction is closer to A. The Anger logic formula for the x-coordinate simplifies as follows:

$$x \approx \frac{A - B}{A + B} = \frac{\frac{A}{B} - 1}{\frac{A}{B} + 1} \quad (4.2)$$

With a small  $R_{\text{spatial}}$  that is comparable or less than the PSAPD sheet resistance (5.2 k $\Omega$ ), the small  $R_{\text{spatial}}$  dominated over the sheet resistance of the PSAPD, resulting in less sharing of signal between A and B through the sheet resistance, and a larger ratio  $A/B$  ( $A/B > 1$ ). From Equation 4.2, this translates into a larger x-coordinate for this interaction, even though the values of  $A$  and  $B$  are smaller. Therefore, it results in a flood histogram with a larger spatial dynamic range. The width of the peaks in the flood histogram also increase proportionally though. Fig 4.23 shows how the ratio  $A/B$  changes when  $R_{\text{spatial}}$  changes.

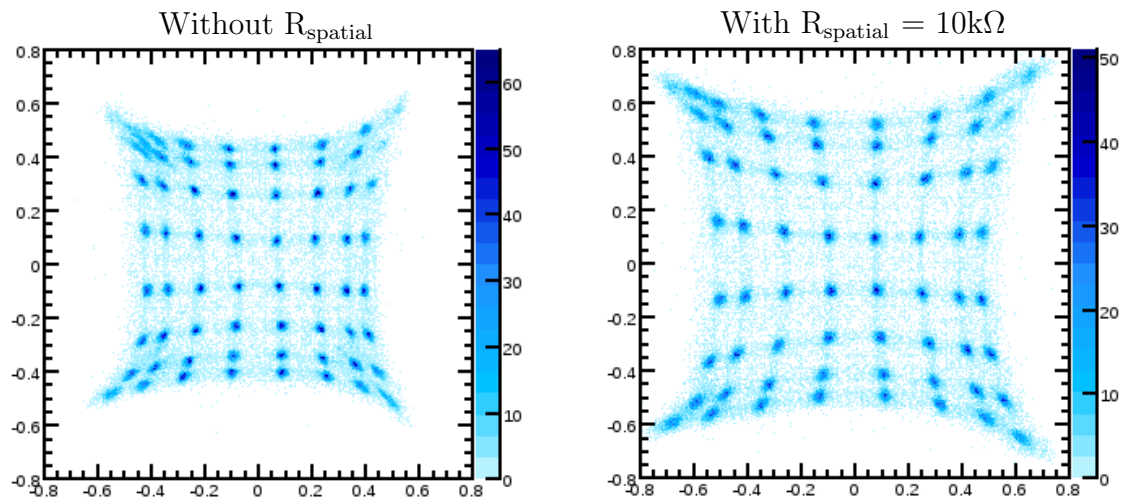


Figure 4.18: Flood histogram without resistor to ground is slightly saturated. With the  $10\text{k}\Omega$   $R_{\text{spatial}}$  resistor to ground, the peaks near the corners of the flood histogram become more well defined and are not pulled inward. Both experiments were with a bias voltage of  $1770\text{V}$  (The flood histogram without  $R_{\text{spatial}}$  is repeated from Figure 4.13 for ease of comparison).

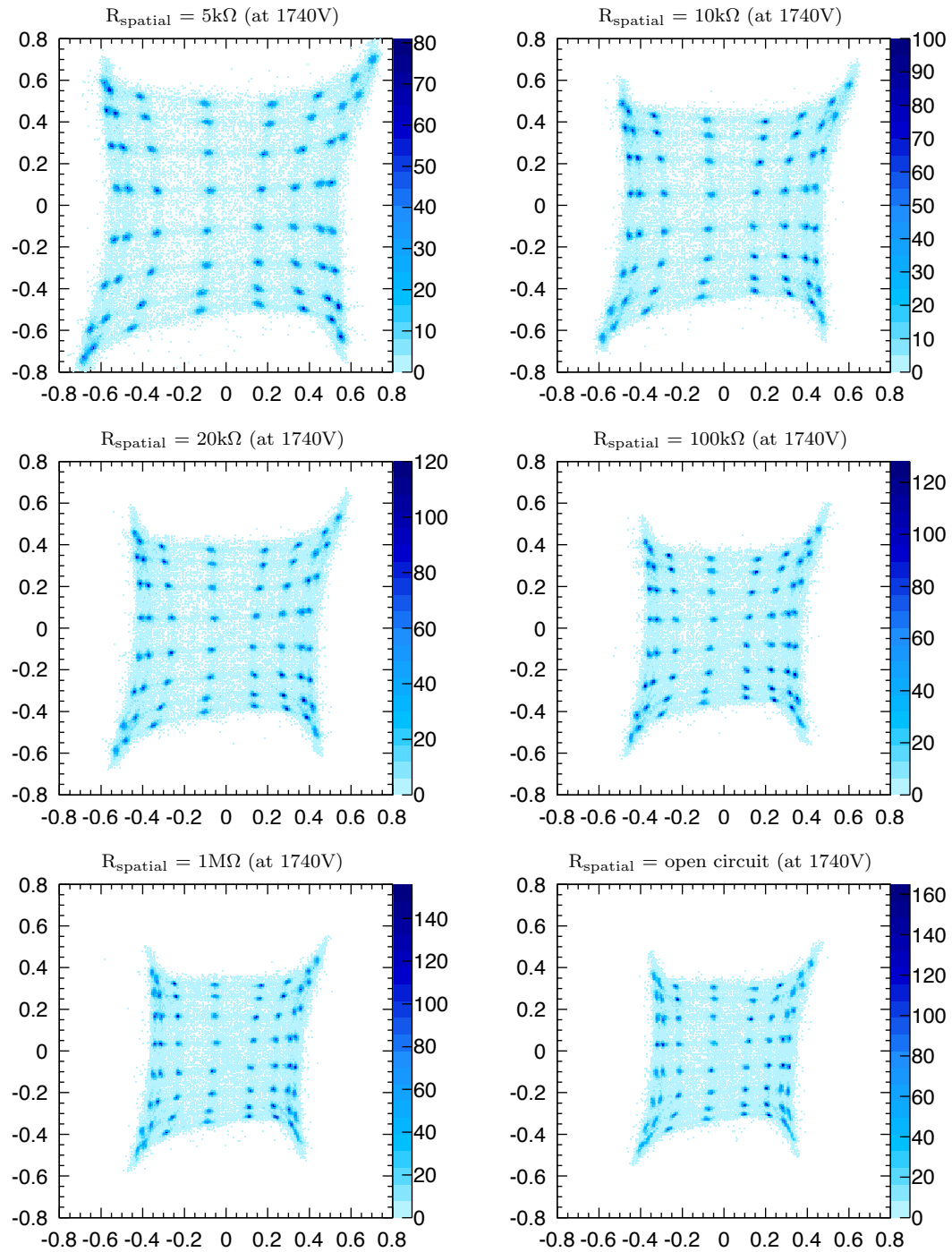
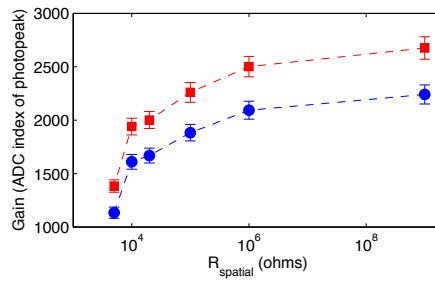
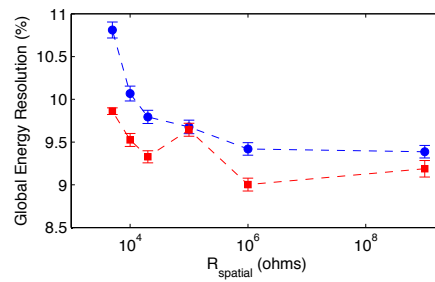


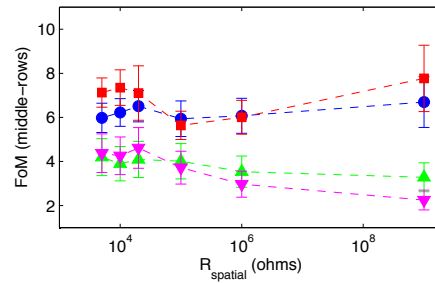
Figure 4.19: Shunt resistor signal conditioning experimental results: flood histograms for Module 1 for various values of  $R_{\text{spatial}}$  (Lau et al., 2012c).



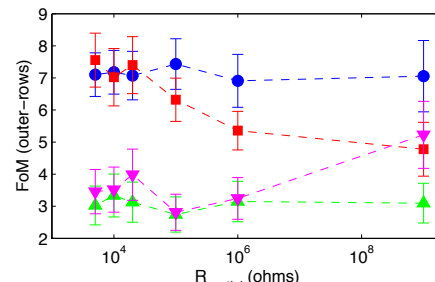
(a)



(b)



(c)



(d)

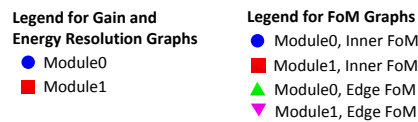


Figure 4.20: Shunt resistor signal conditioning experimental results: a) Gain, b) Global Energy Resolution, c) FoM of middle-rows, d) FoM of outer-rows. Error bars represent statistical error (standard error) in the measurement (Lau et al., 2012c).

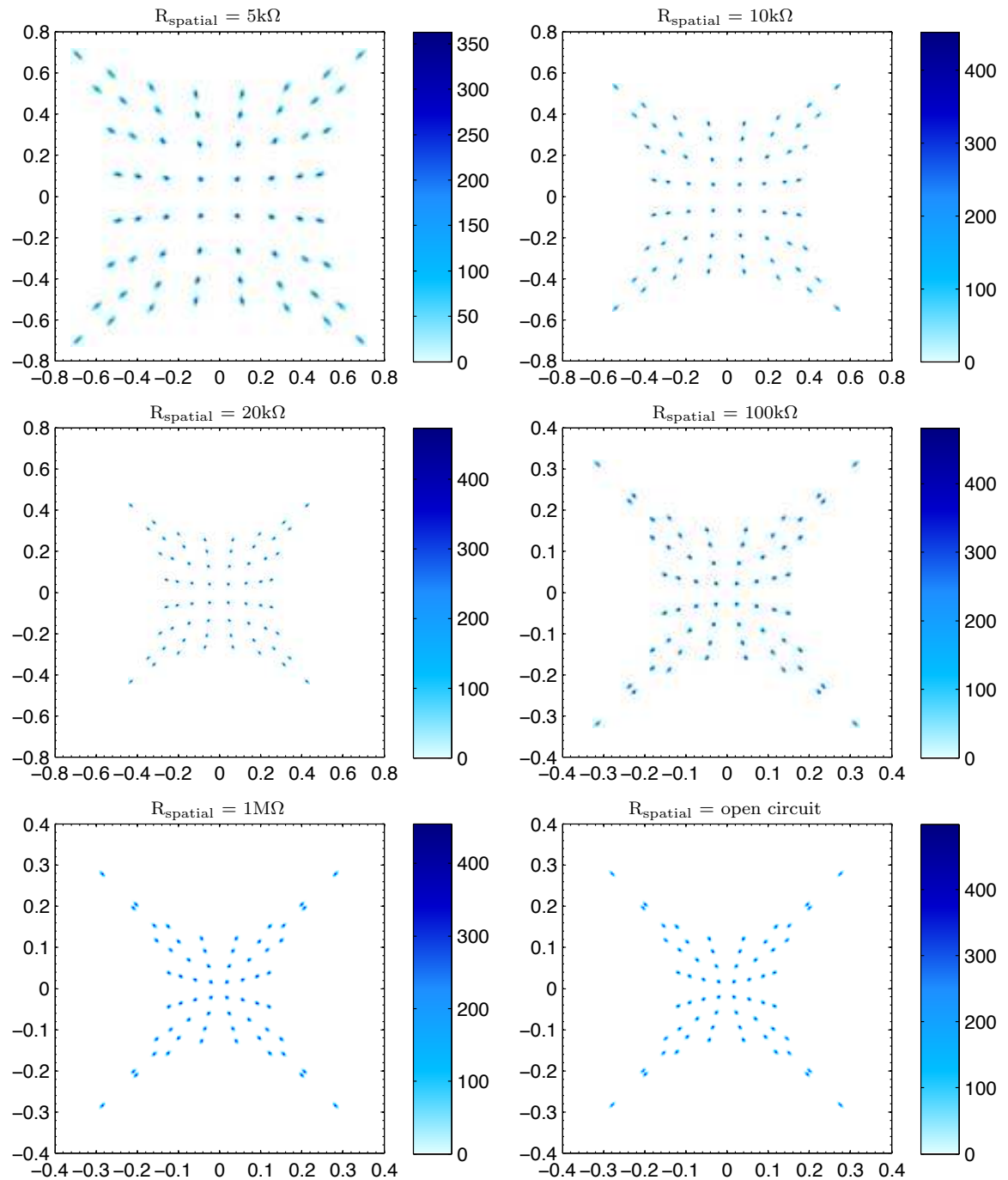


Figure 4.21: Shunt resistor signal conditioning simulation results: flood histograms for various values of  $R_{\text{spatial}}$ . Note that the axes were changed for  $100\text{k}\Omega$  and above Lau et al. (2012c).



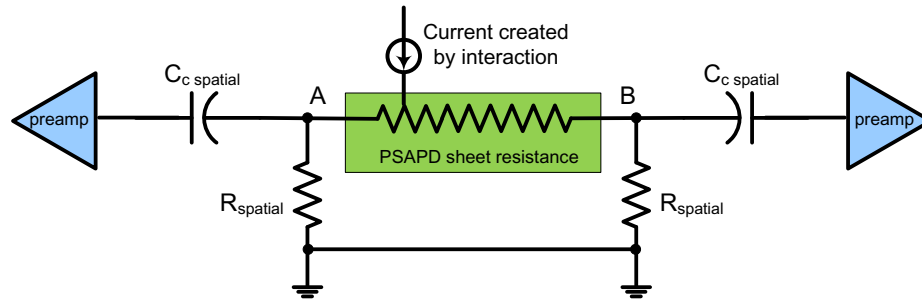


Figure 4.22: 1-dimensional simplification of the PSAPD. Interaction closer to spatial channel A than to spatial channel B.

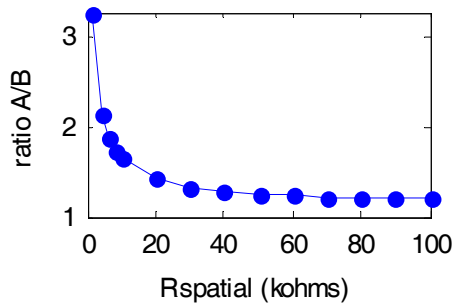


Figure 4.23: SPICE simulation of an interaction near the corner for spatial channel A of the PSAPD.  $R_{\text{spatial}}$  has a significant effect on the ratio between the peak signal at A and B when it approaches the sheet resistance of the PSAPD ( $5.2 \text{ k}\Omega/\text{square}$ ) Lau et al. (2012c).

### 4.3.3 Series capacitor signal conditioning

The capacitor in series with the preamplifier,  $C_{c,spatial}$ , can also be adjusted to scale the signal. This can be done in conjunction with the shunt capacitor or shunt resistor techniques, or done independently. If done independently, then the resulting signal depends on the value of  $C_{c,spatial}$  compared to the detector capacitance. As  $C_{c,spatial}$  is decreased, more charge will remain inside the detector on the detector capacitance, instead of flowing out of the detector, attenuating the signal. Also, since the impedance looking out of the detector is larger (relative to the PSAPD sheet resistance), there is more charge sharing between the spatial channels through the resistive sheet. This reduces the spatial dynamic range of the flood histogram, as shown in Figure 4.24.

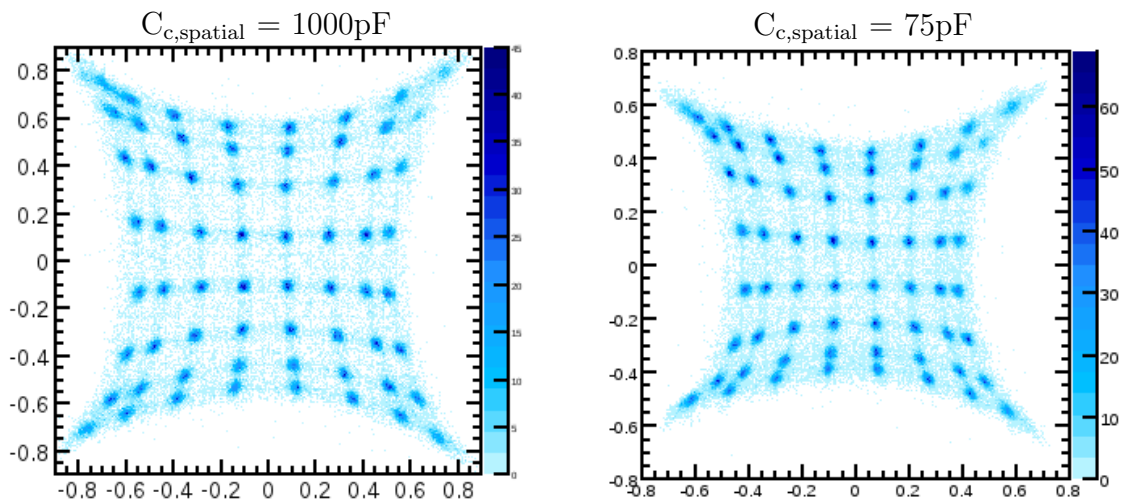


Figure 4.24: Reducing the series capacitor  $C_{c,spatial}$  attenuates the signal and reduces the spatial dynamic range of the flood histogram. In this measurement there was no shunt capacitor or resistor. Both floods are of detector module #398-9-1-1 at a bias voltage of 1760V.

### 4.3.4 Charge sharing signal conditioning

An interesting observation of the experimental floods shown so far in this section is that they appear slightly asymmetric. We found that this was not only seen in those two modules characterized, but it was a trend seen in most of the modules. The two

types of asymmetry seen are shown, exaggerated, in Figure 4.25. Figure 4.13 is an example of Side Compression (which was observed in the floods in Figure 4.16, 4.18 and 4.24) whereas Figure 4.19 is an example of Diagonal Compression (which was observed in Figure 4.19) .

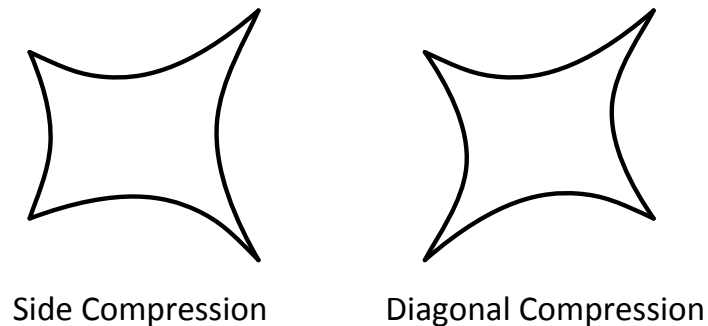


Figure 4.25: An exaggeration of the asymmetry observed in flood histograms: Side Compression (which was observed in the floods in Figure 4.16, 4.18 and 4.24) and Diagonal Compression (which was observed in Figure 4.19).

After some investigation, we found that the type of asymmetry was dependent on the order of the wires on the long FFC (flat flex cable). The wires on the FFC are in the order A-B-C-D. Figure 4.26 shows how the corners of the flood histogram were connected to the FFC wires in each case. Depending on the order in which the corners of the PSAPD are connected to the traces A-B-C-D on the FFC, the flood histogram becomes asymmetric, with either “Side Compression” or “Diagonal Compression”. The FFC cables could be up to 12 inches long, and the coupling capacitance between adjacent traces could be up to 12pF. There is parasitic coupling capacitance to two adjacent spatial channels for channel B and C, whereas parasitic coupling capacitance to only one adjacent spatial channel for A and D. The corners which only have one parasitic coupling capacitance appear compressed inward. The compression may be because the signal begins to saturate the RENA-3 when there is not enough parasitic capacitance. Saturation of the RENA-3 means the ratio of the signal measured at the different corners is smaller, resulting in the peaks near the corner of the flood histogram moving inward. So, a small amount of capacitance between the corners is actually good in helping pull the corners of the flood histogram

outwards. More coupling capacitance than necessary to prevent saturation causes charge sharing between the corners, decreasing the ratio between the signals and resulting in corners being pulled inward. So, it is important to have the coupling capacitance appropriately sized.

Note that Channel A and/or Channel D could be adjacent to a spatial channel trace for another module depending on the placement of the traces on the FFC (in Figure 4.26 it is shown that Channel D is adjacent to another trace). However, we found that this coupling capacitance doesn't have a significant effect on the shape of the flood histogram. That may be because that coupling capacitance does not connect to another terminal of the same PSAPD so the current return path through that parasitic capacitance is not as desirable (higher impedance).

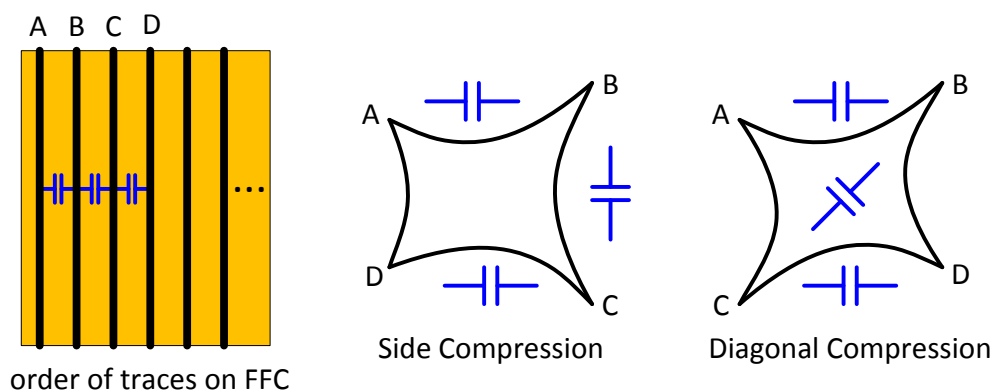


Figure 4.26: The type of asymmetry seen in the flood histograms depends on the order in which the four corners of the PSAPD were connected to the traces on the Flat Flexible Cable (FFC). The parasitic capacitance due to the FFC is shown in blue. This parasitic capacitance causes the flood histogram to have either Side Compression or Diagonal Compression.

Some coupling capacitance was actually beneficial because it prevented saturation of the RENA-3 and helped to “pull out” the corners of the flood histogram, making it easier to segment the peaks near the corners. We wanted to have all four corners “pulled out” in this manner, not just corners B and C. So, we decided to explicitly add four extra charge sharing capacitors. Specifically, we decided to connect the corners of the PSAPD to the FFC as shown in the Side Compression diagram, and then explicitly connect a capacitor between the pairs A and B, B and C, C and D,

and D and A. We considered only adding an explicit capacitor between D and A and just take advantage of the parasitic capacitance for the other pairs. However, the FFC length is variable, and we wanted to be able to use the same scheme regardless of the FFC length. We found that adding 43pF to each of the four pairs “pulled out” all four corners sufficiently for all the FFC lengths that would be used. 43pF was enough to dominate over the parasitic capacitance of the FFC (which was at most about 12pF), so the influence of the different FFC lengths was not that great. It was decided that the final breast-dedicated PET system would have four 43pF charge sharing capacitors and to use 75pF for  $C_{c,spatial}$ . Figure 4.27 shows the flood histogram achieved with this scheme. The results in Chapter 5 all use this scheme.

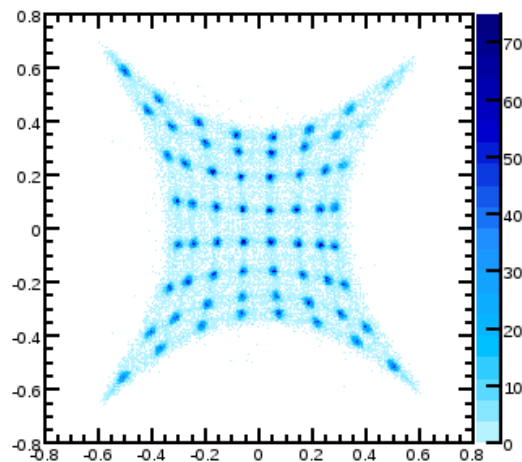


Figure 4.27: Flood histogram with 43pF explicit charge sharing capacitors

# Chapter 5

## Experiments with two cartridges

The hardware for two cartridges was built, assembled, and debugged. In these two cartridges, there was a total of 16 fins (i.e.,  $16 \times 16 = 256$  Dual-LYSO-PSAPD modules, or 32,768 scintillation crystal pixels), 16 Pitch Adapters, 2 HV Bias Boards, 8 RENA Boards, and 16 Discrete Boards (refer to Table 3.1). Photographs of the two cartridges are in Figures 5.1, 5.2, and 5.3.

The objects connected to plastic pipes next to the fins are fans. In the final system, water cooling will be implemented to thermally regulate the detectors. As a temporary solution, fans were used to draw warm air away from the heat sink attached to the fins. The plastic pipes were necessary to keep the fans further away from the detectors and electronics to reduce electromagnetic interference from the motors in the fans.

After an initial debugging period where the functionality of the system was established, measurements were taken to characterize the spatial resolution, energy resolution, and time resolution of this two cartridge system (Reynolds et al., 2012). Two experimental setups were used. In the first setup, a Sodium-22 (Na-22) point source was placed on a translation stage between the the two detector panels. In the second setup, an imaging phantom filled with FDG was placed between the detector panels.

A picture of the setup with the translation stage is in Figure 5.4. The detector panels were positioned 3.8cm apart and a Na22 point source with an activity of

$^{46}\text{uCi}$  and a source diameter of 0.25 mm, enclosed in a plastic disk, was placed on the translation stage, mid-way between the panels. Annihilation photons interacted with the detectors in the edge-on configuration. Movement of the translation stage was controlled by the data acquisition software. The bias voltage of the detector modules was set individually to its optimal value using the programmable HV distribution (Section 3.3).

Three experiments were performed with this translation stage setup: 1) the Na22 source was stepped across the detector panels with a 10.3mm step-size to measure energy and time resolution and the reconstructed point sources, 2) the Na22 source was placed in the center of the detector panels to measure sensitivity, and 3) the Na22 source was translated in front of a module pair with a 0.1mm step-size to measure point spread function (PSF). These measurements were performed with the temperature regulation set to  $27 \pm 1^\circ\text{C}$ . The following sections will describe these experiments and the results.

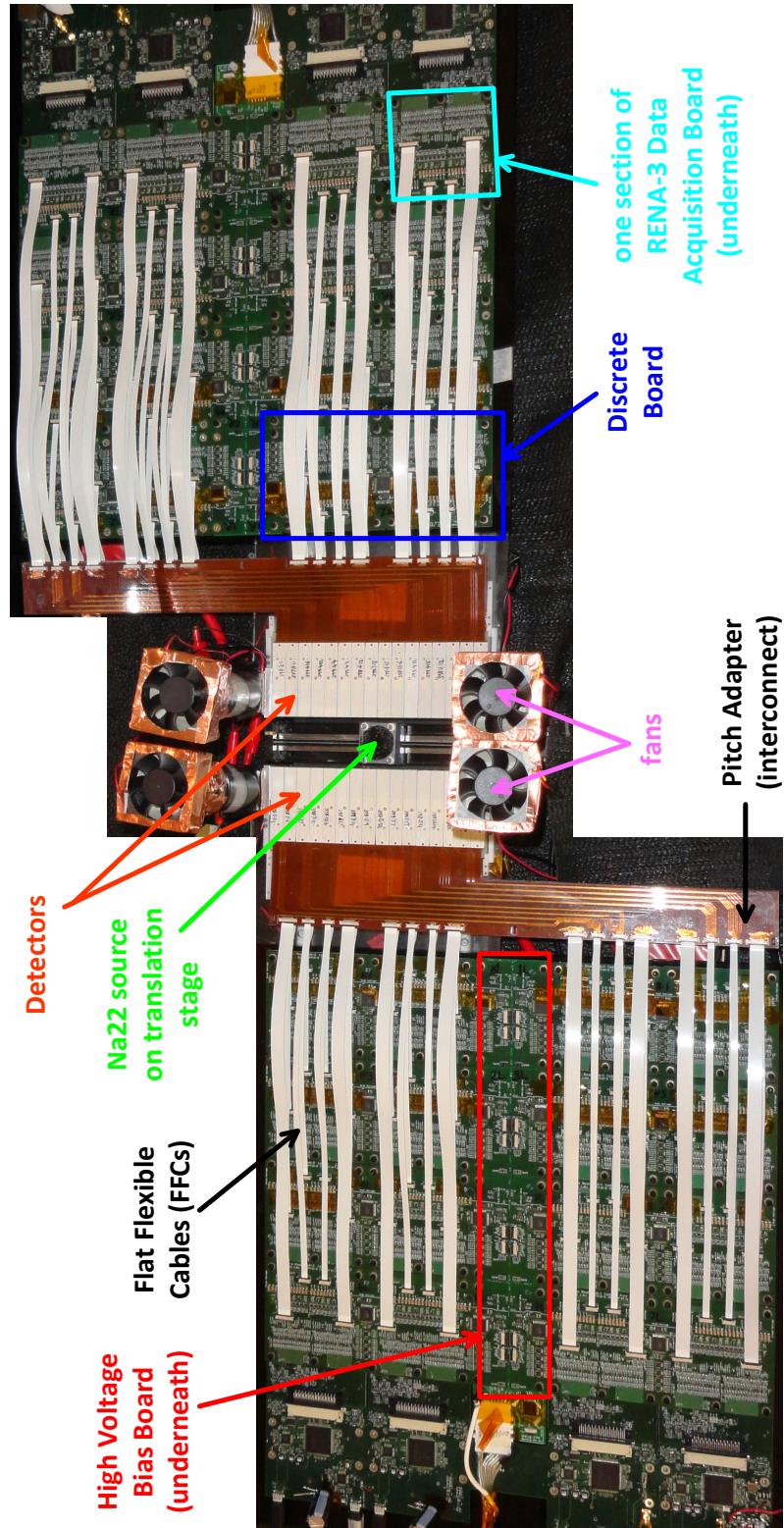


Figure 5.1: Picture of cartridge — top view.



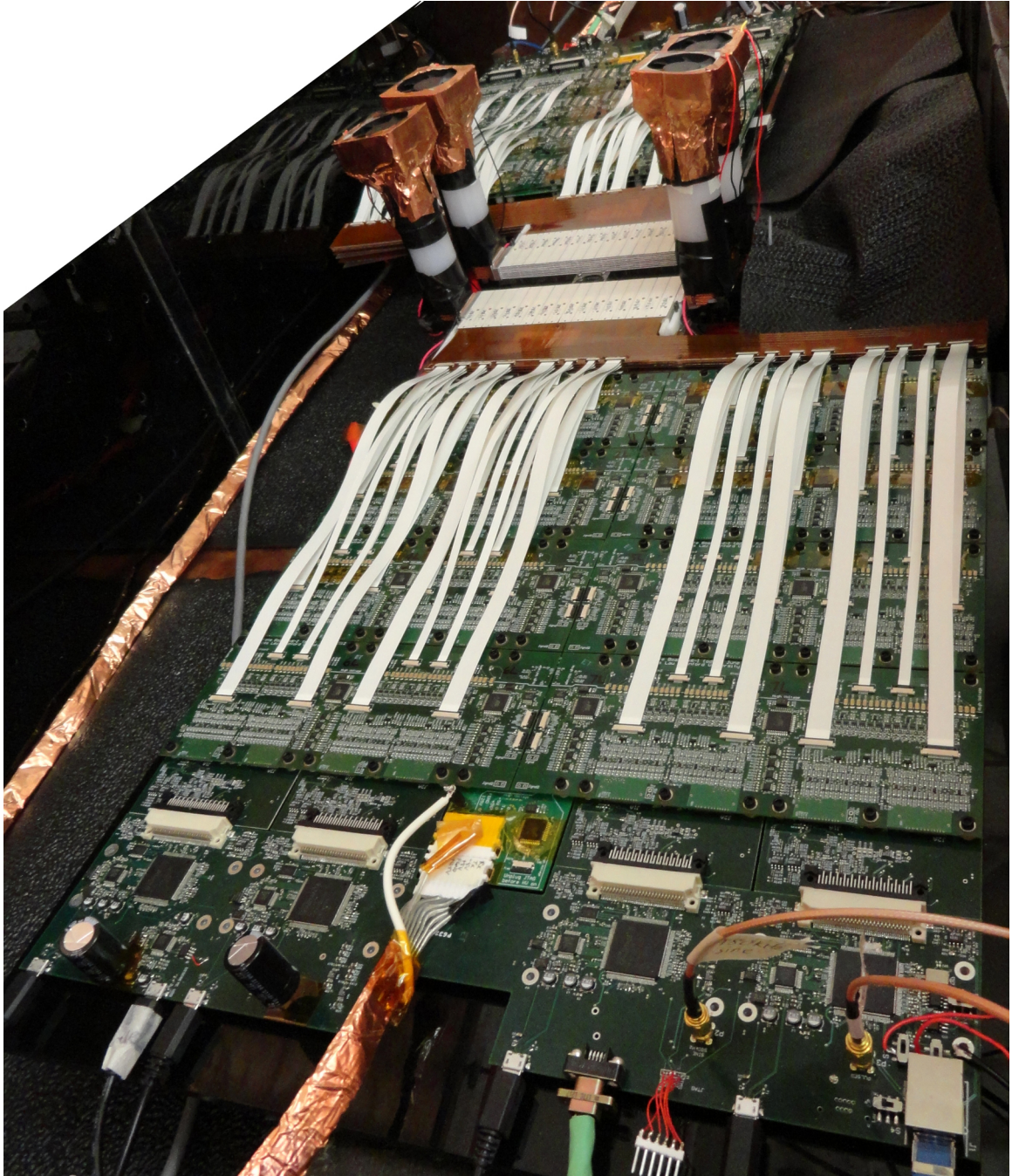


Figure 5.2: Picture of cartridge — end view.





Figure 5.3: Close-up picture of the stack of detectors.

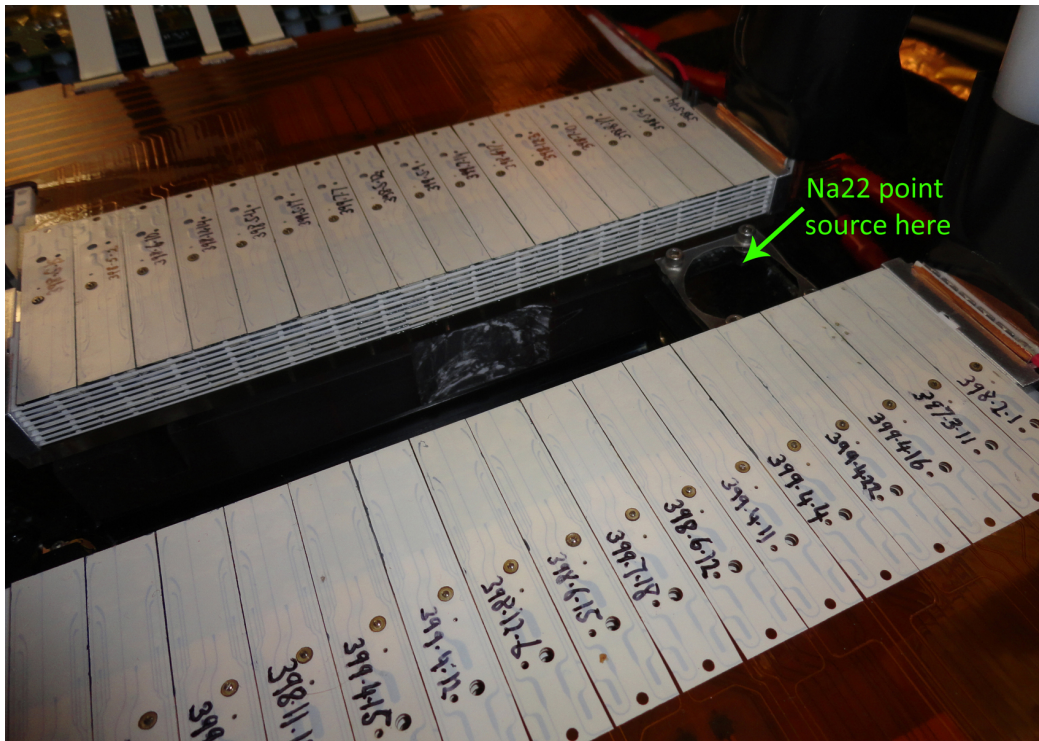


Figure 5.4: Experimental setup with translation stage. The Na22 source was placed on the source holder on the translation stage.

## 5.1 Stepped point source measurements

The detector panels were setup 3.8cm apart and the Na22 point source was placed mid-way between the two detector panels. Since the detector modules are placed side-by-side in a fin with a 10.3mm pitch, the Na22 point source was translated with 10.3mm steps, and data acquired at each step, so that data would be collected once in front of each detector module pair, as illustrated in Figure 5.5. Since the translation stage itself is 138mm long, we were able to collect data at 13 positions spaced 10.3mm apart. The data from all 13 positions was accumulated together. This experiment was repeated three times on three different days to determine the stability of the system and the systematic error in the measurements. Results from all three datasets are in Table 5.1. The following sub-sections contains explanations of the methods by which the results were obtained and figures for the results from first day of experiment (Dataset 1).

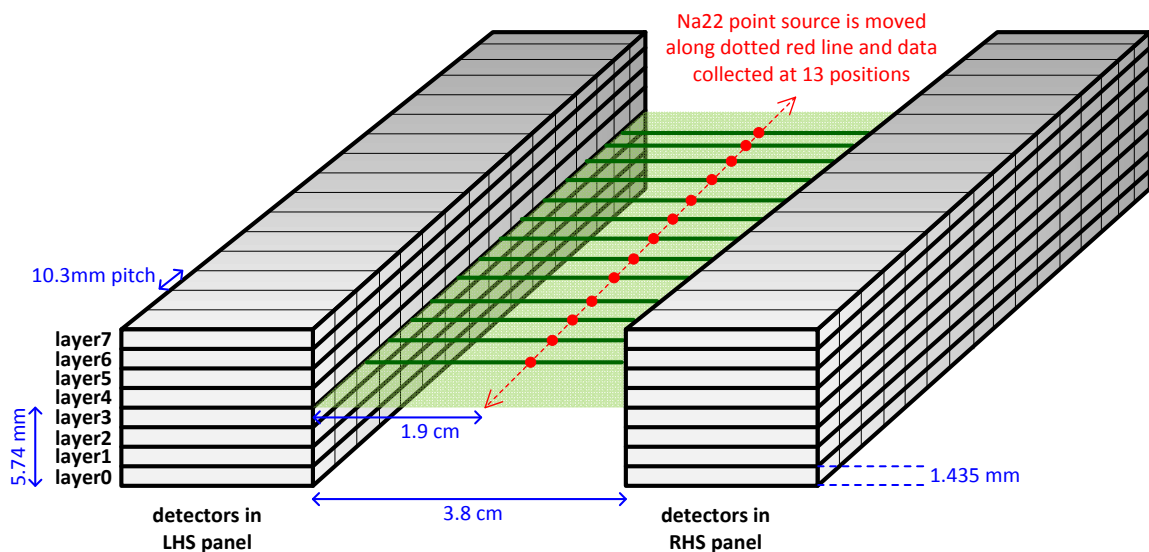


Figure 5.5: Stepped point source experiment setup. The Na22 point source was stepped across the panels with a 10.3mm step-size. Vertically, the point source was placed in the center of the detector panels, i.e., between layer 3 and layer 4.

Table 5.1: Stepped point source experiment results

	<b>Dataset 1</b>	<b>Dataset 2</b>	<b>Dataset 3</b>
<b>System Energy Resolution (FWHM)</b>	11.01±0.04%	10.70±0.04%	11.41±0.05%
<b>System Time Resolution (before calibration)</b>	109.3ns	104.0ns	109.0ns
<b>System Time Resolution (after calibration)</b>	24.3ns	21.2ns	25.3ns
<b>Sensitivity</b>	2.7%	2.7%	2.6%
<b>FBP Avg FWHM of Peaks</b>	0.70±0.04 mm	0.74±0.07 mm	0.69±0.03 mm
<b>FBP FWHM for Individual Peaks</b>	0.682±0.004 mm	0.673±0.004 mm	0.646±0.003 mm
	0.714±0.004 mm	0.703±0.004 mm	0.690±0.004 mm
	0.719±0.004 mm	0.811±0.005 mm	0.692±0.003 mm
	0.708±0.003 mm	0.784±0.005 mm	0.705±0.003 mm
	0.729±0.004 mm	0.758±0.004 mm	0.720±0.003 mm
	0.658±0.002 mm	0.804±0.005 mm	0.671±0.003 mm
	0.757±0.004 mm	0.815±0.005 mm	0.728±0.003 mm
	0.742±0.004 mm	0.816±0.006 mm	0.700±0.003 mm
	0.700±0.004 mm	0.705±0.004 mm	0.692±0.003 mm
	0.689±0.004 mm	0.615±0.003 mm	0.681±0.004 mm
	0.604±0.003 mm	0.645±0.004 mm	0.622±0.003 mm

### 5.1.1 Energy resolution

The energy spectrum for each detector module was corrected for per-crystal gain differences using the procedure described in Section 2.2.2. Then, the data from all the detector modules and from all 13 positions was aggregated together to obtain the system energy spectrum. To measure the system energy resolution, a double-Gaussian plus an exponential was fit to the photopeak. The double-Gaussian allowed the effects of x-ray escape to be included and the exponential captured the tail from the Compton peak and back-scatter peak. The same sigma was used for both Gaussian fits. The FWHM of the Gaussian for the 511keV photopeak divided by the mean of that Gaussian was reported as the global energy resolution. The error bar reported is the error in the fit at a confidence interval of 68%. The energy spectrum for Dataset 1 is shown in Figure 5.6.

The energy resolution was also determined for each PSAPD individually. A double-Gaussian-plus-exponential fit was also used in this case to determine the FWHM. A histogram of the per-PSAPD energy resolution was plotted, as shown

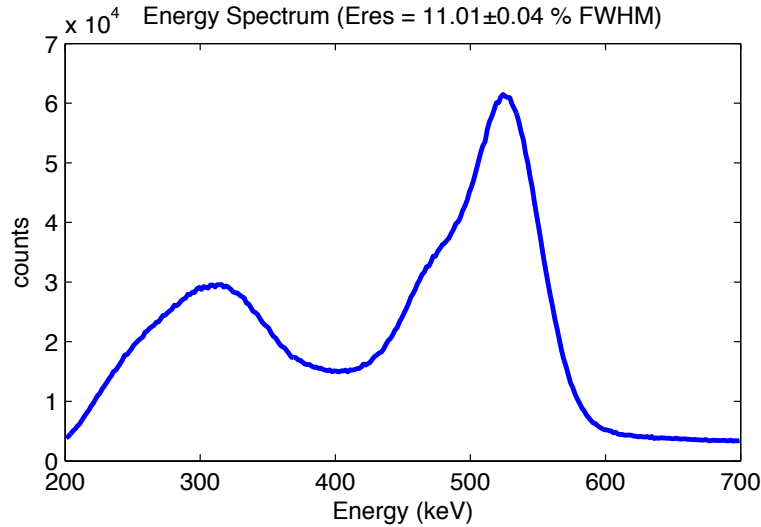


Figure 5.6: System energy spectrum for Dataset 1, showing  $11.01 \pm 0.04\%$  FWHM energy resolution.

in Figure 5.7. The mean energy resolution was  $11.2\%$  and the standard deviation was  $2.3\%$ . Aside from some outliers, most of the modules had an energy resolution clustered around  $11.2\%$ . To double-check if this distribution varied among fins, a per-PSAPD energy resolution histogram was plotted for each fin, as shown in Figure 5.8. There was no systematic difference between the various fins.

### 5.1.2 Time resolution

To correct for per-crystal offset and time walk effects in the system time resolution, a convex optimization algorithm (Reynolds et al., 2010b) was used. Work on improving this correction method is ongoing. The data in this thesis used a preliminary version of the algorithm where the convex optimization was performed on an average PSAPD to obtain the calibration parameters, and these calibration parameters were applied to all the PSAPDs.

Figure 5.9 shows the histogram of the time difference before and after calibration for Dataset 1. A Gaussian fit was used to determine that the time resolution was  $109.3 \pm 0.7$  ns FWHM before calibration ( $77.3 \pm 0.4$  ns FWHM unpaired) and  $24.10 \pm 0.03$  ns FWHM after calibration ( $17.04 \pm 0.02$  ns FWHM unpaired). The error

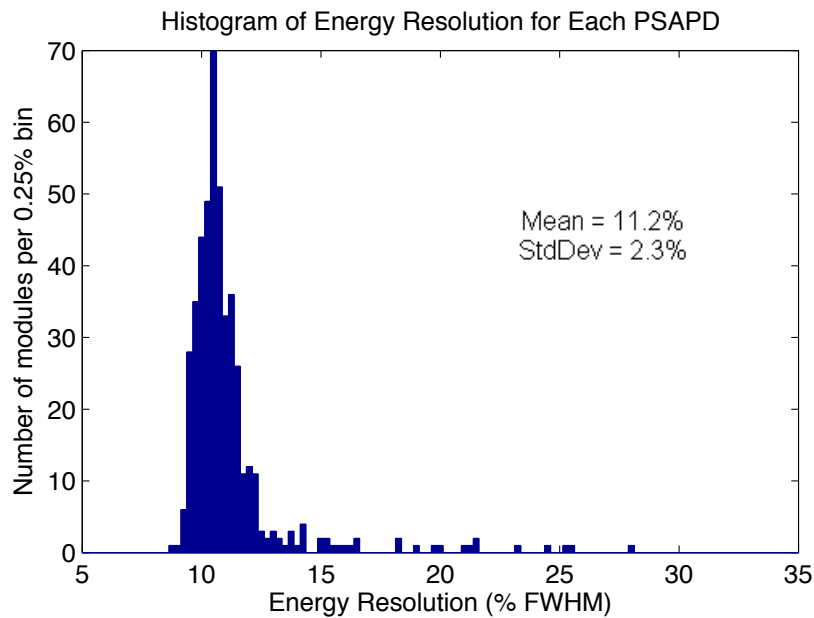
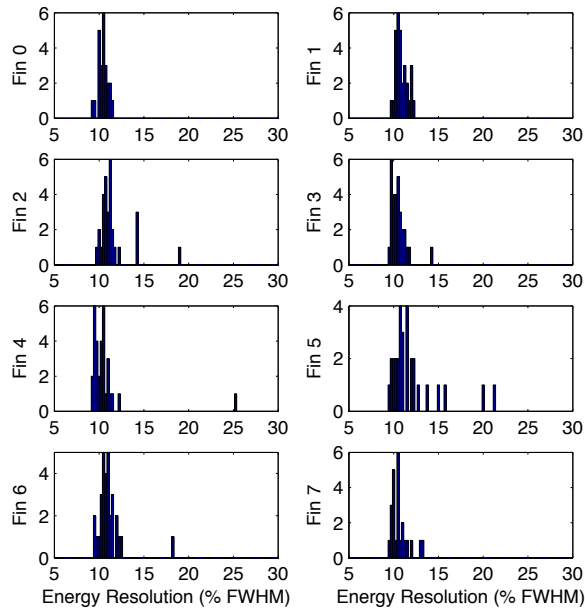


Figure 5.7: Per-PSAPD energy resolution for Dataset 1

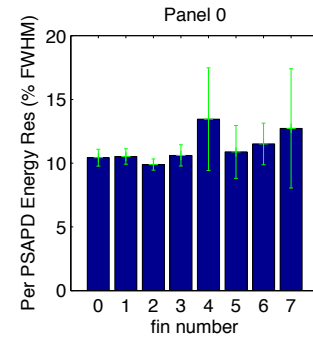
bar reported was the error in the fit at a confidence interval of 68%.

The system time resolution improved significantly with this calibration, although it was still not as low as the 7 ns FWHM previously obtained with two detectors (Reynolds et al., 2010b). This is because with the preliminary correction algorithm, the same calibration parameters were applied to all the PSAPDs. Work on developing methods to improve the system time resolution is ongoing.

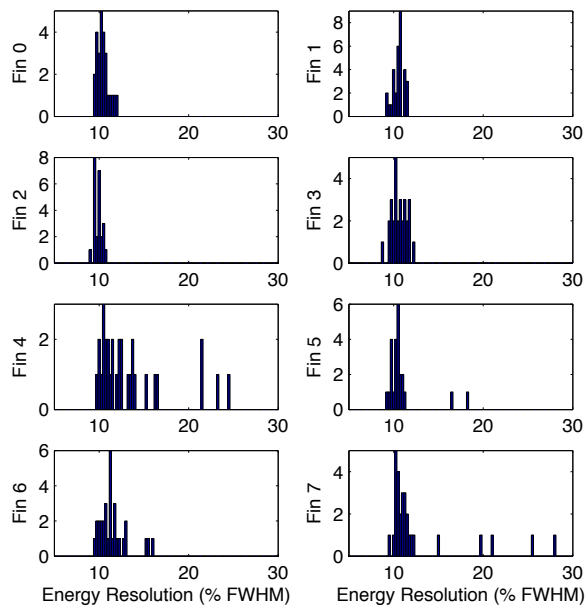
We wanted to determine if the system time resolution was biased by a few particularly good or bad detectors. The preliminary system-wide timing calibration was applied to the aggregated data from all 13 point source positions. Then, for each PSAPD in one panel, the time resolution was measured between that PSAPD and all the PSAPDs on the opposing panel. A histogram of the per-PSAPD time resolution was plotted, as shown in Figure 5.10. The mean time resolution was 24.6ns and the standard deviation was 5.6ns.



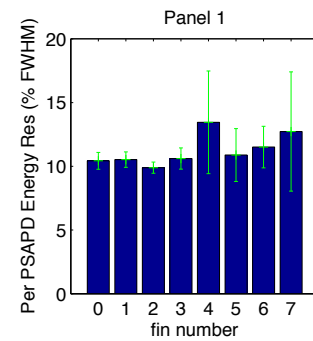
a) Panel 0: Histogram of per-PSAPD energy resolution, for each fin



b) Panel 0: Mean per-PSAPD energy resolution for each fin



c) Panel 1: Histogram of per-PSAPD energy resolution, for each fin



d) Panel 1: Mean per-PSAPD energy resolution for each fin

Figure 5.8: Per-PSAPD energy resolution for Dataset 1, for each fin

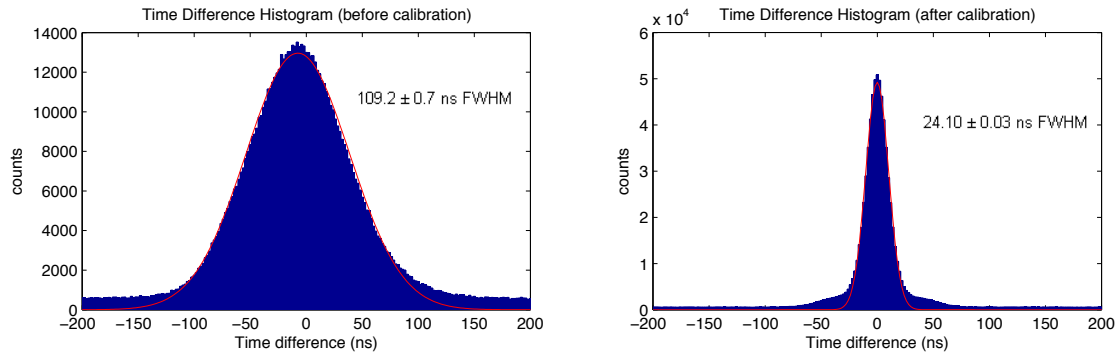


Figure 5.9: Time difference histograms for Dataset 1. Before calibration, the system time resolution was  $109.3 \pm 0.7$  ns FWHM. After our preliminary calibration algorithm, it improved to  $24.3 \pm 0.03$  ns FWHM.

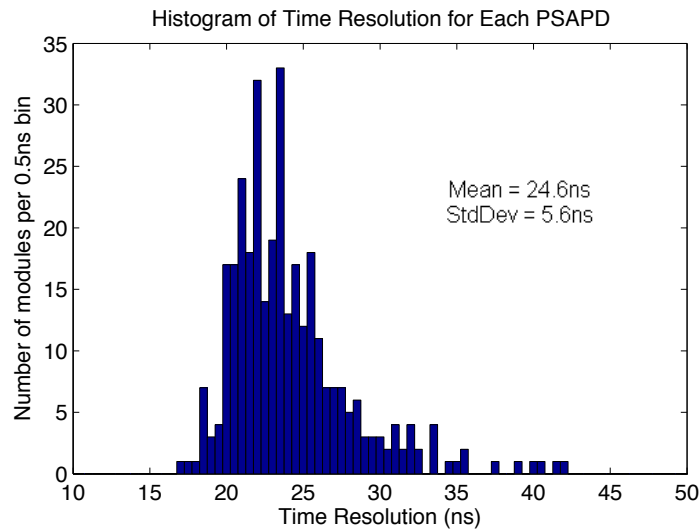


Figure 5.10: Per-PSAPD time resolution for Dataset 1



### 5.1.3 Filtered back projection reconstruction

The data from all 13 positions of the point source was accumulated together, so the reconstructed image appeared as if there were 13 point sources, spaced 10.3mm apart.

To obtain a reconstructed image of the point source as it was translated across the panels with 10.3mm steps, first, an energy window of  $\pm 20\%$  of 511keV and a time window of  $\pm 20$ ns was used to gate the data. Then, Filtered Back Projection, as implemented by the ‘iradon’ inverse Radon transform function in Matlab, was used for reconstruction. A cross-sectional profile through the center of the reconstructed image was created, and a Gaussian was fit to the reconstructed point sources. The FWHM of the Gaussian fit was reported. Since there were insufficient lines of response passing through the left-most and right-most source positions, the reconstructed point sources was not Gaussian in shape, and so those positions were excluded from the FWHM calculations. That’s why 11 values are reported in Table 5.1 for the FWHM even though data was collected at 13 positions. The error bar reported for the FWHM for the 11 individual peaks is the error in the fit at a confidence interval of 68%. The average FWHM of these middle 11 peaks is also reported, and in this case, the error bar is the standard deviation of the data used to compute the average.

Figure 5.11 shows the reconstructed image for Dataset 1 as well as a profile through the center of that image. The average FWHM of the middle 11 peaks is  $0.70 \pm 0.04$  mm.

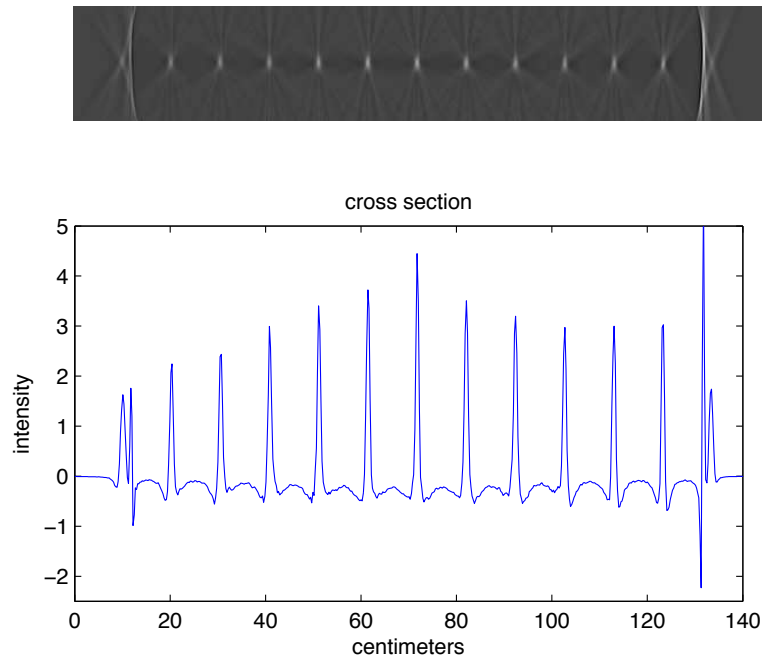


Figure 5.11: Filtered back projection image for Dataset 1 (top) and cross-sectional profile through the center (bottom). The left-most and right-most peaks do not appear Gaussian in shape due to insufficient lines of response at the edges of the detector panels. The FWHM of the peaks in the profile (excluding the left-most and right-most peaks) are listed in Table 5.1, and the average is  $0.70 \pm 0.04$  mm.

## 5.2 Sensitivity measurements

The two detector panels were placed 3.8cm apart, and the sensitivity of the two cartridge system was measured at the center of the FOV, as shown in Figure 5.12. A Na22 point source with an activity of 46uCi and a diameter of 0.25mm was placed in the center of the FOV.

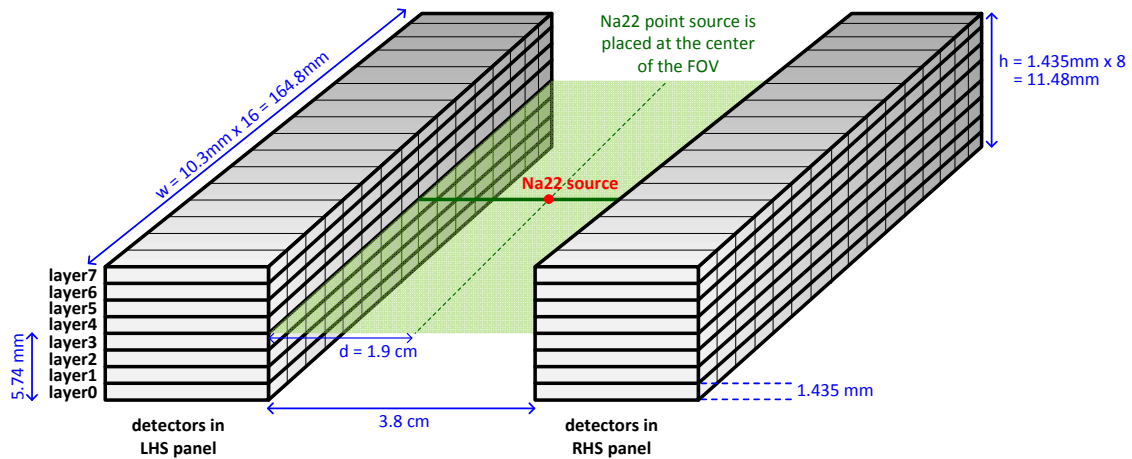


Figure 5.12: The Na22 point source was placed in the center of the FOV, mid-way between the detector panels. Vertically, the point source was placed in the center of the detector panels, i.e., between layer 3 and layer 4.

Five million counts were captured and the amount of time required to acquire those counts was recorded, and used to compute the count rate. To translate the count rate into a number for absolute sensitivity, the percentage of emitted photons which were detected was computed. 1 Curie (Ci) equals  $3.7 \times 10^{10}$  Bq, where 1 Bq (Becquerel) is a unit of radioactive decay equal to one disintegration per second. Therefore, 46uCi equals 1,702,000 disintegrations per second. 90% of disintegrations of Na22 produce a 511keV photon pair (Johns and Cunningham, 1978), so that is 1,531,800 511keV photon pairs per second. The count rate measured is divided by 1,531,800 and multiplied by 100 to calculate the percentage of emitted photons captured, reported in Table 5.1.

The sensitivity ranged from 2.6% to 2.7% for the three datasets. To check if this

result was reasonable, the solid angle of the detector panels in the two cartridge setup was calculated. Using the formula for the solid angle of a rectangular pyramid with apex at the origin (van Oosterom and Strackee, 1983; Gossman et al., 2011), where  $w = 10.3\text{mm} \times 16 = 164.8\text{mm}$  is the width of the detector panel,  $h = 1.435\text{mm} \times 8 = 11.48\text{mm}$  is the height of the detector panel, and  $d = 19.5\text{mm}$  is the perpendicular distance to the Na22 source, the solid angle  $\Omega$ , in units of  $\pi$  radians, was:

$$\begin{aligned}\Omega &= 4 \sin^{-1} \frac{wh}{\sqrt{(w^2 + 4d^2)(h^2 + 4d^2)}} \\ &= 4 \sin^{-1} \frac{164.8 \times 11.48}{\sqrt{(164.8^2 + 4(19.5)^2)(11.48^2 + 4(19.5)^2)}} \\ &= 1.11\end{aligned}\tag{5.1}$$

The upper limit on the sensitivity due to the solid angle subtended by the detector panels was then:

$$\begin{aligned}\text{sensitivity upper limit} &= 100 \frac{\Omega}{4\pi} \\ &= 8.9\%\end{aligned}\tag{5.2}$$

Thus, the two cartridge system captured and processed about  $2.65/8.9 = 30\%$  of all annihilation photons intersecting with the detector panels. Some annihilation photons may not have been captured because of the imperfect packing fraction of the crystals due to gaps between adjacent detector modules (see Figure 5.3). It was also possible that some of the photons intersected with the detector panels at an angle such that the detector thickness was insufficient to stop the photon. The solid angle of the detector panel will increase (by Equation 5.1) as more cartridges are constructed and stacked to form the full system.

### 5.3 Point Spread Function (PSF) measurements

The point spread function of a PET system characterizes the spatial resolution. To produce the point spread function, a point source was stepped across the detectors using a translational stage in 0.1mm steps. An energy window of  $\pm 20\%$  of 511keV and a time window of  $\pm 20$ ns was used to gate the data. Instead of using a lead collimator, collimation was done electronically by plotting a histogram of the events detected at each scan step for each parallel line coincident set of crystals (i.e, from columns of directly opposing crystals), as shown in Figure 5.13. All the coincidence counts registered to the columns of directly opposing crystals were interpreted by the system to be from the same line of response. The width of the histogram represents the physical space over which the annihilation originated and could not be differentiated by the system. This histogram, with the actual source position as the x-axis, is called a point spread function, and indicates the spatial resolution.

Ignoring noise, a pair of rectangular detectors produces a triangular-shaped point spread function at the center between the two detectors with a FWHM that is approximately 50% of the detector width (Yamashita, 1992). With blurring effects such as charge sharing and inter-crystal scatter, the point spread function appears Gaussian. So, a Gaussian was fit to the peaks and the average FWHM of the Gaussians was reported, representing the intrinsic spatial resolution. The error bar was the standard deviation of the data used to compute the average.

The PSF was measured for two sets of opposing detectors modules, one set near the center of the FOV and one set at the edge of the FOV. In both sets, detector modules on layer 4 were chosen. The PSF was normalized so that the number of events in each crystal pairing would be the same.

Without de-convolving effects of the 0.25 mm point source, the average FWHM was  $0.84 \pm 0.02$ mm for the module near the center (Figure 5.14) and  $0.93 \pm 0.17$ mm for the module near the edge (Figure 5.15). Extra crystal columns from adjacent modules were included to show the detector pitch. In Figure 5.15, for the module at the edge, there is only one extra crystal column since there is an adjacent module on only one side. These extra crystal columns were not included in the calculation of

the average FWHM.

As seen in Figure 5.15, the FWHM was larger for the two crystal columns near the edge of the FOV. This may be due to scattering of annihilation photons on the aluminum side-walls used to hold the fins of detectors in place. When the source was slightly outside the FOV, events were still being registered as interacting in the crystal columns closest to the edge, so this may be due to scatter. It may be possible to reject these events in the future if the energy resolution is improved.

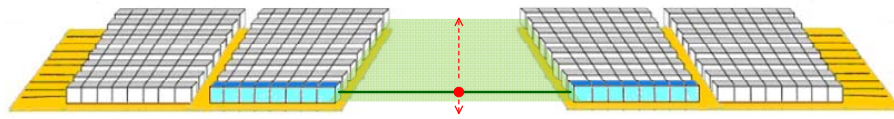


Figure 5.13: The Point Spread Function histogram is formed by creating a histogram of events recorded in each set of opposing crystal columns as a function of source position.

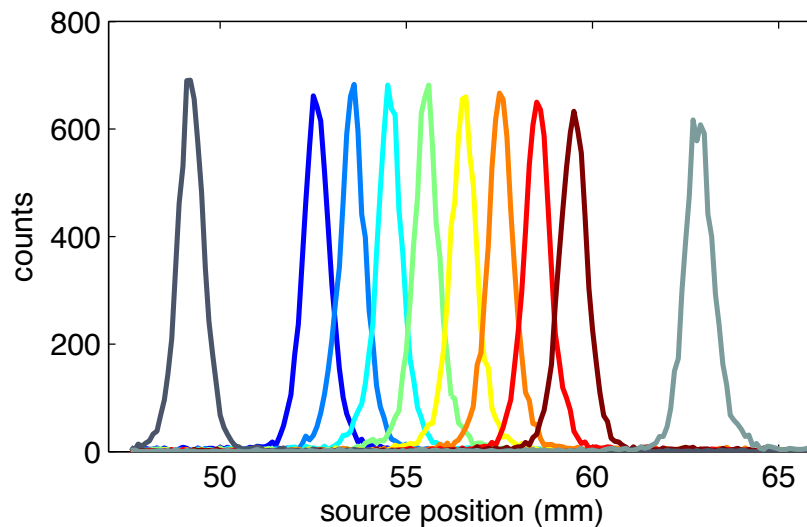


Figure 5.14: Point spread function for a detector module near the center of the FOV. The average FWHM was  $0.84 \pm 0.02$  mm.

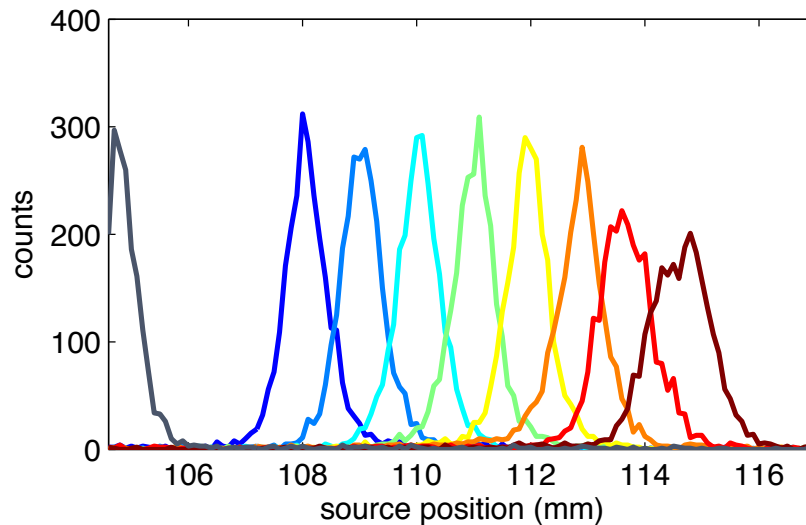


Figure 5.15: Point spread function for a detector module at the edge of the FOV. The average FWHM was  $0.93 \pm 0.17$  mm.

## 5.4 Acquisition and image reconstruction of phantom data

To further validate the performance of the two cartridge system, two phantoms were imaged. The Micro Deluxe Phantom from Data Spectrum Corporation was placed between detector panels positioned 5.8 cm apart (Figure 5.16). This phantom has two removable inserts — a hot rod insert and a cold rod insert. The hot rod insert has plastic cylindrical tubes which can be filled with FDG, testing the ability of the system to image lesions with radioactivity inside. The cold rod insert has solid plastic cylinders so that the surrounding volume can be filled with FDG, testing the ability of the system to image structures without radioactivity in a background with radioactivity. Three datasets were acquired using this setup: 1) normalization dataset, 2) hot rod dataset, and 3) cold rod dataset.

A normalization dataset was acquired to calibrate for differences in detection efficiency across the FOV. For this normalization, the phantom cylinder was used without any inserts, and the entire cylinder (diameter 4.5 cm) was filled with  $51 \mu\text{Ci}$  of FDG (volume was 27 mL, filled to height of about 1.7 cm). 2.3 million counts were

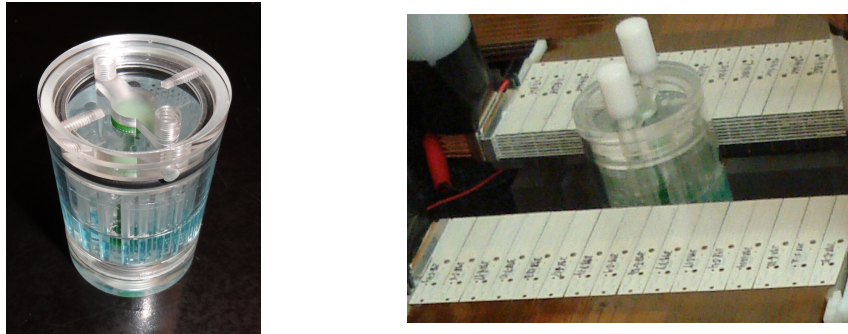


Figure 5.16: Left: Phantom. Right: Phantom placed between detector panels with panel separation of 5.8cm.

acquired. Using the maximum likelihood expectation maximization (MLEM) reconstruction algorithm (Dempster et al., 1977), (Wernick and Aarsvold, 2004, Chapter 21), implemented by running one subset of the algorithm implemented by Cui et al. (2011), the normalization image produced is shown in Figure 5.17. The phantom had FDG uniformly distributed in the entire 4.5 cm diameter, so the variations in intensity seen in the image are due to detection efficiency. An inverse of this image was used to normalize the subsequent datasets.

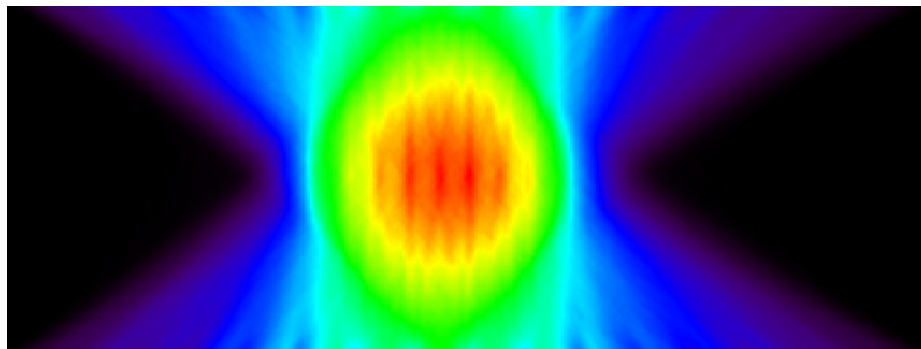


Figure 5.17: Reconstructed phantom normalization image

Next, the hot rod insert was placed inside the phantom cylinder. The rods in the insert had diameters of 1.2, 1.6, 2.4, 3.2, 4.0 and 4.8 mm and the center-to center spacing was two times the diameter of the rods. These rods were filled with  $140\mu\text{Ci}$  of



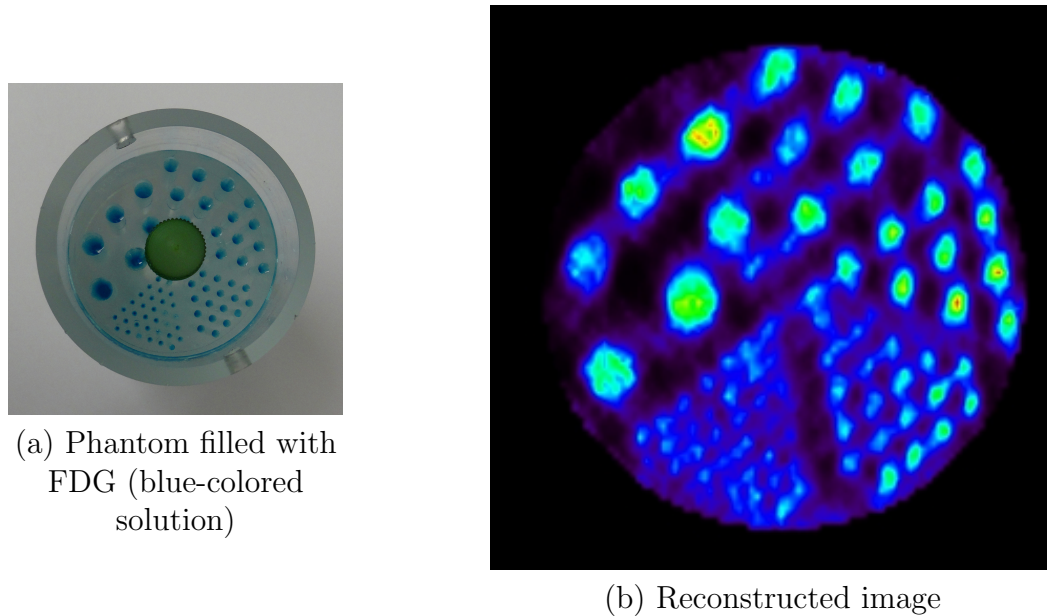


Figure 5.18: Phantom with hot rods filled with FDG and reconstructed image after randoms removal and normalization

FDG (volume was 4.1mL). To make it easier to identify air bubbles, blue food coloring was added to the FDG solution. Due to the limited count rate in the preliminary backend electronics (see Section 3.4) and active height (11.48mm) of the system at this time, the rods were filled to a height of about 17mm to reduce the number of singles.

1.2 million counts were acquired, of which 286,000 were randoms. The delayed window randoms removal method (Wernick and Aarsvold, 2004, Chap. 10) was used to reject these randoms to improve the image contrast. Then, normalization was done. The MLEM reconstructed image is shown in Figure 5.18. Most of the 1.2mm rods were resolvable.

Finally, the cold rod insert was placed inside the phantom cylinder. The rods were solid plastic with diameters of 1.2, 1.6, 2.4, 3.2, 4.0 and 4.8 mm and center-to-center spacing two times the diameter of the rods. The phantom was filled with  $48\mu\text{Ci}$  of FDG (volume was 17mL, with blue food coloring), so the entire 4.5cm diameter

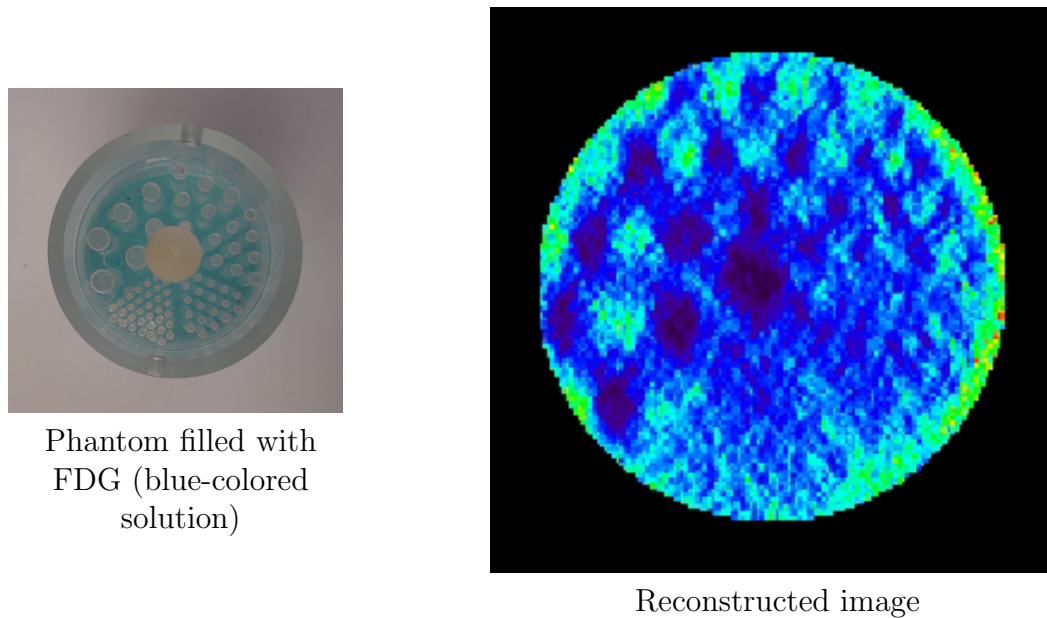


Figure 5.19: Phantom with cold rods and reconstructed image after randoms removal and normalization

cylinder was filled with FDG except for the cold rods.

3.3 million counts were acquired, of which 200,000 were randoms. The delayed window randoms removal method was used to reject these randoms to improve the image contrast, and normalization was done. The MLEM reconstructed image is shown in Figure 5.19.

The contrast, reconstructed SNR, and resolution of the cold rod image was not as good as the hot rod image. The first reason is because an insufficient number of counts was acquired. A larger volume of radioactive liquid was necessary to fill the cold rod phantom (17mL for cold rod phantom, versus 4.1mL for hot rod phantom), and we could not keep the concentration of FDG as high as it was with the hot rod phantom due to the count rate limitation of the existing system (due to the preliminary backend electronics, see Section 3.4). In fact, in this experiment, the activity in the cold rod experiment ( $48\mu\text{Ci}$ ) ended up being even lower than the activity in the hot rod experiment ( $140\mu\text{Ci}$ ) due to difficulties in measuring exact

amounts of radioactivity immediately before performing experiments (because of the short half life of FDG). With this lower FDG concentration, we could only collect 3.3 million counts before the FDG decayed, which was not sufficient. In the future, after the count rate of the system is improved, the cold rod experiment can be repeated with a higher concentration of radioactivity. Since the activity-to-background ratio was lower for the cold rods, the cold rod phantom image was also more sensitive to inaccuracies in normalization.

Secondly, the randoms rate was high due to the limited active height (11.48mm) of the detectors, and the delayed window randoms removal method was noisy, so applying the noisy correction to the noisy dataset propagated noise. The image should also improve in the future as the number of stacked detector layers increases.

## 5.5 Conclusions from two cartridge experiments

The two cartridge system was characterized with Na22 point source and phantom experiments. The results from the experiments with the Na22 point source were quite consistent over the three days, showing uniformity in the system performance. The system energy resolution only differed by 0.7% (absolute difference), the system time resolution only differed by 4.1ns, and the sensitivity only differed by 0.1% (absolute difference). The point spread function experiment showed that the system has an intrinsic resolution of about 0.8-0.9mm. The system was able to image phantoms and 1.2mm rods filled with FDG could be resolved.

# Chapter 6

## Conclusion

Two cartridges of the breast-dedicated PET system were designed, built, and characterized. The intrinsic resolution was 0.8-0.9mm, the system energy resolution was about 11% FWHM, and the time resolution was 21-25 ns FWHM. Phantoms were imaged and 1.2mm rods filled with FDG could be resolved. The next step is to build 16 more cartridges in order to complete the two full panels for the final system. The entire chain of detectors, interconnect, and data acquisition electronics planned for the final system were used in the two cartridge experiments shown in this thesis, so the results should be good predictors of the final system performance.

There are many challenges in designing a high resolution breast-dedicated PET system with PSAPDs. For high resolution, the PSAPDs need to be packed tightly together and interconnect to the PSAPDs needs to handle the low voltage signals as well as the -1750V bias voltages. This thesis described a design which achieves these goals using PSAPDs mounted on a thin flexible circuits, Pitch Adapters, and flat flexible cables (FFCs). Multiplexing of PSAPDs was done, reducing the density of the interconnect by 40% and the number of electronics channels by 33% without significant degradation in performance. The design achieves 1mm resolution in all three dimensions (with 1mm depth-of-interaction).

Biasing the PSAPDs was challenging because the magnitude of the required bias voltage is so high (1750V), the PSAPDs were tightly packed with potential paths for breakdown, and because each PSAPD had a slightly different optimal bias voltage due

to process and temperature differences. Section 3.3 described a solution to provide programmable bias voltages ranging from -1800V to -1700V by using a DAC with a 100V range referenced to -1800V.

Reading out the PSAPDs using the RENA-3 ASIC was not straightforward due to the mismatch in the signal dynamic ranges and the parasitic capacitances introduced by the interconnect. Charge division was implemented on the common terminal of the PSAPD (Section 3.5.1) and signal conditioning was implemented on the spatial channels (Section 4.3) to solve this problem.

Based on the experience of designing these first two cartridges of the breast-dedicated PET system, a number of observations and ideas for future improvements emerged. The current interconnect design is very compact, but it is time consuming to repair the system if detectors fail and need to be replaced after the cartridges have been stacked to form a panel. If a PSAPD fails and becomes an open circuit, then one line of response would be missing, but it is fine to leave that PSAPD in the system. However, if a PSAPD fails and becomes a low resistance path, then it is necessary to remove that PSAPD to prevent it from drawing too much current. In the future, investigation needs to determine the likelihood of PSAPD failure and, if necessary, how to modify the system to handle PSAPD failure.

The system time resolution was 21-25 ns FWHM, not as low as the 7 ns FWHM previously obtained with two detectors, because the calibration parameters were derived from an average PSAPD and then applied to all the PSAPDs. The other team members working on the breast-dedicated PET system are investigating how to improve the system time resolution.

The reconstructed SNR, contrast, and resolution of the two cartridge measurements were limited by the count rate of about 25,000 events/sec presently achieved with the prototype interface between the RENA-3 Board and the backend electronics and current data acquisition software (see Sections 3.4 and 5.4). Work is ongoing by the other team members to improve this count rate.

A big challenge of this project was the high bias voltage (1750V) of the PSAPDs. Although we were able to create a design that handles the high voltage, a future research direction could be to investigate ways to avoid using such high voltages. If the

bias voltage were lower, the system form factor could be smaller since we would be able to choose smaller components with lower voltage ratings. System development time could decrease since there will be less chance of accidental high voltage arcing and it will take less time to ramp up the bias voltage during experiments. Position Sensitive Solid-State Photomultipliers (PS-SSPMs) (McClish et al., 2010) are detectors that have shown promise to be useful in PET and only have a bias voltage of 30-80V.

Although the mismatch in the PSAPD and RENA-3 signal dynamic ranges was addressed by charge division and signal conditioning, there was SNR loss by doing this, so it would be better to avoid the problem altogether with front-end electronics that have a dynamic range that matches the input charge. In fact, another project is ongoing where a new integrated circuit for PET applications was designed (Lau et al., 2012a,b). This integrated circuit has an input dynamic range that can be adjusted to be suitable for PSAPDs (gain  $\sim 10^3$ ) as well as SiPM detectors (gain  $\sim 10^6$ ).

This breast-dedicated PET system uses the analog circuits in the RENA-3 for charge integration and time discrimination. As mentioned in Section 2.3.5, waveform digitization is another approach that is more flexible and could result in better time resolution. Waveform digitization is usually implemented using free-running ADCs. However, the digitized pulse waveform output from a free-running ADC is actually an inefficient representation of the signal. It is most important to finely sample the rising edge for good time resolution, but it is usually sampled coarsely, unless a very high sample rate is used. The falling edge, which is only used to compute the integral of the pulse for energy determination, can be coarsely sampled because the integration calculation suppresses noise, but it's usually finely sampled. Thus, using free-running ADCs for this problem is neither cost nor power efficient.

In the ongoing integrated circuit design project, an unconventional digitization method that takes better advantage of the characteristic form of scintillation pulse shapes in PET is proposed (Lau et al., 2012a,b). Instead of sampling at equal time intervals, sampling is done at user-defined voltage levels. This achieves fine sampling on the beginning of the fast rising edge and coarse sampling on the slower falling edge. This principle is also known as "level-crossing ADC", "time-based ADC", or

“threshold ADC”, and has been used in other applications (Sayiner et al., 1996; Kozmin et al., 2009).

This thesis contributes to the PET research field by demonstrating that it is possible to build a  $1\text{x}1\text{x}1\text{mm}^3$  resolution PET system with 3-D position sensitive detectors using LYSO, PSAPDs and the RENA-3 ASIC. This thesis also provides some insight on how to integrate over 2,300 detectors and 18,000 electronic channels to build an extremely complex system. Using this system, a clinical study can be performed to study whether a  $1\text{x}1\text{x}1\text{mm}^3$  resolution PET system can improve the detection, diagnosis, and monitoring of cancer. This system is also a useful research tool. Individuals developing image reconstruction and signal processing algorithms for PET can use data from this system to verify their algorithms. PET system designers can use building blocks from this system, such as the data acquisition hardware, detector modules, or software programs, in new PET system prototypes.

# Publication List

- F. W. Y. Lau, A. Vandenbroucke, P. D. Reynolds, H. Ho, D. Innes, and C. S. Levin. Signal conditioning technique for position sensitive photodetectors to manipulate pixelated crystal identification capabilities. *IEEE Transactions on Nuclear Science*, 59(5):1815–1822, 2012.
- F. W. Y. Lau, J.-Y. Yeom, A. Vandenbroucke, P. D. Reynolds, D. Innes, and C. S. Levin. A cost-effective modular programmable HV distribution system for photodetectors. In *IEEE Nuclear Science Symposium and Medical Imaging Conference*, pages 3504–3506, 2012.
- F. W. Y. Lau, H. H. Choi, M. A. Horowitz, and C. S. Levin. A new IC with level-crossing ADC readout architecture for PET detector signals. In *IEEE Nuclear Science Symposium and Medical Imaging Conference*, pages 2486–2488, 2012.
- F. W. Y. Lau, C. S. Levin, M. A. Horowitz, H. H. Choi, and J. Kim. Time-based digitizer for pet photodetector, 2012. Patent Application PCT/US2012/067800, Publication Number WO2013085923 A1.
- P. D. Reynolds, F. W. Y. Lau, A. Vandenbroucke, D. Innes, U. Yoruk, and C. S. Levin. Characterization of detector layers from a 1 mm<sup>3</sup> resolution clinical PET system. In *IEEE Nuclear Science Symposium and Medical Imaging Conference*, pages 3804–3807, 2012.
- F. W. Y. Lau, A. Vandenbroucke, P. D. Reynolds, H. Ho, D. Innes, and C. S. Levin. Signal conditioning technique for position sensitive photodetectors to manipulate



- pixelated crystal identification capabilities. In *IEEE Nuclear Science Symposium and Medical Imaging Conference*, pages 1647–1653, 2011.
- A. Vandenbroucke, F. W. Y. Lau, P. D. Reynolds, and C. S. Levin. Measuring 511 keV photon interaction locations in three dimensions using 3-d position sensitive scintillation detectors. In *IEEE Nuclear Science Symposium and Medical Imaging Conference*, pages 3635–3638, 2011.
- P. D. Reynolds, F. W. Y. Lau, A. Vandenbroucke, and C. S. Levin. Study of readout for groups of position sensitive avalanche photodiodes used in a 1 mm<sup>3</sup> resolution clinical PET system. In *IEEE Nuclear Science Symposium and Medical Imaging Conference*, pages 3253–3255, 2011.
- F. W. Y. Lau, A. Vandenbroucke, P. D. Reynolds, P. D. Olcott, M. A. Horowitz, and C. S. Levin. Analog signal multiplexing for PSAPD-based PET detectors: simulation and experimental validation. *Physics in Medicine and Biology*, 55(23): 7149–7174, 2010.
- P. D. Reynolds, P. D. Olcott, G. Prax, F. W. Y. Lau, and C. S. Levin. Convex optimization of coincidence time resolution for a high resolution PET system. *IEEE Transactions on Medical Imaging*, PP(99):1, 2010.
- P. D. Reynolds, F. W. Y. Lau, A. Vandenbroucke, and C. S. Levin. Readout design and validation for a 1 mm<sup>3</sup> resolution clinical PET system. In *IEEE Nuclear Science Symposium and Medical Imaging Conference*, pages 3097–3099, 2010.
- M. Horowitz, M. Jeeradit, F. Lau, S. Liao, B. Lim, and J. Mao. Fortifying analog models with equivalence checking and coverage analysis. In *Proceedings of the 47th Design Automation Conference*, pages 425–430, Anaheim, California, 2010. ACM.
- Y. Gu, G. Prax, F. W. Y. Lau, and C. S. Levin. Effects of multiple-interaction photon events in a high-resolution PET system that uses 3-d positioning detectors. *Medical Physics*, 37(10):5494, 2010.

- F. W. Y. Lau, A. Vandembroucke, P. Reynolds, P. Olcott, M. Horowitz, and C. S. Levin. Detector and front-end electronics for 1mm<sup>3</sup> resolution breast-dedicated PET system. *Society of Nuclear Medicine Annual Meeting Abstracts*, 50(2\_MeetingAbstracts):1525, May 2009.
- A. Vandembroucke, J. Lee, V. C. Spanoudaki, F. W. Y. Lau, P. D. Reynolds, and C. S. Levin. Temperature and bias voltage studies of a large area position sensitive avalanche photodiode. In *IEEE Nuclear Science Symposium and Medical Imaging Conference*, pages 3664–3669, 2009.
- A. Vandembroucke, A. M. K. Foudray, F. W. Y. Lau, P. D. Olcott, P. D. Reynolds, and C. S. Levin. Performance characterization of a new high resolution PET scintillation detector. In *IEEE Nuclear Science Symposium and Medical Imaging Conference*, pages 3604–3608, 2008.
- V. C. Spanoudaki, A. Vandembroucke, F. W. Y. Lau, C. Fang, and C. S. Levin. Effects of thermal regulation structures on the photon sensitivity and spatial resolution of a 1 mm<sup>3</sup> resolution breast-dedicated PET system. In *IEEE Nuclear Science Symposium and Medical Imaging Conference*, pages 5657–5661, 2008.
- P. D. Reynolds, P. D. Olcott, G. Pratz, F. W. Y. Lau, and C. S. Levin. Convex optimization of coincidence time resolution for high resolution PET systems. In *IEEE Nuclear Science Symposium and Medical Imaging Conference*, pages 4068–4073, 2008.
- F. W. Y. Lau, A. Vandembroucke, P. D. Reynolds, P. D. Olcott, M. A. Horowitz, and C. S. Levin. Front-end electronics for a 1 mm<sup>3</sup> resolution avalanche photodiode-based PET system with analog signal multiplexing. In *IEEE Nuclear Science Symposium and Medical Imaging Conference*, pages 3871–3874, 2008.
- F. W. Y. Lau, C. Fang, P. D. Reynolds, P. D. Olcott, A. Vandembroucke, V. C. Spanoudaki, F. Olutade, M. A. Horowitz, and C. S. Levin. 1mm<sup>3</sup> resolution breast-dedicated PET system. In *IEEE Nuclear Science Symposium and Medical Imaging Conference*, pages 5619–5622, 2008.

- Y. Gu, G. Pratz, F. W. Y. Lau, and C. S. Levin. Effects of multiple photon interactions in a high resolution PET system that uses 3-d positioning detectors. In *IEEE Nuclear Science Symposium and Medical Imaging Conference*, pages 3814–3819, 2008.
- P. D. Olcott, F. W. Y. Lau, and C. S. Levin. Data acquisition system design for a 1 mm<sup>3</sup> resolution PSAPD-based PET system. In *IEEE Nuclear Science Symposium Conference Record, 2007. NSS '07*, volume 5, pages 3206–3211, 2007.
- F. W. Y. Lau, P. D. Olcott, M. Horowitz, H. Peng, and C. S. Levin. Noise analysis of LSO-PSAPD PET detector front-end multiplexing circuits. In *Nuclear Science Symposium Conference Record, 2007. NSS '07. IEEE*, volume 5, pages 3212–3219, 2007.
- F. W. Y. Lau, P. D. Olcott, and C. S. Levin. Data acquisition system design for a 1mm<sup>3</sup> resolution PSAPD-based PET system, 2007.

# Bibliography

- M. C. Abreu, J. D. Aguiar, F. G. Almeida, P. Almeida, P. Bento, B. Carrico, M. Ferreira, N. C. Ferreira, F. Goncalves, C. Leong, F. Lopes, P. Lousa, M. V. Martins, N. Matela, P. R. Mendes, R. Moura, J. Nobre, N. Oliveira, C. Ortigao, L. Peralta, R. Pereira, J. Rego, R. Ribeiro, P. Rodrigues, J. Sampaio, A. I. Santos, L. Silva, J. C. Silva, P. Sousa, I. C. Teixeira, J. P. Teixeira, A. Trindade, and J. Varela. Design and evaluation of the clear-PEM scanner for positron emission mammography. *IEEE Transactions on Nuclear Science*, 53(1):71–77, 2006.
- H. O. Anger. Scintillation camera. *Review of Scientific Instruments*, 29(1):27–33, January 1958.
- R. Brun and F. Rademakers. ROOT – an object oriented data analysis framework. *Nuclear Instruments Methods Physics Research A*, 389(1-2):81–86, April 1997.
- F. Cayouette, D. Laurendeau, and C. Moisan. DETECT2000: an improved monte-carlo simulator for the computer aided design of photon sensing devices. *Proceedings of SPIE*, 4833(1):69–76, February 2003.
- S. Cho, R. Grazioso, N. Zhang, M. Aykac, and M. Schmand. Digital timing: sampling frequency, anti-aliasing filter and signal interpolation filter dependence on timing resolution. *Physics in Medicine and Biology*, 56(23):7569–7583, December 2011.
- J.-Y. Cui, G. Prax, S. Prevrhal, and C. S. Levin. Fully 3D list-mode time-of-flight PET image reconstruction on GPUs using CUDA. *Medical Physics*, 38(12):6775–6786, December 2011.

- A. P. Dempster, N. M. Laird, and D. B. Rubin. Maximum likelihood from incomplete data via the EM algorithm. *Journal of the Royal Statistical Society, Series B*, 39(1):1–38, January 1977.
- P. Dokhale, R. W. Silverman, K. S. Shah, R. Grazioso, R. Farrell, J. Glodo, M. McClish, G. Entine, V.-H. Tran, and S. R. Cherry. Performance measurements of a depth-encoding PET detector module based on position-sensitive avalanche photodiode read-out. *Physics in Medicine and Biology*, 49(18):4293–4304, September 2004.
- N. K. Doshi, R. W. Silverman, Y. Shao, and S. R. Cherry. maxPET, a dedicated mammary and axillary region PET imaging system for breast cancer. *IEEE Transactions on Nuclear Science*, 48(3):811–815, 2001.
- P. Elmer. Avalanche photodiode: A user guide, 2010. URL [www.optoelectronics.perkinelmer.com](http://www.optoelectronics.perkinelmer.com).
- S. Fanti, M. Farsad, and L. Mansi. *Atlas of PET-CT: A Quick Guide to Image Interpretation*. Springer, 2009.
- R. Farrell. PSAPD device characteristics. (private communication), 2009.
- R. Fontaine, M. A. Tetrault, F. Belanger, N. Viscogliosi, R. Himmich, J. B. Michaud, S. Robert, J. D. Leroux, H. Semmaoui, P. Berard, J. Cadorette, C. M. Pepin, and R. Lecomte. Real time digital signal processing implementation for an APD-based PET scanner with phoswich detectors. *IEEE Transactions on Nuclear Science*, 53; 53(3):784–788, 2006.
- R. Freifelder and J. S. Karp. Dedicated PET scanners for breast imaging. *Physics in Medicine and Biology*, 42(12):2463–2480, 1997.
- M. Furuta, K. Kitamura, J. Ohi, H. Tonami, Y. Yamada, T. Furumiya, M. Satoh, T. Tsuda, M. Nakazawa, N. Hashizume, Y. Yamakawa, A. Kawashima, and Y. Kumazawa. Basic evaluation of a c-shaped breast PET scanner. In *IEEE Nuclear Science Symposium and Medical Imaging Conference*, pages 2548–2552, 2009.

- M. S. Gossman, A. J. Pahikkala, M. B. Rising, and P. H. McGinley. Letter to the editor. *Journal of Applied Clinical Medical Physics*, 12(1), 2011.
- P. R. Gray, P. J. Hurst, S. H. Lewis, and R. G. Meyer. *Analysis and Design of Analog Integrated Circuits*. John Wiley & Sons, 2001.
- R. Grazioso, M. Aykac, M. E. Casey, G. Givens, and M. Schmand. APD performance in light sharing PET applications. *IEEE Transactions on Nuclear Science*, 52(5): 1413–1416, 2005.
- R. Grazioso, N. Zhang, J. Corbeil, M. Schmand, R. Ladebeck, M. Vester, G. Schnur, W. Renz, and H. Fischer. APD-based PET detector for simultaneous PET/MR imaging. *Nuclear Instruments and Methods in Physics Research Section A*, 569(2): 301–305, December 2006.
- Y. Gu and C. Levin. Studies of electrode design for a sub-mm resolution 3-d position sensitive CZT PET detector. In *IEEE Nuclear Science Symposium and Medical Imaging Conference*, pages 2303 –2305, 2011.
- Y. Gu, G. Pratz, F. W. Y. Lau, and C. S. Levin. Effects of multiple-interaction photon events in a high-resolution PET system that uses 3-d positioning detectors. *Medical Physics*, 37(10):5494, 2010.
- Y. Gu, J. L. Matteson, R. T. Skelton, A. C. Deal, E. A. Stephan, F. Duttweiler, T. M. Gasaway, and C. S. Levin. Study of a high-resolution, 3D positioning cadmium zinc telluride detector for PET. *Physics in Medicine and Biology*, 56(6):1563–1584, March 2011.
- P. Guerra, J. Ortuno, G. Kontaxakis, M. Ledesma-Carbayo, J. Vaquero, M. Desco, and A. Santos. Real-time digital timing in positron emission tomography. *IEEE Transactions on Nuclear Science*, 55(5):2531–2540, 2008.
- H. E. Johns and J. R. Cunningham. *The Physics of Radiology*. Charles C. Thomas, Springfield, Illinois, 3 edition, 1978.

- M. S. Judenhofer, C. Catana, B. K. Swann, S. B. Siegel, W.-I. Jung, R. E. Nutt, S. R. Cherry, C. D. Claussen, and B. J. Pichler. PET/MR images acquired with a compact MR-compatible PET detector in a 7-t magnet<sup>1</sup>. *Radiology*, 244(3):807–814, 2007.
- K. Kerlikowske, D. Grady, J. Barclay, E. A. Sickles, and V. Ernster. Effect of age, breast density, and family history on the sensitivity of first screening mammography. *JAMA*, 276(1):33–38, July 1996.
- T. Kimble, M. Chou, and B. Chai. Scintillation properties of LYSO crystals. In *IEEE Nuclear Science Symposium and Medical Imaging Conference*, volume 3, pages 1434 – 1437 vol.3, November 2002.
- G. F. Knoll. *Radiation Detection and Measurement*. Wiley, 3 edition, January 2000.
- D. B. Kopans. The positive predictive value of mammography. *American Journal of Roentgenology*, 158(3):521–526, March 1992.
- K. Kozmin, J. Johansson, and J. Delsing. Level-crossing ADC performance evaluation toward ultrasound application. *IEEE Transactions on Circuits and Systems I*, 56; 56(8):1708–1719, 2009.
- R. Kumar, A. Chauhan, H. Zhuang, P. Chandra, M. Schnall, and A. Alavi. Clinicopathologic factors associated with false negative FDG-PET in primary breast cancer. *Breast Cancer Research and Treatment*, Volume 98(3):267–274, 2006.
- H. Kume, S. Suzuki, J. Takeuchi, and K. Oba. Newly developed photomultiplier tubes with position sensitivity capability. *IEEE Transactions on Nuclear Science*, 32(1):448–452, February 1985.
- F. W. Y. Lau, C. Fang, P. D. Reynolds, P. D. Olcott, A. Vandenbroucke, V. C. Spanoudaki, F. Olutade, M. A. Horowitz, and C. S. Levin. 1mm<sup>3</sup> resolution breast-dedicated PET system. In *IEEE Nuclear Science Symposium and Medical Imaging Conference*, pages 5619–5622, 2008.

- F. W. Y. Lau, A. Vandenbroucke, P. D. Reynolds, P. D. Olcott, M. A. Horowitz, and C. S. Levin. Analog signal multiplexing for PSAPD-based PET detectors: simulation and experimental validation. *Physics in Medicine and Biology*, 55(23):7149–7174, 2010.
- F. W. Y. Lau, H. H. Choi, M. A. Horowitz, and C. S. Levin. A new IC with level-crossing ADC readout architecture for PET detector signals. In *IEEE Nuclear Science Symposium and Medical Imaging Conference*, pages 2486–2488, 2012a.
- F. W. Y. Lau, C. S. Levin, M. A. Horowitz, H. H. Choi, and J. Kim. Time-based digitizer for pet photodetector, 2012b. Patent Application PCT/US2012/067800, Publication Number WO2013085923 A1.
- F. W. Y. Lau, A. Vandenbroucke, P. D. Reynolds, H. Ho, D. Innes, and C. S. Levin. Signal conditioning technique for position sensitive photodetectors to manipulate pixelated crystal identification capabilities. *IEEE Transactions on Nuclear Science*, 59(5):1815–1822, 2012c.
- F. W. Y. Lau, J.-Y. Yeom, A. Vandenbroucke, P. D. Reynolds, D. Innes, and C. S. Levin. A cost-effective modular programmable HV distribution system for photodetectors. In *IEEE Nuclear Science Symposium and Medical Imaging Conference*, pages 3504–3506, 2012d.
- C. S. Levin. Design of a high-resolution and high-sensitivity scintillation crystal array for PET with nearly complete light collection. *IEEE Transactions on Nuclear Science*, 49(5):2236–2243, 2002.
- C. S. Levin. Primer on molecular imaging technology. *European Journal of Nuclear Medicine and Molecular Imaging*, 32 Suppl 2:S325–345, December 2005.
- C. S. Levin and E. J. Hoffman. Calculation of positron range and its effect on the fundamental limit of positron emission tomography system spatial resolution. *Physics in Medicine and Biology*, 44(3):781–799, March 1999.



- L. MacDonald, J. Edwards, T. Lewellen, D. Haseley, J. Rogers, and P. Kinahan. Clinical imaging characteristics of the positron emission mammography camera: PEM flex solo II. *Journal of Nuclear Medicine*, 50(10):1666–1675, October 2009.
- A. Mann, B. Grube, I. Konorov, S. Paul, L. Schmitt, D. P. McElroy, and S. I. Ziegler. A sampling ADC data acquisition system for positron emission tomography. *IEEE Transactions on Nuclear Science*, 53; 53(1):297–303, 2006.
- M. McClish, P. Dokhale, J. Christian, C. Stapels, E. Johnson, R. Robertson, and K. S. Shah. Performance measurements of CMOS position sensitive solid-state photomultipliers. *IEEE Transactions on Nuclear Science*, 57(4):2280–2286, August 2010.
- R. McIntyre. Multiplication noise in uniform avalanche diodes. *IEEE Transactions on Electron Devices*, 13(1):164 – 168, January 1966.
- C. L. Melcher. Scintillation crystals for PET. *Journal of Nuclear Medicine*, 41(6): 1051–1055, June 2000.
- M. Morh, J. Kliman, V. Matouek, M. Veselsk, and I. Turzo. Identification of peaks in multidimensional coincidence -ray spectra. *Nuclear Instruments Methods Physics Research A*, 443(1):108–125, March 2000.
- W. W. Moses, S. Payne, W.-S. Choong, G. Hull, and B. Reutter. Scintillator non-proportionality: Present understanding and future challenges. *IEEE Transactions on Nuclear Science*, 55(3):1049–1053, 2008.
- M. Moszynski, T. Ludziejewski, D. Wolski, W. Klamra, and V. V. Avdejchikov. Timing properties of GSO, LSO and other ce doped scintillators. *Nuclear Instruments and Methods in Physics Research Section A*, 372(1-2):51–58, March 1996.
- B. Murmann. ADC performance survey 1997-2012, 2012. URL <http://www.stanford.edu/~murmann/adcsurvey.html>. Web Page.
- J. Nissinen and J. Kostamovaara. Fully differential, regulated cascode amplifier. In *IEEE Mediterranean Electrotechnical Conference, MELECON*, pages 51–54, 2006.

- NOVA R&D. RENA-3 IC user specifications. Technical Report Rev 1.1b, Riverside, CA, June 2007.
- Y. Okada, T. Takahashi, G. Sato, S. Watanabe, K. Nakazawa, K. Mori, and K. Makishima. CdTe and CdZnTe detectors for timing measurements. *IEEE Transactions on Nuclear Science*, 49(4):1986 – 1992, August 2002.
- P. D. Olcott, F. Habte, J. Zhang, and C. S. Levin. Charge multiplexing readout for position sensitive avalanche photodiodes. In *IEEE Nuclear Science Symposium and Medical Imaging Conference*, volume 5, pages 2935–2937, 2005.
- P. D. Olcott, H. Peng, and C. S. Levin. Solid state photomultiplier (SSPM)-based PET detector with capacitively multiplexed readout and electro-optical coupling for PET/MR. *Society of Nuclear Medicine Annual Meeting Abstracts*, 50(2):354, May 2009.
- Ortec. Principles and applications of timing spectroscopy AN42, 2012. URL <http://www.ortec-online.com/download/Application-Note-AN42-Principles-Applications-Timing-Spectroscopy.pdf>.
- S. M. P. Park and H.-J. Yoo. 1.25-gb/s regulated cascode CMOS transimpedance amplifier for gigabit ethernet applications. *IEEE Journal of Solid-State Circuits*, 39(1):112–121, 2004.
- H. Peng and C. S. Levin. Recent developments in PET instrumentation. *Current Pharmaceutical Biotechnology*, 11(6):555–571, September 2010.
- H. Peng, P. Olcott, A. Foudray, and C. Levin. Evaluation of free-running ADCs for high resolution PET data acquisition. In *IEEE Nuclear Science Symposium and Medical Imaging Conference*, volume 5, pages 3328 –3331, 2007.
- C. Pepin, P. Berard, A.-L. Perrot, C. Pepin, D. Houde, R. Lecomte, C. Melcher, and H. Dautet. Properties of LYSO and recent LSO scintillators for phoswich PET detectors. *IEEE Transactions on Nuclear Science*, 51(3):789 – 795, June 2004.

- B. J. Pichler, B. K. Swann, J. Rochelle, R. E. Nutt, S. R. Cherry, and S. B. Siegel. Lutetium oxyorthosilicate block detector readout by avalanche photodiode arrays for high resolution animal PET. *Physics in Medicine and Biology*, 49(18):4305–4319, September 2004.
- V. Popov, S. Majewski, A. G. Weisenberger, and R. Wojcik. Analog readout system with charge division type output. In *IEEE Nuclear Science Symposium and Medical Imaging Conference*, volume 4, pages 1937–1940, 2001.
- V. Popov, S. Majewski, and B. L. Welch. A novel readout concept for multianode photomultiplier tubes with pad matrix anode layout. *Nuclear Instruments and Methods in Physics Research Section A*, 567(1):319–322, November 2006.
- G. Pratz and C. S. Levin. Bayesian reconstruction of photon interaction sequences for high-resolution PET detectors. *Physics in Medicine and Biology*, 54(17):5073–5094, September 2009.
- C. D. Rajadhyaksha, J. A. Parker, L. Barbaras, and V. H. Gerbaudo. Normal and benign pathologic findings in <sup>18</sup>F-FDG-PET and PET/CT, 2012.
- R. R. Raylman, S. Majewski, M. F. Smith, J. Proffitt, W. Hammond, A. Srinivasan, J. McKisson, V. Popov, A. Weisenberger, C. O. Judy, B. Kross, S. Ramasubramanian, L. E. Banta, P. E. Kinahan, and K. Champley. The positron emission mammography/tomography breast imaging and biopsy system (PEM/PET): design, construction and phantom-based measurements. *Physics in Medicine and Biology*, 53(3):637–653, February 2008.
- B. Razavi. *Design of integrated circuits for optical communications*. McGraw-Hill, New York, 2003.
- P. D. Reynolds, F. W. Y. Lau, A. Vandenbroucke, and C. S. Levin. Readout design and validation for a 1 mm<sup>3</sup> resolution clinical PET system. In *IEEE Nuclear Science Symposium and Medical Imaging Conference*, pages 3097–3099, 2010a.

- P. D. Reynolds, P. D. Olcott, G. Pratz, F. W. Y. Lau, and C. S. Levin. Convex optimization of coincidence time resolution for a high resolution PET system. *IEEE Transactions on Medical Imaging*, PP(99):1, 2010b.
- P. D. Reynolds, F. W. Y. Lau, A. Vandenbroucke, D. Innes, U. Yoruk, and C. S. Levin. Characterization of detector layers from a 1 mm<sup>3</sup> resolution clinical PET system. In *IEEE Nuclear Science Symposium and Medical Imaging Conference*, pages 3804–3807, 2012.
- E. L. Rosen, W. B. Eubank, and D. A. Mankoff. FDG PET, PET/CT, and breast cancer imaging. *Radiographics*, 27(suppl 1):S215–S229, October 2007.
- R. D. Rosenberg, W. C. Hunt, M. R. Williamson, F. D. Gilliland, P. W. Wiest, C. A. Kelsey, C. R. Key, and M. N. Linver. Effects of age, breast density, ethnicity, and estrogen replacement therapy on screening mammographic sensitivity and cancer stage at diagnosis: review of 183,134 screening mammograms in albuquerque, new mexico. *Radiology*, 209(2):511–518, November 1998.
- E. Sackinger. The transimpedance limit. *IEEE Transactions on Circuits and Systems I*, 57(8):1848–1856, August 2010.
- R. Sarpeshkar, T. Delbruck, and C. Mead. White noise in MOS transistors and resistors. *IEEE Circuits and Devices Magazine*, 9(6):23–29, 1993.
- N. Sayiner, H. Sorensen, and T. Viswanathan. A level-crossing sampling scheme for A/D conversion. *IEEE Transactions on Circuits and Systems II*, 43(4):335–339, 1996.
- K. S. Shah. A novel position sensitive detector for nuclear radiation. Report submitted to the department of energy, RMD Inc., Watertown, MA, 2005.
- K. S. Shah, R. Farrell, R. Grazioso, E. Harmon, and E. Karplus. Position-sensitive avalanche photodiodes for gamma-ray imaging. *IEEE Transactions on Nuclear Science*, 49(4):1687–1692, 2002.

- K. S. Shah, R. Grazioso, R. Farrell, J. Glodo, M. McClish, G. Entine, P. Dokhale, and S. R. Cherry. Position sensitive APDs for small animal PET imaging. *IEEE Transactions on Nuclear Science*, 51(1):91–95, 2004.
- Y. Shao. A new timing model for calculating the intrinsic timing resolution of a scintillator detector. *Physics in Medicine and Biology*, 52(4):1103–1117, February 2007.
- Y. Shao, H. B. Barber, S. J. Balzer, and S. R. Cherry. Measurement of coincidence timing resolution with CdTe detectors. *Proceedings of SPIE*, pages 254–264, December 2000.
- K. Shimazoe, J. Yeom, H. Takahashi, T. Kojo, Y. Minamikawa, K. Fujita, and H. Murayama. Multi-channel waveform sampling ASIC for animal PET system. In *IEEE Nuclear Science Symposium and Medical Imaging Conference*, volume 4, pages 2473–2475, 2006.
- S. Siegel, R. W. Silverman, Y. Shao, and S. R. Cherry. Simple charge division readouts for imaging scintillator arrays using a multi-channel PMT. *IEEE Transactions on Nuclear Science*, 43(3):1634–1641, 1996.
- V. C. Spanoudaki and C. S. Levin. Photo-detectors for time of flight positron emission tomography (ToF-PET). *Sensors*, 10(11):10484–10505, November 2010.
- V. C. Spanoudaki, A. Vandenbroucke, F. W. Y. Lau, C. Fang, and C. S. Levin. Effects of thermal regulation structures on the photon sensitivity and spatial resolution of a 1 mm<sup>3</sup> resolution breast-dedicated PET system. In *IEEE Nuclear Science Symposium and Medical Imaging Conference*, pages 5657–5661, 2008.
- H. Spieler. *Semiconductor Detector Systems*. Oxford University Press, October 2005.
- T. Tumer, V. Cajipe, M. Clajus, S. Hayakawa, and A. Volkovskii. Multi-channel front-end readout IC for position sensitive solid-state detectors. In *IEEE Nuclear Science Symposium and Medical Imaging Conference*, volume 1, pages 384–388, 2006.

- T. O. Tumer, V. B. Cajipe, M. Clajus, S. Hayakawa, and A. Volkovskii. Performance of RENA-3 IC with position-sensitive solid-state detectors. In *Proceedings of SPIE*, volume 7079, page 70791, 2008.
- A. van Oosterom and J. Strackee. The solid angle of a plane triangle. *IEEE Transactions on Biomedical Engineering*, BME-30(2):125–126, February 1983.
- A. Vandenbroucke, A. M. K. Foudray, P. Olcott, and C. S. Levin. Performance characterization of a new high resolution PET scintillation detector. *Physics in Medicine and Biology*, 55(19):5895–5911, October 2010.
- A. Vandenbroucke, T. J. McLaughlin, and C. S. Levin. Influence of temperature and bias voltage on the performance of a high resolution PET detector built with position sensitive avalanche photodiodes. *Journal of Instrumentation*, 7(08):P08001–P08001, August 2012.
- G. C. Wang, J. S. Huber, W. W. Moses, J. Qi, and W. S. Choong. Characterization of the LBNL PEM camera. *IEEE Transactions on Nuclear Science*, 53(3):1129–1135, 2006.
- X. Wang, Q. Xie, Y. Chen, M. Niu, and P. Xiao. Advantages of digitally sampling scintillation pulses in pileup processing in PET. *IEEE Transactions on Nuclear Science*, 59(3):498–506, June 2012.
- I. N. Weinberg, D. Beylin, V. Zavarzin, S. Yarnall, P. Y. Stepanov, E. Anashkin, D. Narayanan, S. Dolinsky, K. Lauckner, and L. P. Adler. Positron emission mammography: high-resolution biochemical breast imaging. *Technology in Cancer Research & Treatment*, 4(1):55–60, February 2005.
- M. N. Wernick and J. N. Aarsvold. *Emission tomography: the fundamentals of PET and SPECT*. Academic Press, 2004.
- Y. Wu, S. L. Bowen, K. Yang, N. Packard, L. Fu, G. Burkett, J. Qi, J. M. Boone, S. R. Cherry, and R. D. Badawi. PET characteristics of a dedicated breast PET/CT scanner prototype. *Physics in Medicine and Biology*, 54(13):4273–4287, July 2009.

- T. Yamashita. *Development of New Position-Sensitive Detectors for Positron Emission Tomography*. PhD thesis, Central Research Laboratory, Hamamatsu Photonics K.K., 1992.
- J. Zhang, A. M. K. Foudray, P. D. Olcott, R. Farrell, K. S. Shah, and C. S. Levin. Performance characterization of a novel thin position-sensitive avalanche photodiode for 1mm resolution positron emission tomography. *IEEE Transactions on Nuclear Science*, 54(3):415–421, 2007a.
- J. Zhang, P. D. Olcott, G. Chinn, A. M. K. Foudray, and C. S. Levin. Study of the performance of a novel 1 mm resolution dual-panel PET camera design dedicated to breast cancer imaging using monte carlo simulation. *Medical Physics*, 34(2):689–702, 2007b.
- N. Zhang, R. Grazioso, N. K. Doshi, and M. Schmand. RF transformer coupled multiplexing circuits for APD PET detectors. *IEEE Transactions on Nuclear Science*, 53(5):2570–2577, 2006.